ABSTRACT

INFLUENCE OF BEACH HYDRODYNAMICS ON SALTWATER TRANSPORT AND OIL PERSISTENCE IN BEACHES

by
Ali Abdollahi-Nasab

The exchange of water and solutes across the aquifer-ocean interface plays an important ecological role in both aquifer and the open water. Saltwater intrusion could prevent utilization of groundwater for either drinking water or irrigation. In addition, the flux of solutes, such as nutrients, from inland groundwater sources plays an important role in shoreline ecology, especially in embayments. This research relies on a three-pronged approach, involving a laboratory beach experiment, field scale experiments and numerical analyses. The laboratory beach experiment is designed to investigate the fundamental processes occurring in beach aquifers. It explores the effects of buoyancy (or lack thereof) on the flushing of freshwater to sea. The results indicate that the increase in water pressure when freshwater inundates saltwater systems exceeds the pressure obtained assuming the system is filled with freshwater. This has implications for the evaluation of stress on aquifers and the management of coastal aquifers.

The field study is conducted along two transects of a tidally influenced gravel beach in Prince William Sound (PWS), Alaska, which was heavily polluted by the Exxon Valdez oil. The observed data of water table, pore water salinity and tracer (lithium) concentration indicates high freshwater recharge to the clean transect and low freshwater recharge to the oiled transect. The numerical model MARUN is used to reproduce the observations of water pressure and pore water salinity at both transects. Based on the field experiments and numerical simulations, the beach can be viewed as a two-layer

system from a hydraulic point of view with a high permeable upper layer underlain by a layer with low permeability.

Five hypotheses are designed and tested to explore factors affecting the beach hydrodynamics. One of the hypotheses establishes that the density gradient between saltwater and freshwater does not play a role in the intertidal zone of beaches. This hypothesis is tested through numerical modeling and laboratory experiments and is rejected. The results show that the density gradient has significant effect on solute transport in the intertidal zone. Another hypothesis states that depth (and slope) of bedrock greatly affects solute transport in beaches. Numerical investigations indicate that the depth of bedrock greatly affects solute transport in homogenous beaches while it has minor impact on that in the upper layer of two-layer beaches. A third hypothesis states that in locations of a large freshwater recharge, it is less likely to find oil. Numerical simulations reveal that freshwater recharge promotes the removal of oil in two-layer beaches by maintaining the water table at or above the interface of the two layers.

Findings from this work in relation to oiled beaches include: 1) oil tends to persist at locations of small freshwater recharge, 2) Prior to oil arriving to the shoreline, one could minimize oil penetration into the beach by releasing water onto the beach at the high tide line during low tides, and 3) bioremediation of oil polluted beaches should be conducted using deep injection as amendments applied on the beach surface would washout rapidly to sea.

INFLUENCE OF BEACH HYDRODYNAMICS ON SALTWATER TRANSPORT AND OIL PERSISTENCE IN BEACHES

by
Ali Abdollahi-Nasab

A Dissertation
Submitted to the Faculty of
New Jersey Institute of Technology
in Partial Fulfillment of the Requirements for the Degree of
Doctor of Philosophy in Environmental Engineering

Department of Civil and Environmental Engineering

January 2014

APPROVAL PAGE

INFLUENCE OF BEACH HYDRODYNAMICS ON SALTWATER TRANSPORT AND OIL PERSISTENCE IN BEACHES

Ali Abdollahi-Nasab

Dr. Michel C. Boufadel, Dissertation Advisor	Date
Professor of Civil and Environmental Engineering, NJIT	

Dr. Lisa B. Axe, Committee Member	Date
Professor of Civil and Environmental Engineering, NJIT	

Dr. Robert Dresnack, Committee Member	Date
Professor of Civil and Environmental Engineering, NJIT	

Dr. Taha F. Marhaba, Committee Member	Date
Professor of Civil and Environmental Engineering, NJIT	

Dr. Priscilla Nelson, Committee Member	Date
Professor of Civil and Environmental Engineering, NJIT	

Dr. Nancy L. Jackson, Committee Member	Date
Professor of Chemistry and Environmental Science, NJIT	

BIOGRAPHICAL SKETCH

Author: Ali Abdollahi-Nasab

Degree: Doctor of Philosophy

Date: January 2014

Undergraduate and Graduate Education:

- Doctor of Philosophy in Environmental Engineering,
  New Jersey Institute of Technology, Newark, NJ, 2014

- Master of Science in Environmental Engineering,
  Sharif University of Technology, Tehran, Iran, 2007

- Bachelor of Science in Civil Engineering,
  Amirkabir University of Technology, Tehran, Iran, 2003

Major: Environmental Engineering

Presentations and Publications:

Abdollahi-Nasab, A., Boufadel, M. C., Saleh, F. (2014). "Effects of beach hydrodynamics on the long-term persistence of the Exxon Valdez oil in a wave-exposed gravel beach." (In Preparation to submit to Water Resour. Res.)

Abdollahi-Nasab, A., Boufadel, M. C., Saleh, F., Geng, X. (2014). "A Tracer study in a gravel beach polluted by the Exxon Valdez oil." (In Preparation to submit to Groundwater)

Abdollahi-Nasab, A., Boufadel, M. C., Geng, X. (2013). "Role of freshwater in the persistence of the Exxon Valdez oil spill in a wave-exposed beach." Environmental and Water Resources Institute Congress, Cincinnati, OH.

Abdollahi-Nasab, A., M. C. Boufadel, Li, H., Weaver, J. W. (2010). "Saltwater flushing by freshwater in a laboratory beach." J. Hydrol., 386, 1-12.

Abdollahi-Nasab, A., Li, H., Boufadel, M. C. (2009). "Temporal evolution of the freshwater-saltwater interface." American Geophysical Union Fall Meeting, San Francisco, CA.

To: Baba and Maman
and
Hoda

To the Promised One, to the Savior

ACKNOWLEDGEMENT

TABLE OF CONTENTS

TABLE OF CONTENTS
(Continued)

LIST OF TABLES

LIST OF FIGURES

CHAPTER 1

INTRODUCTION

1.1   Exxon Valdez Oil Spill

On March 24, 1989, the 987-foot tank vessel Exxon Valdez struck Bligh Reef in Prince William Sound (PWS), Alaska. As the result of the Exxon Valdez oil spill, 783 km of the Prince William Sound shorelines (approximately 5000 km) were polluted (Neff et al., 1995). The area affected by the Exxon Valdez oil spill is shown in Figure 1.1. After the oil spill, one of the largest containment and cleanup operations was started. Shoreline cleanup began in April of 1989 and continued until September of 1989 constituting the first year of the response. The response effort continued in 1990 and 1991 with cleanup in the summer months, and limited shoreline monitoring in the winter months. Most cleanup efforts focused on the more heavily oiled upper and middle intertidal zones (Neff et al., 1995). During June 1992, both the federal and state governments declared that no additional cleanup of shoreline was needed, because further cleanup activities would provide no net environmental benefit.

However, scientists from the National Oceanic and Atmospheric Administration (NOAA) conducted an extensive study in PWS and estimated that between 60 to 100 tons of oil still remains in the subsurface of beaches in PWS (Short et al., 2004; Short et al., 2006). The oil persistence was noted by other studies (Li and Boufadel, 2010; Michel and Hayes, 1999; Taylor and Reimer, 2008). Based on the research by Short et al. (2004), the oil contains a relatively high percentage of Polycyclic Aromatic Hydrocarbons (PAH) known to be highly toxic to wildlife (Carls et al., 2003). To restore

oiled beaches, a thorough understanding of the beach hydrogeological characteristics and groundwater dynamics should be obtained (Li and Boufadel, 2010; Owens et al., 2008).
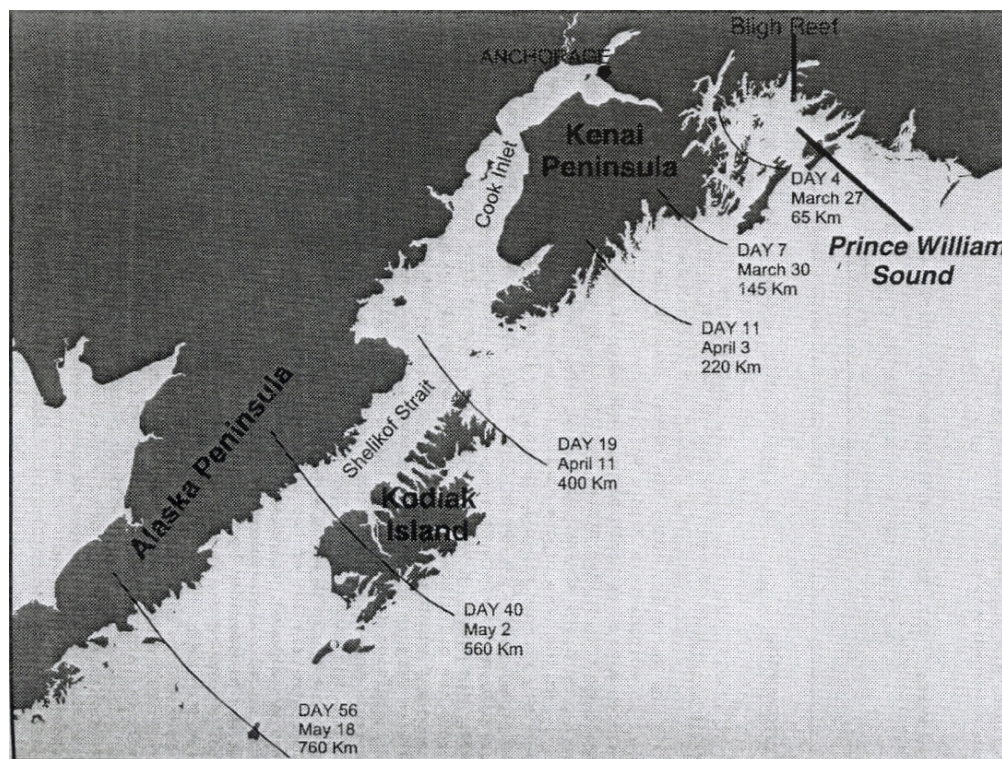
Figure 1.1   The trajectory of spilled oil throughout Prince William Sound and the western Gulf of Alaska
Source: Neff et al. (1995).

1.2   Modeling Water Flow and Solute Transport in Beach Environment

Understanding groundwater flow and solute transport in coastal aquifers plays an important role in quantifying saltwater intrusion (Ataie-Ashtiani et al., 1999; Cobaner et al., 2012; Goswami and Clement, 2007; Huyakorn et al., 1987) in determining nutrients and contaminants transport from aquifers to coastal waters (Burnett et al., 2003; Li et al. 1999; Moore, 1999; Slomp and van Cappellen, 2004; Uchiyama et al., 2000) and in performing bioremediation in polluted beaches (Boufadel, 2000; Boufadel et al., 2006;

Brovelli et al. 2007; Eljamal et al., 2008; Li et al., 2007; Venosa et al., 1996; Wrenn et al., 1997). Groundwater flow dynamics and solute transport in beach aquifers has been intensively addressed in the literature by implementing analytical solutions, numerical simulations and laboratory or field experiments. Here only some of these studies are listed.

Phillip (1973) used an analytical solution to study a vertical face beach and found that the average water table in the beach was higher than the average seawater level. Nielsen (1990) investigated the tidal dynamics in a sloping beach via field measurements and confirmed the findings of Phillip (1973). Turner et al. (1997) conducted a field study to distinguish between the role of tides and that of waves in raising the water table above the elevation of mean sea level. Wrenn et al. (1997) evaluated the nutrient transport in a sandy beach in Delaware Bay using a conservative tracer. They concluded that the nutrient transport was driven by tidal fluctuation and wave action. Based on their discussion, the horizontal movement of the plume could be due to the hydraulic gradient between the average water table in the beach and the mean sea level. Also, the downward transport of the plume could be driven by waves. Boufadel (2000) conducted two laboratory experiments to investigate the effects of tides and buoyancy on beach hydraulics. The MARUN model (Boufadel et al., 1999a) was used to simulate the observations. He found that the seawater penetrated deeper in the midsection of the intertidal zone. Based on his work, groundwater in the aquifer moved seaward beneath the upper saline plume and exited the domain near the low tide mark (the "freshwater tube"). He suggested an application of dissolved nutrients at low tides for the oil bioremediation similar to the application strategy used by Venosa et al. (1996).

Ataie-Ashtiani et al. (2001) used a 2D model to investigate the influence of tidal fluctuation on contaminants carried by saline groundwater to the sea. They concluded that tides affected the shape of the contaminant plume. Li et al. (2004) reported that the salinity distribution in the aquifer is more complex due to the tide's effect. They also observed the "freshwater tube" in their study noted by Boufadel (2000).

Another study was conducted by Mao et al. (2006) to investigate the effect of tide on contaminant transport in a mildly sloping beach. They reported complex flow patterns produced by tide. Boufadel et al. (2006) conducted a tracer study in a laboratory beach and investigated the effect of tide on water flow and solute transport. They indicated that for bioremediation of the polluted beaches, the nutrient should be applied near the high-tide line during low tides. Brovelli et al. (2007) numerically modeled the transport of a dense contaminant plume in a tidal aquifer. Based on their simulations, the contaminant was mainly discharged from the beach surface. Also, they recommended that both tide and density effects should be accounted for in the study of contaminant transport in tidal aquifers. Li et al. (2008) investigated seawater-groundwater circulation in a tidal shallow aquifer using a dimensionless formulation. They related the size of the saltwater plume in the intertidal zone to inland freshwater recharge and beach permeability. Abdollahi-Nasab et al. (2010) used MARUN model to simulate the process of the saltwater flushing by freshwater in a laboratory beach under the steady state condition. They found the buoyancy plays an important role when the seawater salinity is high (e.g., 34 g/L, around the value for the salinity of coastal waters). Boufadel et al. (2011) modeled the solute transport and transient seepage in a laboratory beach. They concluded that it is important to use variably-saturated models to simulate the tidally influenced beaches.

Most of the studies on beach hydrodynamics focus on the littoral environments composed of finer sediments (e.g., sandy beaches), and less attention has been paid to the study of gravel beaches. This could be due to the logistical problems associated with studying gravel beaches (Buscombe and Masselink, 2006) or more usage of sandy beaches for recreational purposes (Hayes et al., 2009). However, understanding the dynamics of gravel beaches is important (Buscombe and Masselink, 2006) especially if the goal is to responds to oil spills or to remediate the polluted beaches (Hayes et al., 2009; Michel and Hayes, 1999).

Li and Boufadel (2010) more recently conducted a field study to identify the hydrogeological factors that determined the persistence of oil in a gravel beach in Eleanor Island, PWS. Their results indicated that the beach (or similar gravel beaches) could be viewed as a two-layer system from a hydraulic point of view with a higher permeable layer on top of a very low permeable layer. This two-layer system was confirmed by other studies conducted later in different beaches of PWS (Xia et al., 2010; Guo et al., 2010; Bobo et al., 2012). Xia et al. (2010) studied an oiled transect of a gravel beach in Knight Island, PWS and concluded that the small flow entering the beach from the land could be the reason for the oil persistence in the beach. They also conducted a numerical simulation of nutrient application on the beach surface and concluded that if the nutrient was the limiting factor, this method of nutrient application could provide enough nutrients for an extended period of time such that the biodegradation could happen. Guo et al. (2010) investigated the beach hydrodynamics in a clean transect of the same gravel beach studied by Xia et al. (2010). They conducted field measurements and numerical simulations and also performed a sensitivity analysis to explore the effect of hydraulic

conductivity and dispersivities on the simulation results. Bobo et al. (2012) studied the groundwater flow in another tidally influenced gravel beach in PWS. They concluded that the change in the beach slope affected the water flow in the gravel beach they studied. These beaches and also the beach studied in this dissertation are labeled as gravel beaches because of the visual appearance of the surface layer, but some researchers label them as mixed beaches (Mason and Coates, 2001). For this dissertation, we will continue to label them as gravel beaches for simplicity.

1.3   Objectives

This work focuses on hydrodynamics factors affecting the water and solute transport in beaches and evaluates their potential impact on coastal areas that are subjected to multiple stressors such as saltwater intrusion, sea level rise and oil spills pollution. The investigation was carried out through two case studies. The first one (the tank study) implemented experimental and numerical techniques to quantify the flushing of saltwater in a laboratory beach subjected to steady state condition (Abdollahi-Nasab et al., 2010). The second case study (beach study) consisted of simulating the observation results of water table and pore water salinity obtained from a field study in a tidal gravel beach located in PWS, Alaska. This beach was heavily polluted by the Exxon Valdez oil spill in 1989 and was subjected to extensive treatment (Page et al., 2008; Taylor and Reimer, 2008). Oil persisted on the left side of the beach (when looking landward from sea) but no oil residues were found in the right side at the time of field study. So, the goal is to provide explanations on possible reasons for the disappearance of oil from right side of the beach and its persistence from the left side (of this beach or other beaches in PWS) from the viewpoint of beach hydraulics.

The lab study was more fundamental elucidating the role of density and freshwater on the pressure and water level in beach environments. The tidal action was ignored as the goal was to explore the buoyancy effect (as one of the hydrodynamic factors affecting solute transport in beaches) in a system with large time scale (time scale of months when considering seasonal exchange or days when considering the storm water entering the beaches). The field study was aimed at understanding the movement of water and solute in a two-layer beach, and its impact on oil spills.

In this investigation, questions including but not limited to the following are addressed:

1. Where is the location for maximum seawater-groundwater exchange in the beaches?

2. What is the impact of high salinity wedge on the seaward flow in the subtidal zone (zone seaward of the low tide line)?

3. What is the role of density gradient between saltwater and freshwater in the intertidal zone?

4. What is the impact of bedrock depth on solute transport in beaches?

5. What is the role of freshwater source in the oil persistence in polluted beaches?

These questions are addressed through numerical modeling and experiments conducted in both laboratory and natural beaches. Some of the differences between water flow and solute transport in sandy beaches and gravel beaches are also discussed.

CHAPTER 2

SALTWATER FLUSHING BY FRESHWATER IN A LABORATORY BEACH[1]

2.1   Abstract

Experiments were conducted to investigate the flushing of saltwater out of a laboratory coastal aquifer by freshwater propagating seaward. After a steady state distribution was achieved with a seaward hydraulic gradient, freshwater was introduced while keeping the total head constant at each boundary. This caused the propagation of freshwater seaward. Two initial uniform concentrations were used: Case 1: 2.0 g/L (low salinity case), and Case 2: 34.0 g/L (high salinity case). The observed salinity and pressure data were closely reproduced using the MARUN (Boufadel et al., 1999a) numerical code.

   The results indicated that buoyancy plays an important role for Case 2 but is negligible for Case 1. The results also indicated that the flow in the offshore beach aquifer (submerged portion of beach) was negligible especially for Case 2. For this case, the pressure increased with time until reaching a peak and then decreased (i.e., humps were formed). This was not observed in the low salinity case. Investigations revealed that the increase in pressure is due to a combination of remnant high salinity and a rise in the water table at that location. Numerical investigations revealed that for the same difference in total head, the seaward flow of freshwater increases with a decrease in the seawater salinity. The increase, however, was nonlinear as a function of seawater density. For example, the discharge in the high salinity case was 20 percent lower than that in the low salinity case.

1: The material of this chapter has been published in the Journal of Hydrology, 2010.

2.2   Introduction

Seawater intrusion is a major concern for various coastal communities (Barlow and Reichard, 2010; Bear et al., 1999). The steady state interface of freshwater/seawater has been studied by many researchers in the context of saltwater intrusion in aquifers. W. Ghyben and A. Herzberg (Freeze and Cherry, 1979 p 376) assumed static equilibrium and a hydrostatic pressure distribution in the freshwater region with stationary sea water. Glover (1959) assumed that freshwater and saltwater are at the dynamic equilibrium which is more physical.   Henry (1964) developed the first analytical solution for predicting the steady state salt distribution in a confined coastal aquifer while accounting for mechanical dispersion, which results in a gradual change of the salinity between the seawater and the freshwater, a more realistic situation. However, he used a constant dispersion coefficient in his study. Frind (1982) in his finite element model considered a velocity-dependent dispersion coefficient and discussed the errors caused by use of a constant dispersion coefficient. Huyakorn (1987) presented an improved finite element model capable of simulating multiple aquifer systems, the top aquifer being confined or phreatic.   Galeati et al. (1992) used an implicit Eulerian-Lagrangian finite element formulation to study the effect of dewatering on seawater intrusion through an unconfined coastal aquifer. They also discussed the effect of aquifer heterogeneity and the construction of a cutoff well on seawater intrusion. Croucher and O'Sullivan (1995) discussed the previous solutions of the Henry problem and gave possible reasons for the observed disagreements between them. They suggested that the usage of relatively few grid points could have resulted in excessive numerical dispersion that affected the numerical results. More recently, Simpson and Clement (2003) assessed the worthiness

of the Henry's problem using a coupled versus uncoupled strategy. They concluded that the distribution of the saline water in Henry's problem is dictated by the boundary forcing. Consequently, Simpson and Clement (2004) presented an improved version of Henry's problem by decreasing the freshwater recharge. Abarca et al. (2007) proposed anisotropic dispersive Henry problem to consider sensitivity to density variations and vertical salinity profiles observed in real cases. The solution of their problem was closer to reality.

All these studies addressed the steady state distribution of the saltwater in a beach aquifer. However, there are situations where knowledge of salinity evolution with time within an aquifer is essential. Examples include freshwater entering a coastal aquifer following a storm or due to seasonal variation of freshwater recharge. The evolution of salinity with time has important implications on biochemical reactions in coastal aquifers due to ion exchange, whereby the ions Na^+ and Mg^{2+} get replaced by Ca^{2+} when freshwater displaces saltwater in a coastal aquifer (Slomp and Van Capellen, 2004). An important application of geochemical reactions was noted by Michael et al. (2005) who provided an explanation for the high concentrations of ^{226}Ra in the southeastern US coast reported by Moore (1996).

This chapter investigates the fundamental processes of saltwater flushing by freshwater in a laboratory setup. The layout of this chapter is as follows: The experimental setup is presented followed by a description of the governing equations. The experimental results are then reported followed by calibration of the numerical model MARUN (Boufadel et al., 1999a). The major factors affecting the mechanisms of transport are then investigated numerically.

2.3   Materials and Methods

2.3.1 Facility and Devices

Tank and experiment design

The laboratory tank consisted of an 8 m long, 2 m high, and 0.6 m wide carbon steel tank as shown in Figure 2.1. The sand in the tank was graded at a slope of 10% from a height of 1.15 m down to 0.65 m and then let to rest at its natural slope from 0.65 m to zero (the tank bottom). This resulted in a horizontal length of the beach of 6.3 m at the bottom (Figure 2.1). The sand was separated from the left tank by a screen made of fine mesh. The pores of the screen were large enough (0.1 mm) to allow unhindered passage of water through them. To simulate inland freshwater recharge and concentration landward of the beach, water was pumped into the tank through a 30 cm-long manifold placed across the bottom of the left tank. A mixer was placed in the open water at the right-hand side to guarantee a uniform salt concentration in the sea.   The sand used in the experiments was artificial sand composed mostly of silica (SiO_2) from Sidley, Inc., Cleveland, Ohio. It had a median size of 1.0 mm and a very narrow particle size distribution, varying between 0.8 and 1.2 mm. The particle shape was classified as "round to semiangular." The sand porosity was determined to be 0.38, by filling a 4 L beaker with well-drained sand and adding a sufficient amount of water to produce ponding conditions at the sand surface. The ratio of the volume of the added water to the apparent volume of the sand is, by definition, the porosity of the medium. The porosity of sand in the tank was measured in situ by observing the settlement of the beach sand profile that occurred a few days after the sand was placed in the tank and covered with water. The reduction in sand height in the beach was about 4%, resulting in a porosity of

(1– 0.04) (0.38) = 0.365. A value of 0.36 was adopted to be used in the model. The values for unsaturated flow parameters and the saturated hydraulic conductivity used by Boufadel (2000) were used as initial estimates and new values were obtained upon calibration of the model to data.
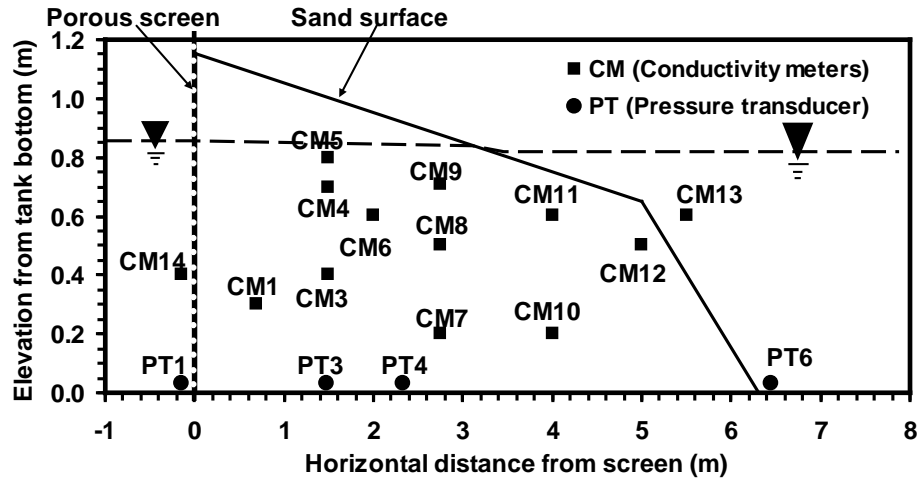
Figure 2.1 Schematic of the laboratory beach and location of sensors (Conductivity Meters and Pressure Transducers). The sensor locations are given in Table 2.1.

Measuring devices

The water pressure at the tank bottom was measured using Pressure Transducers (PT, model 1151AP, Fisher Scientific, Hampton, New Hampshire) that have a reading accuracy of ~2.0 mm of freshwater. Although the PTs were placed 3.0 cm above the bottom of the tank (Table 2.1 and Figure 2.1), the readings were calibrated by taking the tank bottom as the datum. The Strawberry Tree data software (Strawberry Software Inc., Sunnyvale, California) was used to log and control the inflow and outflow pumps, which regulated the water flows and levels in the left and right tanks. The salt concentration was obtained through Conductivity Meters (CM) that measure the electrical conductivity of the water solution, which were calibrated to the salt concentration. The CMs were in

the shape of a hollow disk (doughnut) which had the dimensions 10 cm (external

diameter), 2.5 cm (internal diameter), and 3 cm (thickness). Early experimentation

revealed that the Conductivity Meters were accurate within 1%. However, they were

logged to a CR10 data logging software (Rocktest Inc., Plattsburg, NY) that was sensitive

to power fluctuations causing a degeneration of the accuracy to about 5%. The locations

of the Conductivity Meter centers are given in Table 2.1 and also plotted in Figure 2.1.

The data from all sensors were logged at an interval of 30 s. The data were collected for

16 hours for the low salinity case (Case 1) and 24 hours for the high salinity case (Case

2).

Table 2.1 Locations of Pressure and Concentration Sensors[a]

Sensor	x (cm)	z (cm)	y (cm)
PT1	-15	3	60
PT3	147	3	60
PT4	232.5	3	60
PT6	645	3	60
CM1	70	30	20
CM3	150	40	20
CM4	150	70	40
CM5	150	80	25
CM6	200	60	30
CM7	275	20	40
CM8	275	50	20
CM9	275	71	25
CM10	400	20	20
CM11	400	60	40
CM12	500	50	30
CM13[b]	550	60	30
CM14[b]	-15	40	30

[a] Here, x is the horizontal distance from the screen (positive seaward), z is the elevation
from the tank bottom, and y is the horizontal distance from the plexiglass wall (positive
inward perpendicular to the plane of Figure 2.1).
[b] The sensor is in open water (see Figure 2.1).

2.3.2 MARUN Model

The marine unsaturated (MARUN) is a finite element model that can simulate water flows in the saturated and the unsaturated zones of two dimensional porous media taking into account the effects of salt concentration on water density and water viscosity. Neglecting the elastic storage of the matrix, the water flow equation for homogeneous, isotropic two-dimensional domains can be written as (Boufadel et al., 1999a; Boufadel, 2000):

$$
\begin{aligned}
\beta\phi\frac{\partial S}{\partial t} + \beta\,S_0 S\frac{\partial\psi}{\partial t} + \phi\,S\frac{\partial\beta}{\partial t} &= \frac{\partial}{\partial x}(\beta\delta k_r K_0\frac{\partial\psi}{\partial x}) \\
&+ \frac{\partial}{\partial z}\left[\beta\delta k_r K_0\left(\frac{\partial\psi}{\partial z} + \beta\right)\right]
\end{aligned}
\tag{2.1}
$$

where ψ [L] is the pressure head, ϕ is the porosity, S_0 [L^{-1}] is the specific storage per unit fluid weight, S is the degree of water saturation (fraction of pore volume occupied by water), K_0 [LT^{-1}] is the saturated hydraulic conductivity for freshwater (constant), k_r is the relative permeability, β is the density ratio defined as:

$$
\beta = \frac{\rho}{\rho_0} = 1 + \varepsilon c \geq 1
\tag{2.2}
$$

where ρ [ML^{-3}] is the density of the beach pore water, $\rho_0 = 998.2$ kg/m^3 is the fresh water density at 20°C, ε is the coefficient of expansivity resulting from the change of the mass concentration of the solute at constant hydraulic head [L^{3}M^{-1}] and is given in Table

2.2, c is the salt concentration [ML^3] of the beach pore water, and δ is the dynamic viscosity ratio defined by Boufadel et al. (1999a) as:

$$\delta = \frac{\mu_0}{\mu} = 1 - \xi c \leq 1 \tag{2.3}$$

where μ [$ML^{-1}T^{-1}$] is the dynamic viscosity of the beach pore water, $\mu_0 = 0.001$ kg/(m.s) is the dynamic viscosity of the fresh water at 20^oC, and ξ is a constant equal to 1.566×10^{-3} m^3/kg.

The soil moisture ratio and the relative permeability are correlated by the van Genuchten (1980) model:

$$\text{For } \psi \geq 0: \ S = 1.0, \ k_r = 1 \tag{2.4}$$

$$\text{For } \psi < 0, \ k_r = \sqrt{S_e}[1 - (1 - S_e^{1/m})^m]^2 \tag{2.5}$$

where S_e is the effective saturation ratio given by:

$$S_e = \frac{S - S_r}{1 - S_r} = \left[\frac{1}{1 + (\alpha | \psi |)^n} \right]^m \tag{2.6}$$

where $m = 1 - \frac{1}{n}$, S_r is the residual saturation, α [L^{-1}] represents the characteristic pore size of the beach soil, and higher α values imply a coarser material. The inverse of α provides an estimate of the capillary fringe (zone of considerable moisture above the

water table). The term *n* represents the uniformity of the pores and higher values of *n*

imply a more uniform pore-size distribution (van Genuchten, 1980).

The solute transport equation used is the well-known convection-dispersion

equation. In the absence of source/sink term, it can be written as (Boufadel et al., 1999a;

Boufadel, 2000):

$$\phi S \frac{\partial c}{\partial t} = \beta [\nabla \cdot (\phi S \tau D_m \nabla c) + \nabla \cdot (\mathbf{D} \nabla c)] - \mathbf{q} \cdot \nabla c \qquad (2.7)$$

where $\nabla = \left(\dfrac{\partial}{\partial x}, \dfrac{\partial}{\partial z} \right)$ is the gradient operator with respect to the spatial variables,

$\mathbf{q} = (q_x, q_z)$ [LT^{-1}] is the Darcy flux vector defined as:

$$\mathbf{q} = (q_x, q_z) = -\delta k_r K_0 \left(\frac{\partial \psi}{\partial x}, \frac{\partial \psi}{\partial z} + \beta \right) \qquad (2.8)$$

the term τ (dimensionless) is the domain tortuosity, D_m [L^{2}T^{-1}] is the diffusion

coefficient (molecular diffusion). The term $\mathbf{D}$ [L^{2}T^{-1}] in equation (2.7) represents the

dispersion tensor given by

$$\mathbf{D} = \frac{1}{\|\mathbf{q}\|} \begin{pmatrix} \alpha_L q_x^2 + \alpha_T q_z^2 & (\alpha_L - \alpha_T) q_x q_z \\ (\alpha_L - \alpha_T) q_x q_z & \alpha_T q_x^2 + \alpha_L q_z^2 \end{pmatrix} \qquad (2.9)$$

where $\|\mathbf{q}\| = \sqrt{q_x^2 + q_z^2}$, α_L [L] and α_T [L] are the longitudinal and transverse dispersivities, respectively (Bear, 1972 pp. 614-615).

The governing equations (2.1) to (2.9) used in MARUN are designated as density-and-viscosity-dependent flows in two-dimensional variably saturated media. The equations are discretized in space by the standard Galerkin method, and integrated in time using backward Euler with mass lumping (Celia et al., 1990). The MARUN code has been used to reproduce previous well-known numerical results such as the Henry's problem of seawater intrusion (Boufadel et al., 1999a; Boufadel et al., 1999c; Croucher and O'Sullivan, 1995; Frind, 1982), and the Elder problem (Boufadel et al., 1999c; Elder, 1967). More documentation regarding the MARUN model is presented in Appendix A.

Table 2.2 Comparison of Model Parameters and Their Values Reported by Boufadel (2000) and used in the Numerical Simulations

Symbol	Definition	Dimension	Reported by Boufadel (2000)	Used in this study
α	Parameter of the van Genuchten (1980) model	1/m	12.5	18.5
n	Parameter of the van Genuchten (1980) model	-	3.5	4.1
α_L	Longitudinal dispersivity	m	0.0075	0.0085
α_T	Transverse dispersivity	m	0.0025	0.002
ε	Fitting parameter of density-concentration relationship	m^3/kg	7.44×10^{-4}	7.44×10^{-4}
K_0	Saturated hydraulic conductivity for freshwater	m/s	0.0075	0.0084
S_0	Specific storativity	m	0.0	0.0
S_r	Residual soil saturation.	-	0.01	0.01
ϕ	Sand porosity	-	0.36	0.36
τD_m	Product of tortuosity and diffusion coefficient	m^2/s	10^{-10}	10^{-10}

2.3.3 Experimental and Numerical Approach

Two experiments (Case 1 and Case 2) were designed and conducted to investigate the density effect on beach groundwater flow and solute transport paths. The maximum change of the solute (salt) concentration was 2.0 g/L for Case 1 and 34.0 g/L for Case 2. The salt in Case 1 acts as a tracer, as the numerical simulations revealed. The salinity variation of Case 2 was chosen to represent typical salinity variation on beaches at the coasts of the continental United States. The salt used in the experiments was a commercial grade of sodium chloride (NaCl).

2.3.3.1 Experiments. Prior to each of the experiments the tank was filled with salt water and was circulated through the tank until a uniform salt concentration was reached. Then, while conserving the same concentration for the corresponding case, the pressures at sensors PT1 and PT6 were set equal to 0.857 m and 0.831 m, respectively.

Each experiment started by introducing fresh water (tap water) to the left of the screen through the same manifold used to introduce salt water under the same constant-pressure boundary conditions. Because of the difference in water head between PT1 and PT6, the fresh water propagated in the beach toward the sea side, causing a reduction of the salinity in the beach. Fresh water was pumped through the manifold to the left tank whenever the reading at PT1 dropped by more than 0.2 cm below the design value of 0.857 m, and the pumping stopped whenever the reading at PT1 increased by more than 0.2 cm above the design value. The converse occurred at the right tank, where the mixed water was pumped out whenever the reading at PT6 increased by more than 0.2 cm above the design value of 0.831 m.

The open water levels on the left- and right-hand side boundaries were controlled by the readings at PT1 and PT6. The fluctuations of the pressure readings at PT1 and PT6 resulted from two reasons. The first reason was that 2 millimeters in pressure drop at PT1 were needed to activate the freshwater pump to introduce water into the left tank. The similar was true in the right tank where an increase of water level by 2 millimeters was needed to activate the outflow pump. The second reason for the fluctuations in the readings is due to voltage fluctuation in the data collection software.

The injected fresh water contained air bubbles, which increased the mixing in the open water in the left tank. The air bubbles rose vertically and there was no indication that they passed through the fine mesh screen and entered the sand. Salinity measurements at different heights to the left of the screen indicated that the open water there, was well mixed. Therefore, the reading at CM14 can represent the concentration left boundary condition.

2.3.3.2 Modeling. The mesh contained 46,965 nodes and 92,736 triangular elements; the spacing between nodes varied from 1.25 cm to 0.5 cm, being largest at $x = 0$, $z= 0$ and smallest at $x = 5$ m, $z = 0.65$ m. The time step for the numerical simulation was 15 s. The finer mesh and smaller time step were applied but the improvement in the results was not noticeable. The convergence criterion of pressure head for the Picard iterative scheme of MARUN code was CONVP $= 10^{-5}$ m.

Boundary conditions......... For the flow equation at the screen ($x = 0$), a Dirichlet boundary condition below the water level (in the open water of the left tank) is:

$$\psi(0,z) = H(\text{PT1}) - z[1 + \varepsilon\, c(\text{CM14})] \qquad (2.10)$$

where H(PT1) is the PT1 reading in meters of freshwater, c(CM14) is the concentration

of CM14, ε is the parameter in equation (2.2), and c is the salt concentration expressed

in grams of salt per liter of solution. Equation (2.10) represents a hydrostatic pressure

distribution for $\psi(0,z) \geq 0$ in the saturated zone. For $\psi(0,z) < 0$ (the unsaturated zone

above the water level in the tank) a no-flow Neumann boundary condition ($\left.\dfrac{\partial \psi}{\partial n}\right|_{x=0} = 0$)

was assigned.

On the right and upper boundaries which represent the beach surface, a Dirichlet

boundary condition was used:

$$\psi(x,z) = H(\text{PT6}) - z[1 + \varepsilon\, c(\text{CM13})], \quad \text{if } \psi(0,z) > 0 \qquad (2.11)$$

As the seepage face observed in the experiment was only 4 cm, smaller than the

horizontal mesh size, it was not modeled in the simulations.

For salt concentration at $x = 0$ and the beach surface, for $\psi(0,z) \leq 0$ (on the beach

surface higher than the right water level including the seepage face), $\left.\dfrac{\partial c}{\partial n}\right|_{x=0} = 0$

(Neumann). For $\psi(0,z) > 0$ (boundary submerged by the open water) a Dirichlet

boundary condition was assigned with $c(0, z) = c(\text{CM14})$ at $x = 0$ and $c(x, z) = c(\text{CM13})$

on the beach surface as the outflowing boundary condition (Park and Aral, 2008) did not

provide results that agreed well with observations. This boundary condition is discussed further by Boufadel et al. (1999a).

Initial conditions.   The initial pressure head and concentration distributions were obtained by running the MARUN model from an approximate initial condition until steady state was achieved.   The water levels in the left and right tanks were $[0.857/(1+\varepsilon c)]$ m and $[0.831/(1+\varepsilon c)]$ m, respectively. The concentration throughout the tank was equal to 2.0 g/L for Case 1 and 34.0 g/L for Case 2.

2.4   Results and Discussion

2.4.1 Experimental Results

The observed concentrations and pressure heads are presented in Figure 2.2 and Figure 2.3 for low and high salinity cases, respectively. Figure 2.2a shows how the observed concentrations dropped with time for Case 1 (low salinity case) at three groups of Conductivity Meters {CM3, CM4, CM5}, {CM7, CM8, CM9}, and {CM10, CM11, CM12, CM13}. The first two sensor groups are located onshore and the third, offshore. In addition, sensors in each of the first two groups have the same *x*-coordinates.

In Figure 2.2a, the time order for the fresh water front to arrive at the sensors is: CM3 ≤ CM4 < CM5, CM8 ≈ CM7 < CM9. The readings at CM3 and CM4 were very close, so were those at CM7 and CM8, indicating a freshwater front moving seaward that is almost vertical. The delay of CM5 and CM9 is due to the proximity of the upper sensors to the water table, where the unsaturated zone filled with saltwater initially acted as a source of salt, causing a sustained high value of salinity near the water table.

Figure 2.3a shows the decrease in concentrations =with time for Case 2 (high salinity case) at three groups of Conductivity Meters {CM3, CM4, CM5}, {CM7, CM8, CM9}, and {CM10, CM11, CM12, CM13}. The time order for the fresh water front to arrive at the sensors in Figure 2.3a is almost reversed compared with that in Figure 2.2a: CM5 ≤ CM4 < CM3, CM9 < CM8 < CM7, indicating buoyancy effect where the light freshwater occupied the top portion of the beach and is underlain by the heavier saltwater.
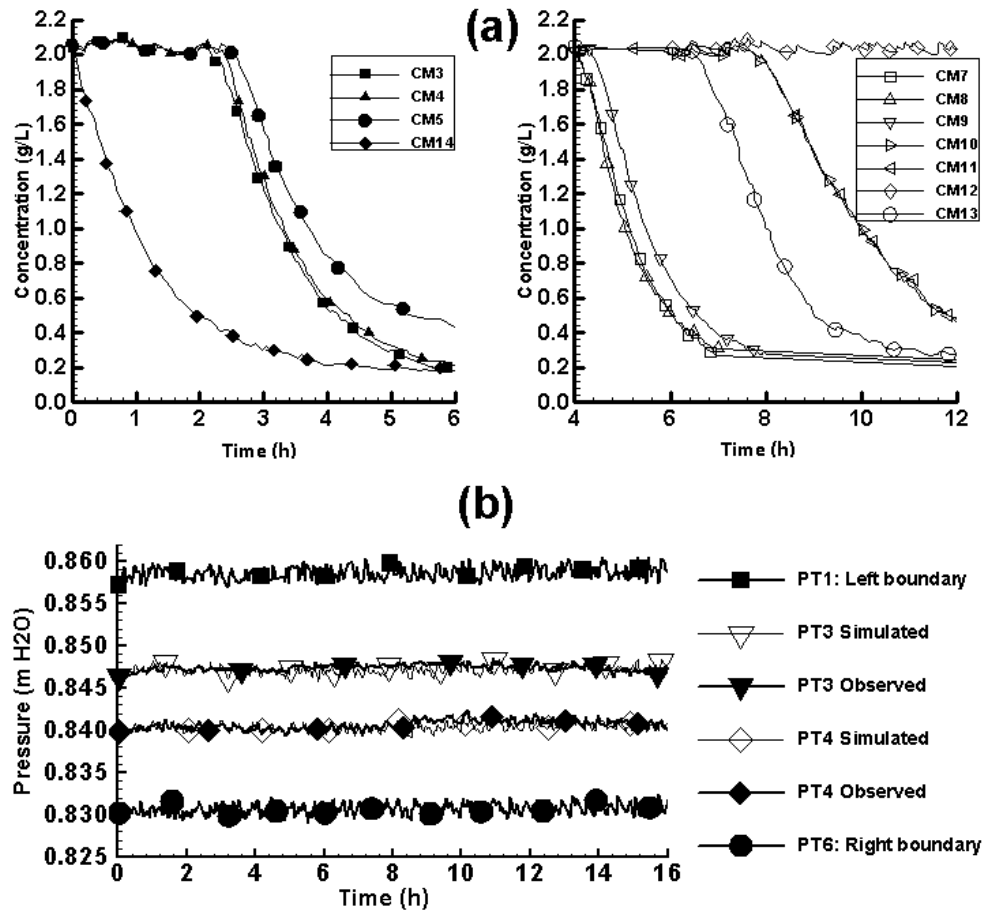
Figure 2.2 (a) Observed concentration dropping with time for Case 1 (low salinity case) at three groups of Conductivity Meters {CM3, CM4, CM5, CM14}, {CM7, CM8, CM9}, and {CM10, CM11, CM12, CM13}. Readings at CM13 and CM14 served as the right and left boundary conditions for concentration, respectively. (b) Simulated versus observed pressures at four Pressure Transducers (PT1, PT3, PT4, and PT6) for Case 1 (low salinity case). The pressure head at each Pressure Transducer was calibrated by taking the tank bottom as the datum.
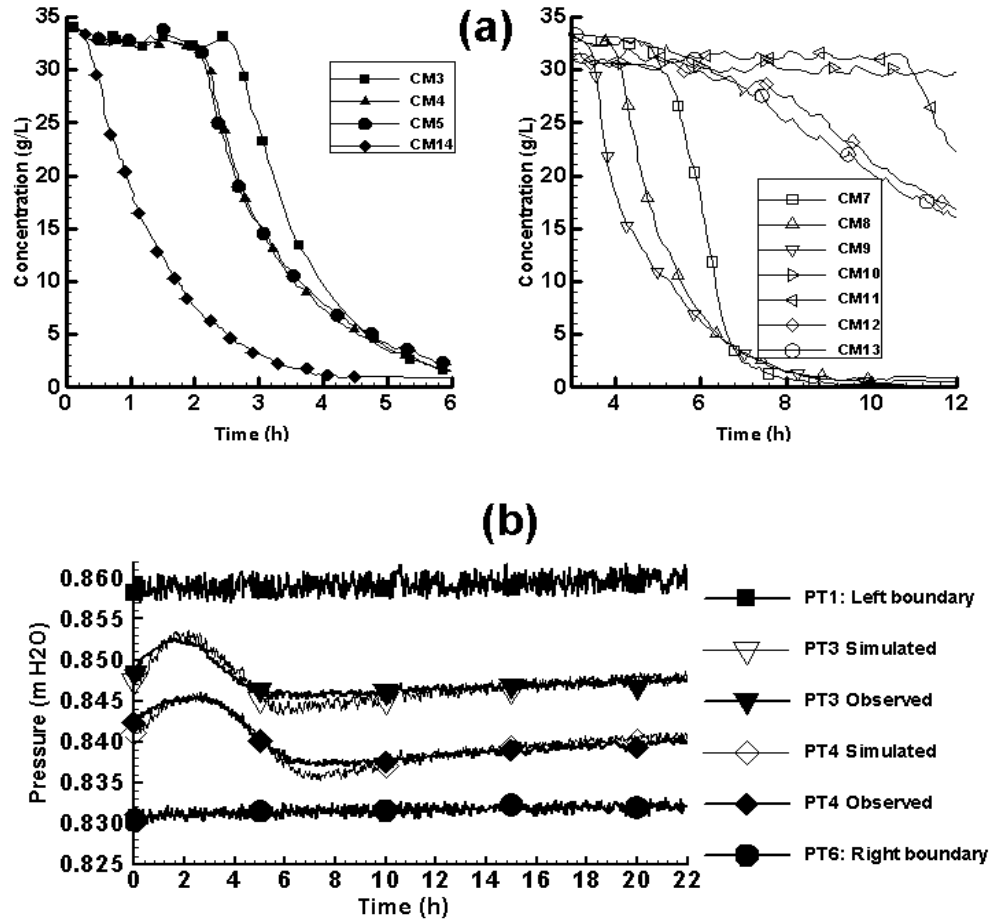
Figure 2.3 (a) Observed concentration dropping with time for Case 2 (high salinity case) at three groups of Conductivity Meters {CM3, CM4, CM5}, {CM7, CM8, CM9}, and {CM10, CM11, CM12, CM13}. Readings at CM13 and CM14 served as the right and left boundary conditions for concentration, respectively. (b) Simulated versus observed pressures at four Pressure Transducers (PT1, PT3, PT4, and PT6) for Case 2 (high salinity case). The pressure head at each Pressure Transducer was calibrated by taking the tank bottom as the datum.

It is also important to note that, for both low and high salinity cases, the readings at CM10 and CM11, which were offshore dropped much slower than those at CM9 and CM13 (open water on the right-hand side). This indicates that fresh water leaves the beach near the coastline, and only a very small horizontal (seaward) flow occurs seaward of that point. This was supported by visual observation, through the transparent wall of the tank, of sand erosion (due to high flow) that occurred only around the coastline. The erosion of the sand was in the order of 0.5 cm in elevation (5 cm in horizontal length).

Because a constant concentration in the sea was not achievable experimentally, the concentration in the sea decreased due to dilution by the incoming freshwater. However, this did not significantly affect the concentration in the beach because the flow velocity in the offshore beach (i.e., seaward of the water line) was much smaller than that in the onshore beach.

The pressures at PT3 and PT4 for the high salinity case (Figure 2.3b) behaved very differently from the low salinity case (Figure 2.2b). While the pressures at PT1 and PT6 were constant (by design), the pressures at PT3 and PT4 exhibited strong variations of about 0.5 cm. These variations were large and were equal to 20 percent of pressure head difference across the beach which was equal to (85.7-83.1=) 2.6 cm (freshwater column). These "humps" were the result of the continuous introduction of the freshwater plume in the tank behind the screen under constant pressure at PT1. In fact, the introduction of freshwater in the tank will lead to the increase of the water level there, because the water density drops while the pressure at PT1 remains practically constant (not accounting for the fluctuations). The initial water level equals $[85.7/(1+\varepsilon c)] = 83.6\,cm$, where $c = 34.0$ g/L, and the final water level equals 85.7 cm (when there is only freshwater in the tank). Thus, the total water level increase in the left tank during the experiment is about 2.1 cm. The increase of the water level in the left tank caused the diluted water to enter the beach above the existing water table, while the pore water below the water table was still at the high initial concentration of about 34.0 g/L. This explains why the measured pressure at PT3 and PT4 rose during the initial stage of the experiment. When the freshwater front moved seaward, the salinity of the pore water above the transducers was replaced with freshwater. Therefore the density

and consequently, the measured pressure at PT3 and PT4 after the initial rise decreased. This fact can be verified from the readings of PT3 (in Figure 2.3b), CM3, CM4, and CM5 (in Figure 2.3a), which are located approximately at the same vertical cross section. At t = 5 h, the salinity at CM3, CM4, and CM5 became essentially negligible (less than 4.0 g/L) in Figure 2.3a, and the reading at PT3 stopped dropping in Figure 2.3b. The reading at PT4 stopped dropping at about t= 6 h (Figure 2.3b), indicating that the salinity in the pore water above PT4 became negligible after about 6 hours of the experiment. The pressure hump is investigated in detail later using numerical simulations.

2.4.2 Numerical Modeling

A good fit was achieved between the simulated and the observed pressures and concentrations, as shown in Figure 2.2b and Figure 2.4 (Case 1), and Figure 2.3b and Figure 2.5 (Case2). The parameters' values are reported in Table 2.2 which shows that they are close to those obtained by Boufadel (2000). Figure 2.6 shows the simulated spatial distribution of concentration and the Darcy flux at t = 4 h and 8 h, for the low salinity case (Case 1). The freshwater seems to propagate seaward as a vertical front in the beach, except near the water table, where the contours become more curved. This is consistent with measurements, where the observed delay of the concentration decreases at CM5 with respect to CM3 and CM4, and at CM9 with respect to CM7 and CM8 (Figure 2.2a). This indicates that neglecting unsaturated flow in modeling would result in an erroneous solute distribution near the water table.
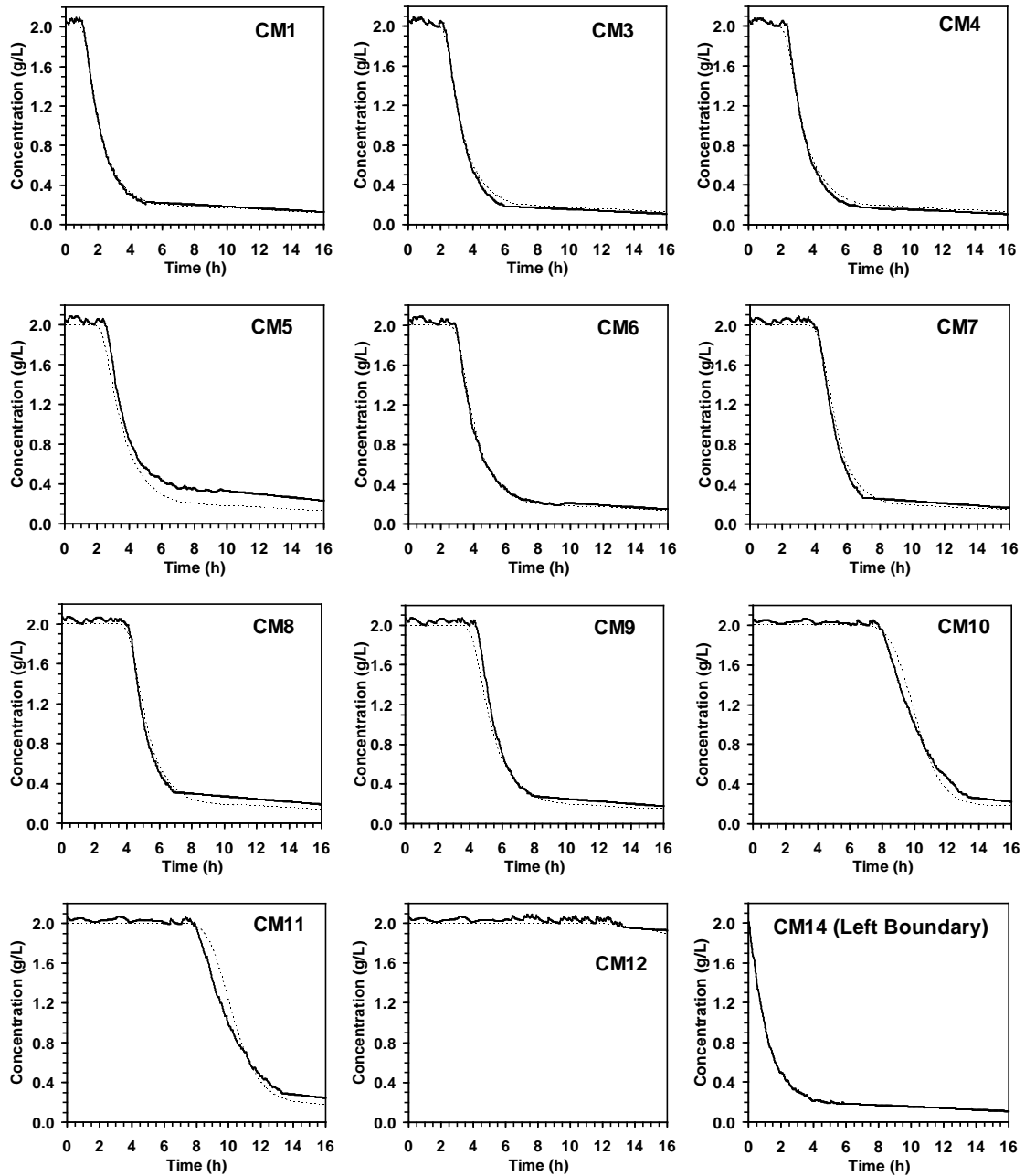
Figure 2.4 Simulated versus observed concentrations at 12 Conductivity Meters (CM1, CM3, CM12, and CM14 for Case 1 (low salinity case). The dashed lines in the concentration figures are the simulation results.
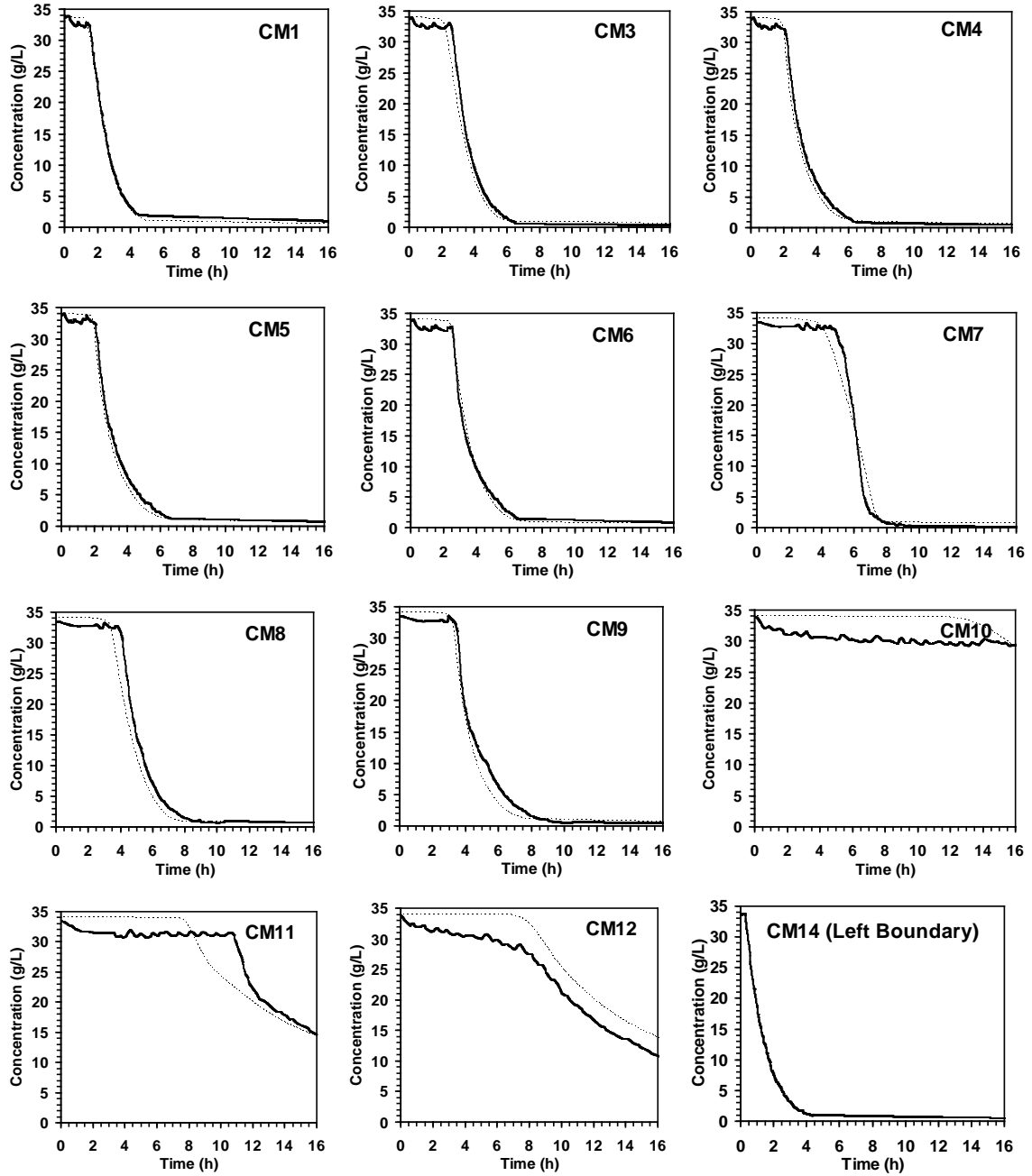
Figure 2.5 Simulated versus observed concentrations at 12 Conductivity Meters (CM1, CM3, CM12, and CM14) for Case 2 (high salinity case). The dashed lines in the concentration figures are the simulation results.
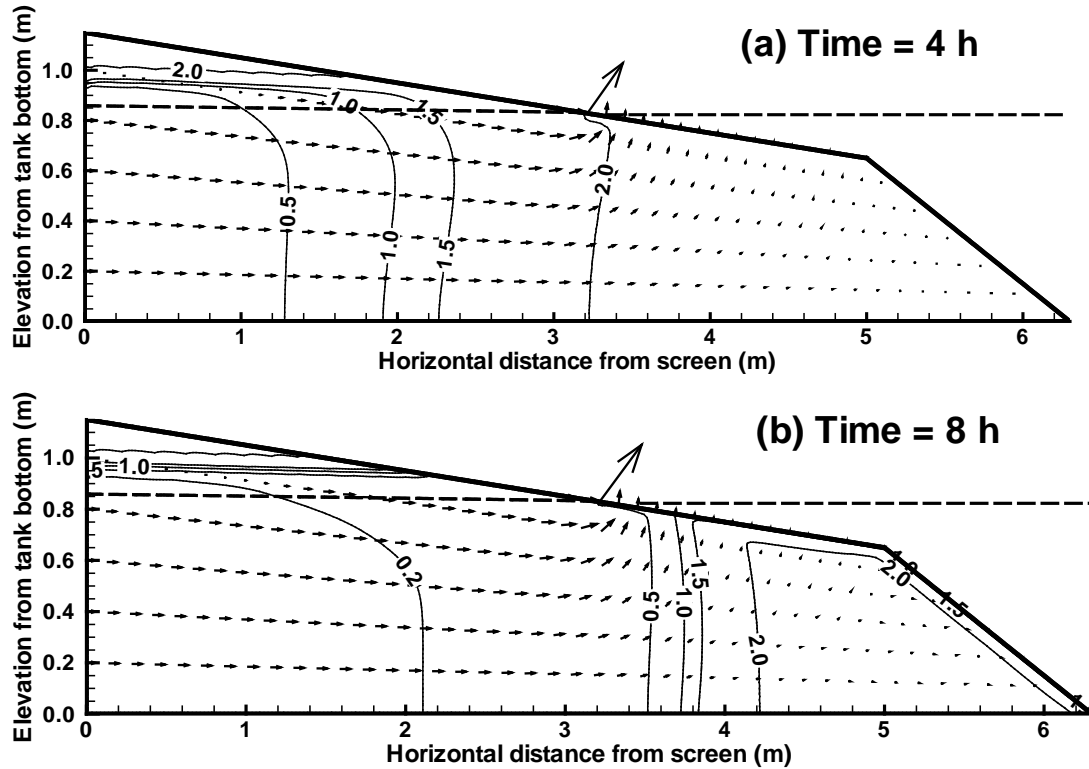
Figure 2.6 Simulated concentration contours (in g/L), Darcy velocity field (arrows), and water table or open water level (dashed lines) for Case 1 (low salinity case) at (a) $t = 4$ hour and (b) $t = 8$ h.

The large magnitude of the Darcy flux around the water line (i.e., the intersection point of the water table and the beach surface) shows that most of the water leaves the beach around that location. This also explains why the concentration at CM13 (open water on the right-hand side) decreased to approximately 1.0 g/L at $t = 8$ h, while the concentrations at CM10, CM11, and CM12 were still at their maximum (initial) values (Figure 2.2a). The significant reduction of the Darcy flux seaward of the exit point occurred because the total head in that region is almost uniform, as imposed by the open water above it. Thus, water leaving the beach would take the shortest path, which is upward instead of seaward where there is more resistance through the sand.

Figure 2.7 shows the spatial distribution of concentration and the Darcy flux at $t =$ 4 h and 8 h, for the high salinity case (Case 2). The salinity distribution in Figure 2.7 is different from that in Figure 2.6; the development of the freshwater/saltwater interface in Figure 2.7 is much clearer than that in Figure 2.6 and a clear salt wedge was formed at the bottom of the domain for the high salinity case. Interestingly, the effect of buoyancy seems to be stronger during transient regime (t=4.0 h) in comparison with the steady state (t=8.0 h and larger). The diffuse saltwater wedge was much larger at t = 4.0 h, indicating that neglecting buoyancy effects at that time would result in a higher error compared to that at steady state.
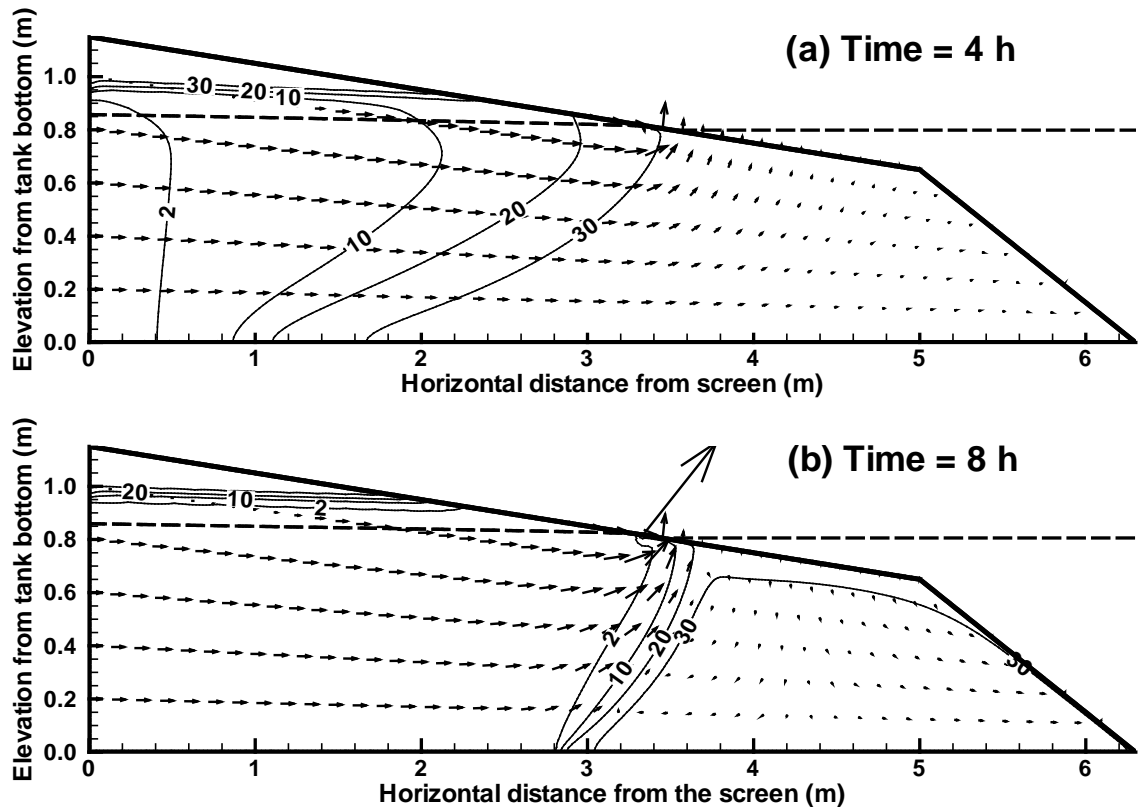
Figure 2.7 Simulated concentration contours (in g/L), Darcy velocity field (arrows), and water table or open water level (dashed lines) for Case 2 (high salinity case) at (a) t= 4 hour and (b) t= 8 h. Buoyancy effects are noted, especially at early time (t=4 hour).

For all cases, the velocity vectors landward of the exit point (coastline) are at least one order of magnitude greater than those seaward of the exit point. This indicates a very limited flow in the offshore beach aquifer, which acts approximately as an impermeable layer for the seaward flow forcing the water to move more upward towards the beach surface near the coastline.

To investigate the behavior of the freshwater front in Case 2 as it propagated seaward, the vertical cross section passed through PT3 was studied. Figure 2.8 shows how the pressure head and the concentration changes with time at four elevations located on that cross section. The pressure head at $z = 0.836$ m increased from negative values to become positive as the concentration decreased, indicating that the pore space at that location was unsaturated (with water) before the freshwater front arrived and the water table rose. The pressure variation range was greatest at $z = 0.836$ m (about 2.0 cm), and decreased with depth, reaching about 0.5 cm at the bottom. As the depth increases, the pressure increase caused by the rising water table was counteracted by the pressure decrease caused by the decrease in density, and resulted in the smallest variation range of about 0.5 cm.

It can be also observed from Figure 2.8 that the lower the elevation, the later the arrival time of the freshwater front (the time when the concentration drops). This is due to the buoyancy effect which will be detailed in the following subsection. The pressure head at a given point in the absence of the vertical flow depends on the water density and depth of the saturated pore water above it. When the freshwater front was propagating seaward the density decreased, but the depth of the saturated pore water increased due to the rising of the water table. The decrease in density tends to decrease the pressure head,

while the rising of the water table tends to increases it. At the highest point ($z = 0.836$

m), the depth of the saturated pore water is zero, or very small. In this case, the pressure

head was not influenced by dropping of the density, and it increased with rising of the

water table. At the bottom of the tank ($z = 0.0$ m), the depth of the saturated pore water is

the higher. In this case the pressure was influenced by both the decrease of the density

and the rise of the water table.
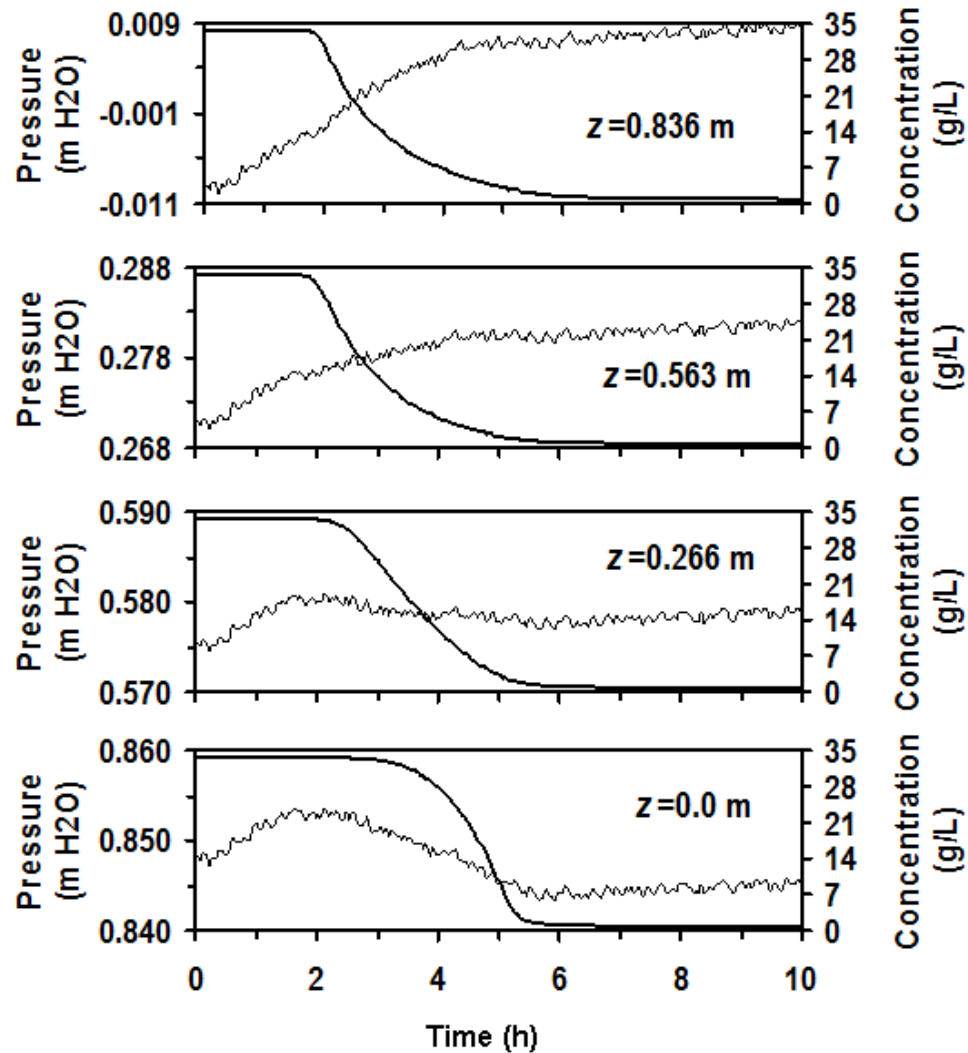
Figure 2.8 Variations of pressure head (thin solid lines) and concentration (thick solid lines) with time at different elevations of $z =0.0$ m, 0.266 m, 0.563 m, and 0.836 m (from bottom to top) along the vertical cross section passed through PT3 ($x=1.47$ m) for Case 2 (high salinity case).

Figure 2.9 reports the variations of water table, pressure head and the average concentration with time at the vertical cross section passed through PT3. From t=2 h until t=3.5 h, the water table rose, but the density remained unchanged or decreased only within the upper small portion of the cross section, so the pressure increased. When most of the freshwater front passed the cross section (t≈6 h), the rate of rising of the water table became slow, while the density decreased in most of the cross section so that the pressure stopped increasing and then began decreasing. This clearly explains the reason for forming the pressure humps.
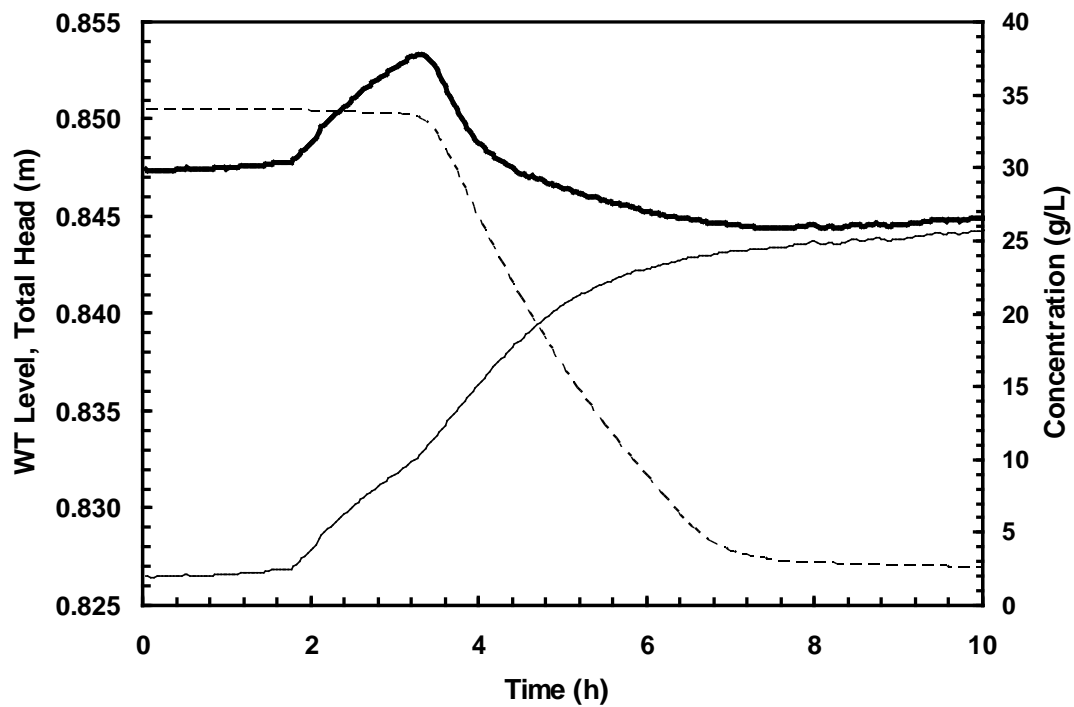
Figure 2.9 Variations of pressure head (thick solid line), water table (thin solid line), and average concentration (thin dashed line) with time along the vertical cross section passed through PT3 (x=1.47 m) for Case 2 (high salinity case).

Figure 2.10 shows the distributions of concentration, and horizontal and vertical Darcy velocities along the vertical cross section passed through PT3 at different times of t = 0.0 h, 2.2 h, 4.3 h, 5.5 h, and 6.3 h for Case 2. At the initial time, the concentration is uniform along the cross section, there is no vertical flow (V_z = 0.0 m/d), and the horizontal Darcy flux is also uniform in the saturated portion (approximately when $z <$ 0.825 m). When t = 2.2 h, the concentration began dropping at a position located just below the water table. The horizontal Darcy flux reached its maximum value near the water table and decreased with depth. Considerable vertical Darcy flux occurred (although it is at least one order of magnitude smaller than the horizontal one). The negative V_z value indicates that the flow is downward, which was caused by the freshwater flushing over the original saltwater water table. As time elapsed, the drop in concentration occurs at points farther below the water table, and finally concentration became uniformly negligible in the saturated zone. The horizontal Darcy flux is highest at the water table when the freshwater front passed the cross section, and tended to be uniform in the saturated zone after the freshwater front passed the cross section. The most interesting phenomenon is the behavior of the vertical Darcy flux. It was downward (indicated by negative value of V_z) when t = 2.2 h, and became positive in the middle-elevation zone when t = 4.3 h and 5.5 h. This was caused by the decrease of the concentration (density) in the middle zone while the concentration at bottom of the tank remained significantly high. It finally tended toward zero as the concentration at the tank bottom also approached zero, as illustrated by the figure when t = 6.3 h. In the unsaturated zone, due to low water saturation, the Darcy flux was essentially zero and the concentration remained at the initial value (maximum concentration).
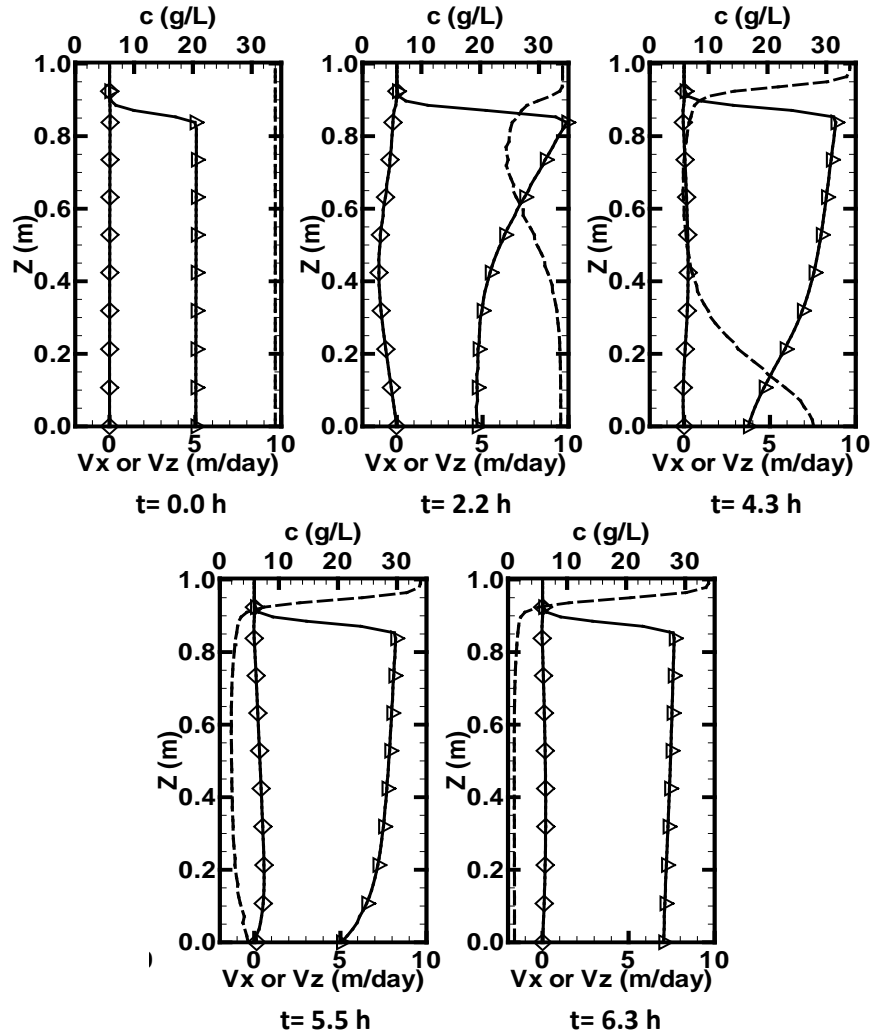
Figure 2.10 Distributions of concentration (dashed lines), horizontal Darcy velocity *Vx* (solid lines with right triangles), and vertical Darcy velocity *Vz* (solid lines with diamonds) along the vertical cross section passed through PT3 at different times *t* =0.0 h, 2.2 h, 4.3 h, 5.5 h, and 6.3 h for Case 2 (high salinity case).

Idealized Scenarios

An idealized scenario was designed to investigate how the rate of salinity drop at the left tank affects the pressure "hump". In this scenario it was assumed that the concentration at the left tank drops from its maximum value (34 g/L) to zero instantaneously, after 1 h, 2 h and 4 h (Figure 2.11a). Figure 2.11b and Figure 2.11c show the effect of time lag on the pressure head at a vertical cross section passed through PT3 and PT4, respectively.

The maximum pressure value is decreasing as the time lag increases for both PT3 and

PT4. However, the difference between the maximum pressure values for two cases (no

time lag and 4 h time lag) is relatively larger at PT3 compared to PT4 (Figure 2.11b and

Figure 2.11c). This is because the PT3 is closer to the left tank and concentration
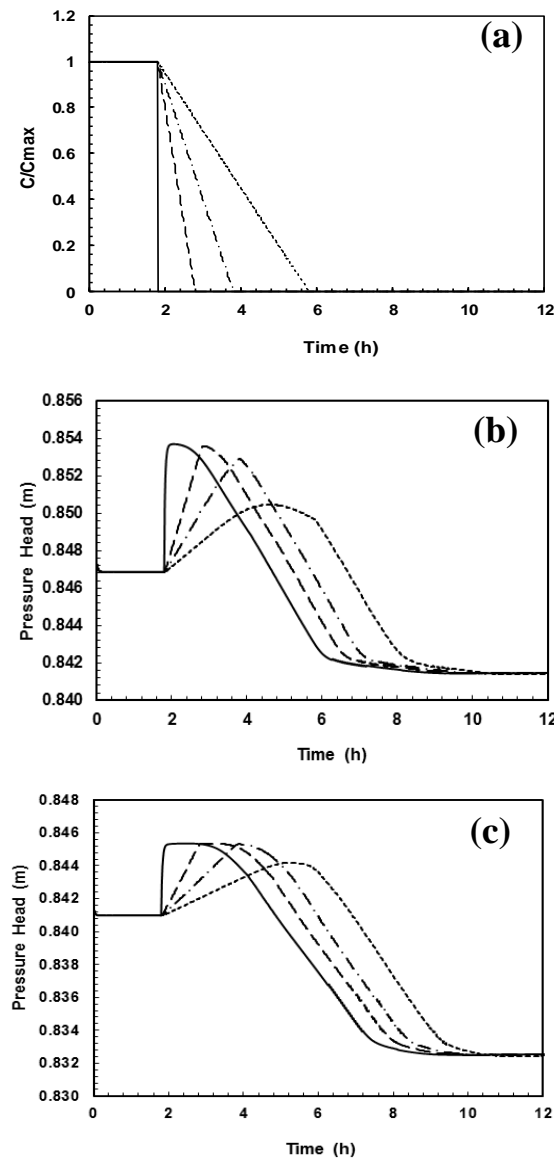
Figure 2.11 Time lag graphs for (a) concentration drop at left tank, (b) pressure head at PT3, and (c) pressure head at PT4. The time lags are 0 (thick solid lines-concentration drops instantaneously), 1 h (dashed lines), 2 h (dashed-dotted lines), and 4 h (dotted lines).

variations play a more important role in forming the pressure hump. In other words, landward locations of the beach are more sensitive to the sudden changes in the salinity in the left tank (say freshwater recharge). This shows that in a real system, the rate that the freshwater enters a beach after a storm has influence on forming the pressure hump.

To investigate the effect of salinity on the final distribution of the salt in the beach, another idealized scenario was designed and simulated numerically. In this scenario, four values (2 g/L, 10 g/L, 25 g/L and 34 g/L) were chosen for sea water concentration. Same hydraulic gradient was selected for all four cases. To set the same hydraulic gradient, the water levels in the left tank and the sea side were equal to 0.855 m and 0.820 m, respectively for all cases. The left tank was filled completely with fresh water, so its concentration is zero for the whole simulation period. Similarly, the concentration at the "sea" did not change with time. In every simulation it was assumed that the beach was filled with seawater initially, then freshwater entered from the left tank and propagated in the beach due to the hydraulic gradient. The simulations continued until the steady state situation was reached.

In Figure 2.12, the water table and the freshwater/seawater interface for different cases were compared. The figure shows that freshwater/seawater interface moves farther seaward for the lower salinity cases. The interface shape for the high salinity case was relatively close to what can be predicted by Ghyben-Herzberg approximation (Freeze and Cherry, 1979 p 376). Based on the Ghyben-Herzberg formula, the depth of the interface below sea level is 40 times the height of the fresh water table above it. The simulation results showed that this ratio was equal to 48 for the high salinity case. One of the main reasons for the difference between these two values is that the Ghyben-Herzberg

approximation is based on a vertical sea-land interface but here the beach has only a 10% slope. Also, Ghyben-Herzberg assumed a simple case in which freshwater and seawater are at the static equilibrium, while the dynamic equilibrium is dealt with in the simulations. For the low salinity cases, this ratio could not be calculated because when the difference between seawater and freshwater densities decreases, the freshwater/seawater interface becomes more vertical, and the experimental beach is not deep enough to allow us to do this calculation.
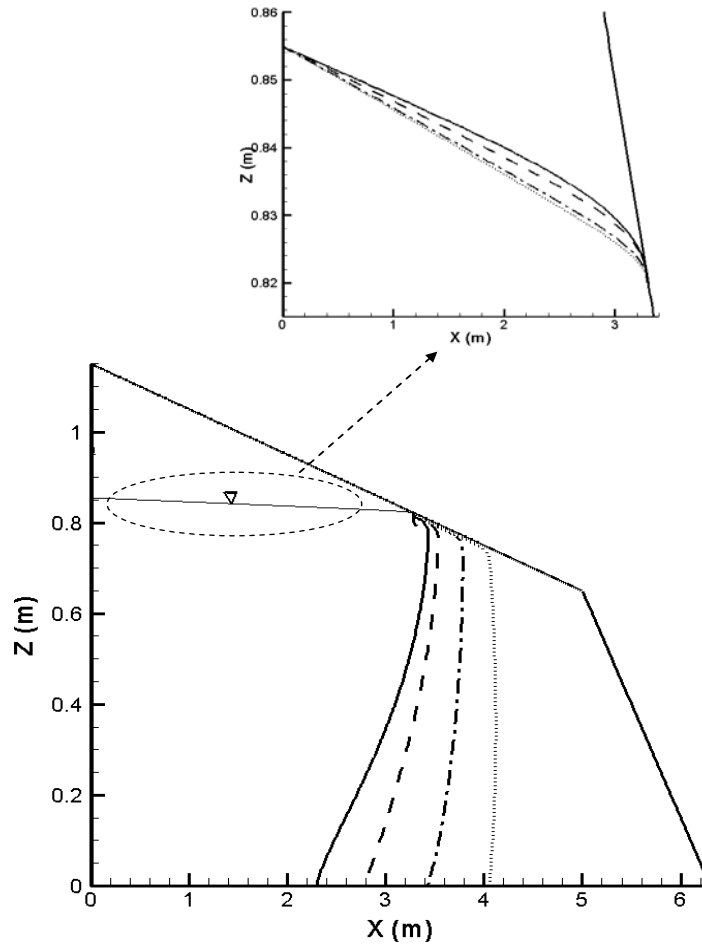
Figure 2.12 Comparison of water table and freshwater/seawater interface for different seawater concentrations in the idealized case. The seawater concentrations are 34 g/L (solid lines), 25 g/L (dashed lines), 10 g/L (dashed-dotted lines), and 2 g//L (dotted lines).

In Figure 2.13 the water table difference between the low salinity case (2 g/L) and high salinity cases are compared. Based on this figure, higher levels of seawater concentration lead to higher water table. It can be also noted from Figure 2.13 that the maximum value of the water table moves farther landward as the salinity increases. The difference between maximum values of the water table is not proportional to the salinity difference. This reflects the highly nonlinear behavior of the system.
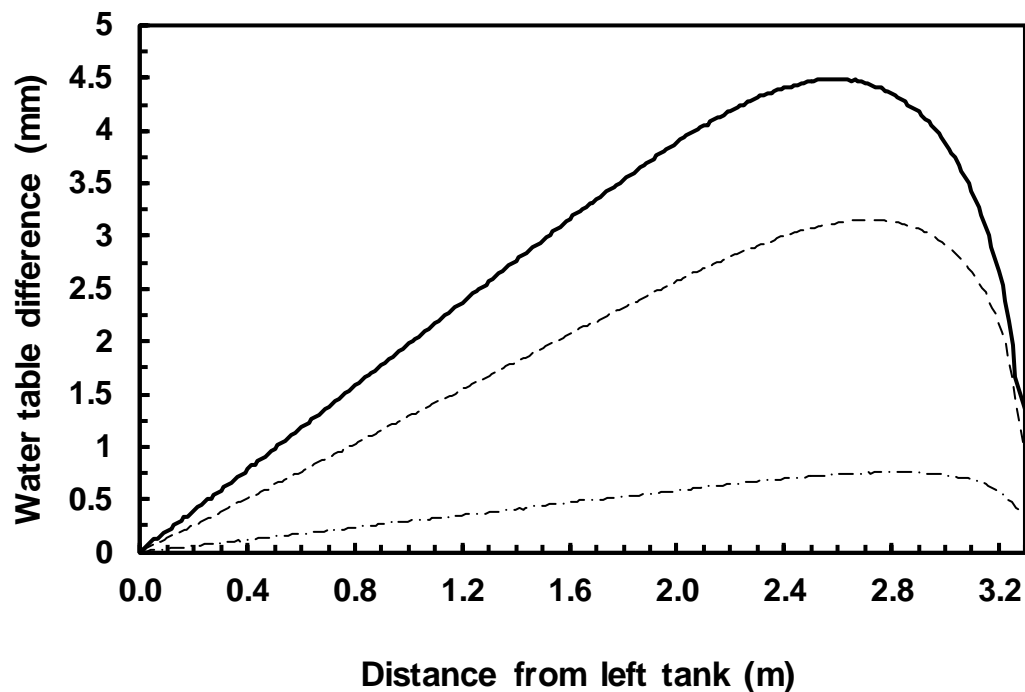
Figure 2.13 Water table differences between the low salinity case (2 g/L) and higher salinity cases in the idealized scenario. The seawater concentrations for these cases are 34 g/L (solid line), 25 g/L (dashed line), and 10 g/L (dashed-dotted line).

Figure 2.14 presents the variation of the average horizontal volumetric flux with time at a vertical cross section passed through PT3. The final values at t=12 h were compared. Based on Figure 2.14, the seaward volumetric flux decreases with the

increase in salinity, and the difference between the 2 g/L case and that of 34g/L is about 20 percent.

Using a mass flux instead of a volumetric flow rate would decrease the difference by only two percentage points. Therefore, there is another factor affecting the flow, the hydraulic gradient. The hydraulic gradient between the left tank and the cross section passed through PT3 was equal to 7.52×10^{-3} for the high salinity case (34 g/L) and was equal to 9.50×10^{-3} for the low salinity case (2 g/L). Thus, the hydraulic gradient for the high salinity case was almost 20 percent smaller than that for the low salinity case, which explains the difference in average flux reported in Figure 2.14. As a result, the increase in seawater density by only 2 percent could lead to a decrease in the seaward flow rate by 20 percent, highlighting the nonlinear behavior of the system.
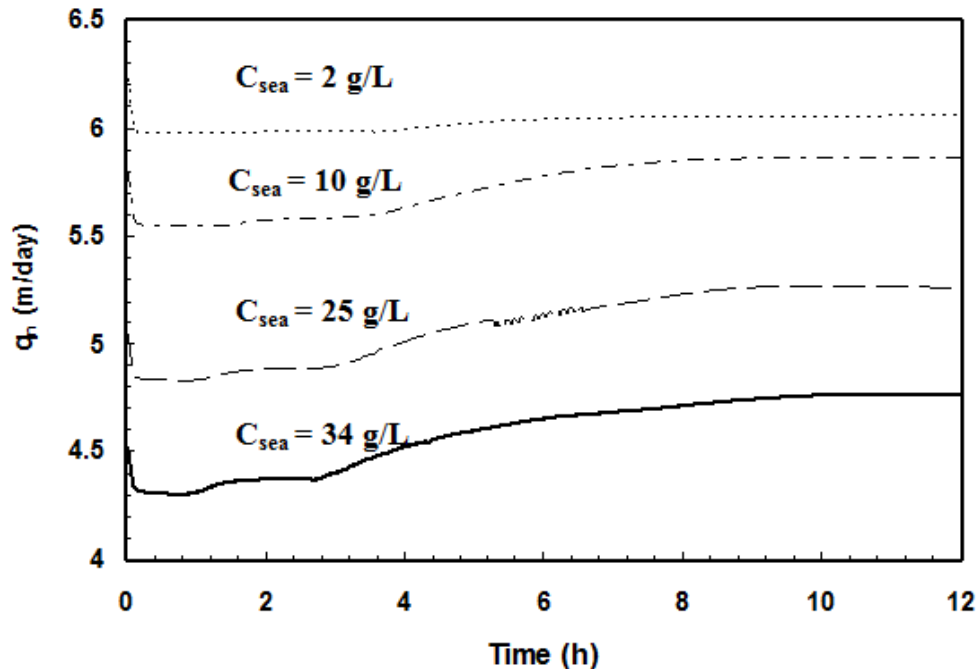
Figure 2.14 Average horizontal water flux at a vertical cross section passed through PT3 for different seawater concentrations. The seawater concentrations are 34 g/L (thick solid line), 25 g/L (dashed line), 10 g/L (dashed-dotted line), and 2 g//L (dotted line).

The impact of the capillarity above the water table on the pressures at PT3 and PT4 was investigated by conducting the simulation using a large α value of 92.5 m^{-1} (five fold of its normal value which corresponds to low capillary effect), while the other parameters remained unchanged. The simulated pressures at PT3 and PT4 (not shown) provided essentially the same results with humps about 0.5 cm high, indicating that the capillarity has no effect on the forming of the pressure humps.

2.5   Summary and Conclusions

Experiments were conducted to investigate the flushing of saltwater out of a laboratory coastal aquifer by freshwater propagating seaward. After a steady state distribution was achieved with a seaward hydraulic gradient, freshwater was introduced while keeping the bottom pressure constant, causing the propagation of freshwater. Two initial uniform concentrations were used: Case 1: 2.0 g/L (low salinity case), and Case 2: 34.0 g/L (high salinity case). The observed salinity and pressure data were closely reproduced using the MARUN numerical code (Boufadel et al., 1999a).

The results indicated that buoyancy plays an important role for Case 2 but is negligible for Case 1. The results also indicated that the flow in the offshore beach aquifer (submerged portion of beach) was negligible (low flow zone), compared to the flow in the onshore aquifer for both cases. The difference was strikingly large for the high density case. The landward extent of the low flow zone increased with the density difference between the seawater and the inland water; it was approximately vertical for a small density difference (Case 1). For the high salinity case the pressure increased with time until reaching a peak and then decreased (i.e., humps were formed). This was not

observed in the low salinity case. The investigations of this study indicated that the seaward propagation of the freshwater/saltwater interface resulted in the rise of the water table and a decrease of the pore water density in the saturated zone. The former tends to increase the pressure and the latter tends to decrease the pressure. However, as pressure fronts propagate faster than concentration fronts (because the water is incompressible), an increase in pressure occurred. As the freshwater arrived at that location, the density decreased causing a reduction in pressure.

The results showed that the water table increased with an increase in the seawater salinity for fixed water levels, landward of the aquifer and at sea. The increase was found to be superlinear as a function of the seawater density, reflecting the nonlinear dynamics of the system. Additionally, the seaward flow of freshwater increased with a decrease in the seawater salinity, and the increase was nonlinear as function of seawater density. For example, the discharge in the high salinity case was about 20 percent lower than that in the low salinity case.

The results of this chapter have important implications on the dynamics of saltwater flushing and the discharge location of an aquifer to its abutting open waters, such as rivers, lakes and sea where the waves and tides are negligible. It is concluded that if the slope of the beach surface is mild below the water surface, then the inland groundwater discharge will exit around the intersection of the surfaces of the open water and the interface. This gives useful guidelines related to the sampling location of the groundwater discharge into open waters using the seepage meter (see e.g., Taniguchi et al. (2006)).

CHAPTER 3

A FIELD INVESTIGATION OF WATER FLOW AND SOLUTE TRANSPORT IN A GRAVEL BEACH: EXPERIMENTAL WORK AND OBSERVATION DATA

3.1   General

During the summer of 2008 a field investigation for water flow and solute transport along an oiled transect (Left transect) and a clean transect (Right transect) of a tidal beach in Smith Island, Prince William Sound (PWS), Alaska was conducted. The goal was to understand hydrodynamic factors impacting beaches (especially gravel beaches) and then relate these factors to the disappearance of oil from an initially polluted area. In this chapter, field measurements of water table, pore water salinity and tracer (lithium) concentration are presented. Hydraulic conductivity of the beach sediments was estimated by analyzing the sediment samples in the lab and also by performing in-situ hydraulic conductivity tests.

Results indicated that the beach can be viewed as a two layer system from a hydraulic point of view with a high permeability layer underlain by a low permeability layer. This two-layer system could be one of the reasons for the oil persistence in this particular beach and also similar beaches in PWS. Based on the results, the freshwater recharge was larger in the clean transect (right transect) in comparison to that in oily transect. Hydrodynamic factors like freshwater recharge could contribute to the disappearance of the oil in the right transect.

3.2   Field and Laboratory Studies

3.2.1 Field Setup

The selected beach is located on Smith Island at the coordinates 147° 24' 13.84" W, 60°
31' 10.30" N (Figure 3.1a), around 11 km southeast of the beach investigated by Li and
Boufadel (2010) and 22 km northeast of the beach studied by Xia et al. (2010) and Guo et
al. (2010). The beach faces north, and is subjected to waves developed over a fetch of 60
km. The length of the beach across-shore is 120 m and its width along-shore is about 50
m. After the earthquake of 27 March 1964, this beach was uplifted about 1 to 2 m
(Plafker, 1969). The sediments throughout the beach are coarse, ranging from granules (a
few millimeters) to pebbles and cobbles (10-20 cm) interspersed between boulders (up to
100 cm). The rock of this area consists mainly of Orca Group turbidities (Orca Group
sedimentary rocks) (Lethcoe, 1990).

The sediments on the right side of the beach are more uniform in shape. The
labels "left" and "right", means the left and right side of the beach, respectively when an
observer is standing on the beach and is looking landward. The left side of the beach is
exposed to waves from northeast while a tombolo (protruding rock formation) shelters
the right side below the mid tide level. An armor layer of worked pebbles and clasts
covers most of the left side of the beach. As one moves seaward, that layer disappears
and a higher percentage of boulders emerges, and possibly an outcrop of the bedrock.
The range of neap tides was around 3.0 m and that of the spring tides was around 6.0 m.
Around 30 m landward of the high tide line, a freshwater pond is located close to the
right transect (Figure 3.2). The beach was subjected to extensive treatment (Page et al.
2008; Taylor and Reimer 2008). Oil persists on the left side of the beach between the

mid-tide line and the low tide-line (Figure 3.1b) at the amount considered to be Heavy

Oil Residue (HOR) according to the ASTM F1687-97, 2003 classification (see also

(Short et al., 2004)). The oil occupied a patch of sediments of approximate dimensions:

6.0 m x 6.0 m x 0.30 m (thickness). The oil was observed from 0.1 m to 0.4 m below the

surface.

(a)

(b)

(c)
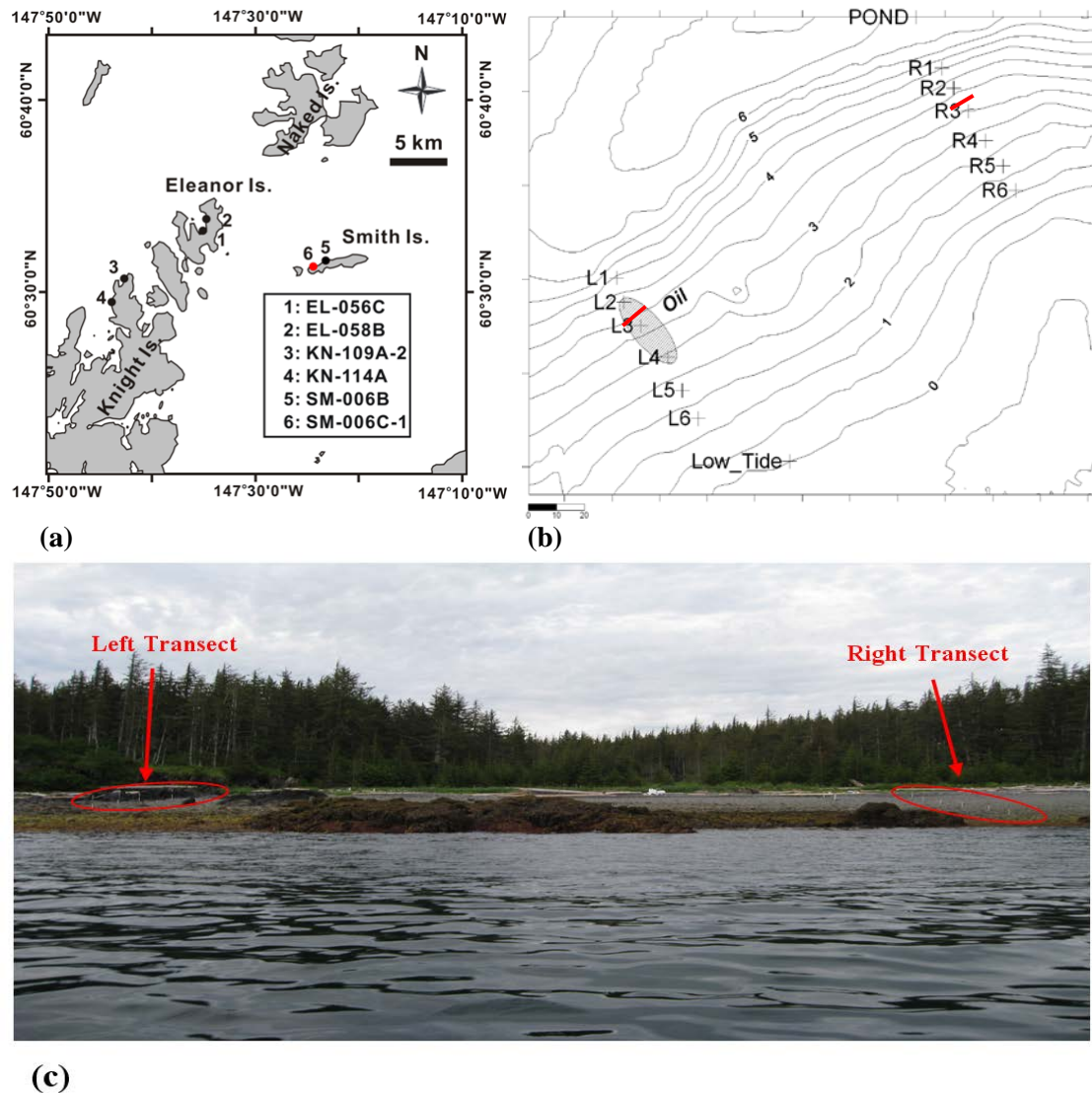
Figure 3.1   (a) Location of the selected beach (SM-006C-1) in Smith Island, Prince William Sound, Alaska. (b) Topographic contours of the beach and locations of twelve observation wells. The oil was found in the shaded area during the field study. The manifold for tracer application is represented by red lines at each transect. Well names begin with "L" for the left transect and with "R" for the right transect. All dimensions are in meters. (c) Site picture of left and transects.

(a)

(b)

Figure 3.2 (a) Aerial view of the pond. The red ellipse shows the estimated location of the Right transect. The arrow shows the location of the sensor (b) View of the pond looking landward
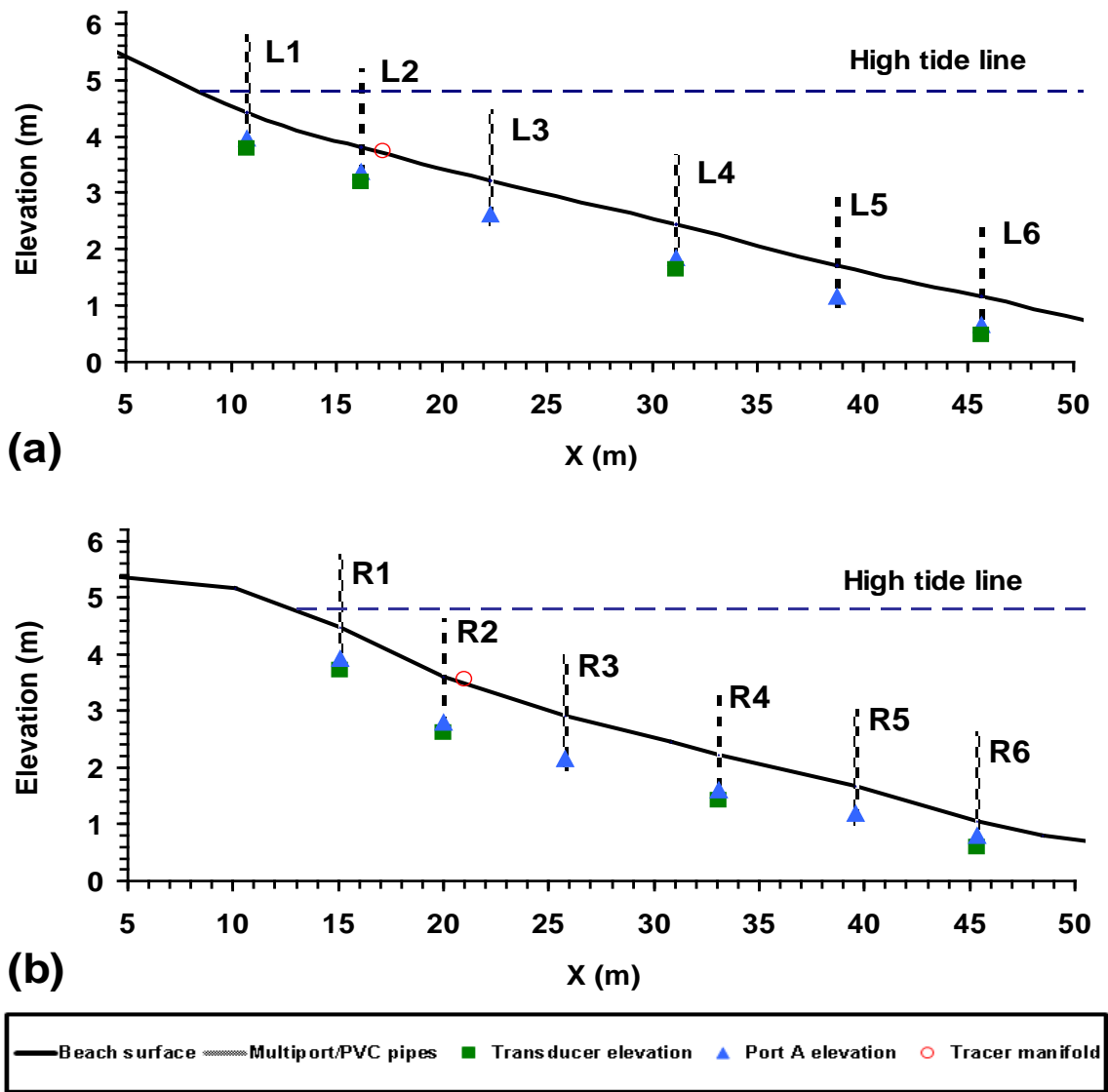
Figure 3.3 Schematic cross-section of (a) the left transect and (b) the right transect of the beach. Well locations and tracer application location are shown here. Square and triangle symbols show the location of pressure transducers and port A of multiports, respectively. The datum is the elevation of the lowest low tide during the field study.

Two transects of six monitoring wells were installed in each side of the beach (one in the oiled left side and one in the clean right side) to better understand hydrodynamic factors in the beach (Figure 3.1 and Figure 3.3). The average slope at the left and right transects in the intertidal zone (about 50 m) were 9% and 11%, respectively (Figure 3.3).

Due to the coarse structure of the sediments (Page et al. 2008), it was practically impossible for us to drive multiport sampling wells or sensors into the beach. Therefore, six pits were hand dug in each transect (L1-L6 along the left transect and R1-R6 along the right transect). The pits were dug to a maximum depth of 0.7 m and 1.0 m whenever possible in the left and right transects, respectively (see Table 3.1 for the depth of pits). The shallow rock formation on the left and the presence of larger boulders at depth on the right precluded deeper pits.

In each pit, a PVC pipe and a multiport sampling well were installed vertically (Figure 3.4). The pits were then refilled with the excavated soil. Effort was made to replace sediments back in the order they were extracted. The PVC pipe consisted of two pipes with a near tight fit. Both pipes were slotted across their whole lengths and there was a fine stainless-steel 100 mesh screen (with opening size of 0.0055 inch) between them to allow water passage while keeping out sediment. A pressure transducer (Mini-Diver, dataLogger-DL501, Schlumberger) was placed at the bottom of four of the PVC pipes (wells 1, 2, 4 and 6 at each transect) (Figure 3.4b) to record the water pressure and the water temperature every 10 minutes from 6/29/2008 3:30:51 PM (initial time t=0 in this research), with the recording duration of 89 hours. All the pressure readings were calibrated against the barometric pressure monitored by an air-pressure sensor (BaroLogger, DL-500, Schlumberger) during the same period. No rain or strong winds happened during the whole experiment.

The stainless-steel multiport sampling well contained four ports labeled A, B, C and D from the bottom up, which were covered with a fine stainless-steel screen to prevent blockage by fine sediments. The distance between any two adjacent ports is 23

cm. The elevations of ports and sensors for different wells are listed in Table 3.1. Each port was connected to a stainless-steel tube that extended to the top of the well where it was connected by means of Tygon tubing to a luer lock three-way valve. Figure 3.4b shows a schematic vertical cross section of R4 after the installation of multiport and PVC pipe.

Table 3.1 Elevations of Beach Surface, Sensors, and Ports at Different Locations

Locations	x (m)	Surface elevation (m)	Sensor elevation (m)	Pit depth (m)	Port elevation (m)		
					Port A	Port B	Port C
L1	10.75	4.74	4.18	0.64	4.29	4.52	--
L2	16.14	4.13	3.65	0.62	3.70	3.93	--
LM	17.11	4.08	--	--	--	--	--
L3	22.31	3.53	--	0.77	2.95	3.18	3.41
L4	31.13	2.75	2.11	0.78	2.16	2.39	2.62
L5	38.79	2.03	--	0.73	1.49	1.72	1.95
L6	45.63	1.49	0.85	0.64	1.04	1.27	--
R1	15.09	4.81	4.18	0.76	4.24	4.47	4.70
R2	20.02	3.93	3.35	1.00	3.12	3.35	3.58
RM	21.04	3.87	--	--	--	--	--
R3	25.78	3.24	--	0.95	2.48	2.71	2.94
R4	33.08	2.54	2.10	0.75	1.98	2.21	2.44
R5	39.58	2.00	--	0.68	1.51	1.74	1.97
R6	45.38	1.38	0.89	0.45	1.10	1.33	--

Note: LM and RM denote the location of manifold from which the tracer was applied onto the beach surface at the left transect and right transect, respectively.
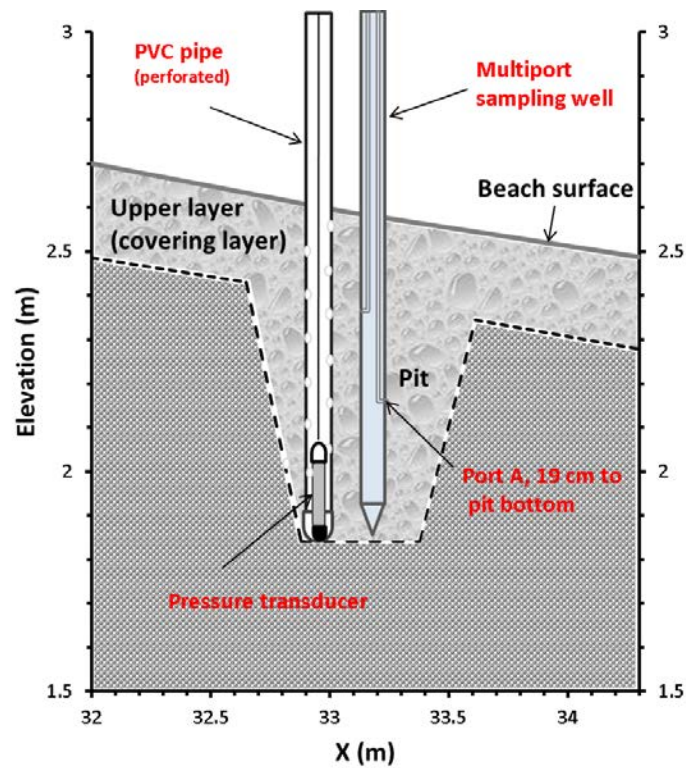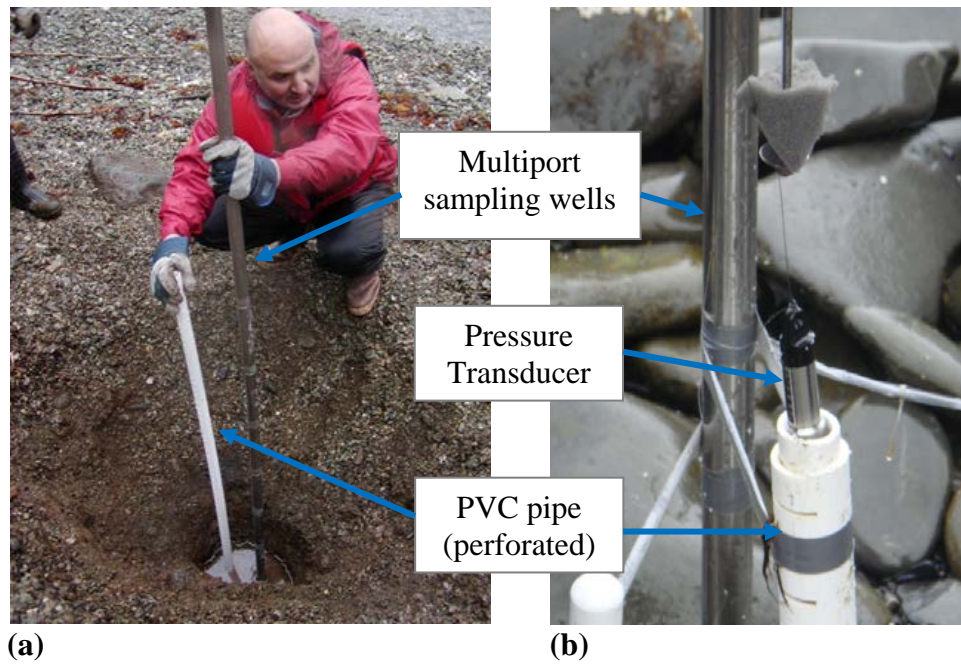
Figure 3.4 The multiport sampling well and the perforated PVC pipe at a pit (a) when they were being installed. Note the change in the material of the pit. The upper part consists of pebble and coarse sand while the lower part is made of compacted silt and fine sand. (b) The pressure transducer is programmed and ready to be deployed. (c) A schematic vertical cross section of the pit at R4.

Tracer studies were conducted by applying seawater solutions of lithium nitrate on the beach surface at the left and right transects simultaneously. The application occurred through manifolds placed approximately 1.0 meter seaward of L2 and R2 at both transects (Figure 3.1b). The manifolds were 5 m long, and perforated (2 mm diameter holes) along their lengths. The holes were turned upward, and the uniformity of the height of water jets was achieved by adjusting the elevation of the manifolds. The location of manifolds is indicated in Figure 3.3.

The application occurred during the falling tide. It was started at 07/01/2008 4:55 PM (t=49.1 h) and lasted for 2 hours and 4 minutes. The lithium nitrate was mixed in two tanks of seawater and the tracer solution for application was pumped from the tanks. The average concentration of the lithium nitrate solution was 3.55 g/L. The corresponding lithium concentration of tracer solution was 355 mg/L. The flow rate per unit length of the 5 m long manifold was 82 L/(h.m). During the tracer application, no ponding was observed on the beach surface. The sampling began immediately after tracer application.

Water samples (approximately 50 mL) were collected with 60-mL luer lock syringes from the multiport sampling wells and placed in 125-mL polyethylene bottles (Fischer Scientific, Fairlawn, NJ). After shipping the samples to the laboratory, the lithium concentration of the samples was measured by atomic absorption spectroscopy with an air-acetylene flame at 670.8 nm (210VGP Atomic Absorption Spectrophotometer, Buck Scientific, Inc). The salinity was measured using Digital Refractometer (300035, SPER SCIENTIFIC) for each of the samples, and then was

calibrated by subtracting the concentration of lithium nitrate from the sample concentration.

To minimize the unnecessary sampling, nitrate strips (Aquachek, Hack) with 1.0 mg/L sensitivity and a detection range of 0-50 mg/L were used. When the sample gave a concentration less than 5 mg/L (based on the discoloration on the strip), the sample was discarded. For this reason, only two samples were obtained from port A of R6. Also, because ports A and B of L6 drew air, no salinity or lithium samples were obtained from well L6.

It was not possible to place a sensor far offshore to measure the lowest low tide. Therefore in order to calculate the tide level ($H_{tide}(t)$), a theoretical expression of tide (Merritt,. 2004) was fitted to the observed water level at R6 using the least squared method. The theoretical expression is:

$$H_{\text{Tide}}(t) = h_{\text{MSL}} + \sum_{i=1}^{5} A_i \cos(\omega_i t + \varphi_i) \tag{3.1}$$

where h_{MSL} denotes the mean sea level, and the summation represents five harmonic components (O1, K1, M2, S2, and N2, see Table 3.2) for tides. The parameters A_i, ω_i and φ_i are the amplitude (m), frequency (radian/hour) and phase shift (rad) of the i-th component of tide, respectively. Although the theoretical expression for tide contains seventeen components, it was sufficient to use five components. The observed and simulated tidal levels are reported in Figure 3.5 and the mean sea level and the values of the five tidal components are listed in Table 3.2.

Table 3.2 Fitted Parameter Values for Tide

Harmonic component i	Amplitude A_i (m)	Phase shift φ_i (rad)	Explanation
1	0.453	0.133	Main lunar diurnal (O1), $\omega_1=0.243$ rad/h
2	-0.696	-1.467	Lunar-solar diurnal (K1), $\omega_2=0.262$ rad/h
3	-0.264	1.605	Main lunar semidiurnal (M2), $\omega_3=0.506$ rad/h
4	-0.437	2.014	Main solar semidiurnal (S2), $\omega_4=0.524$ rad/h
5	1.131	3.177	Lunar elliptic (N2), $\omega_5=0.496$ rad/h
$h_{MSL}=2.447$ m			Mean sea level

Source: Detailed explanations can be found in Table 4 of Merritt (2004).
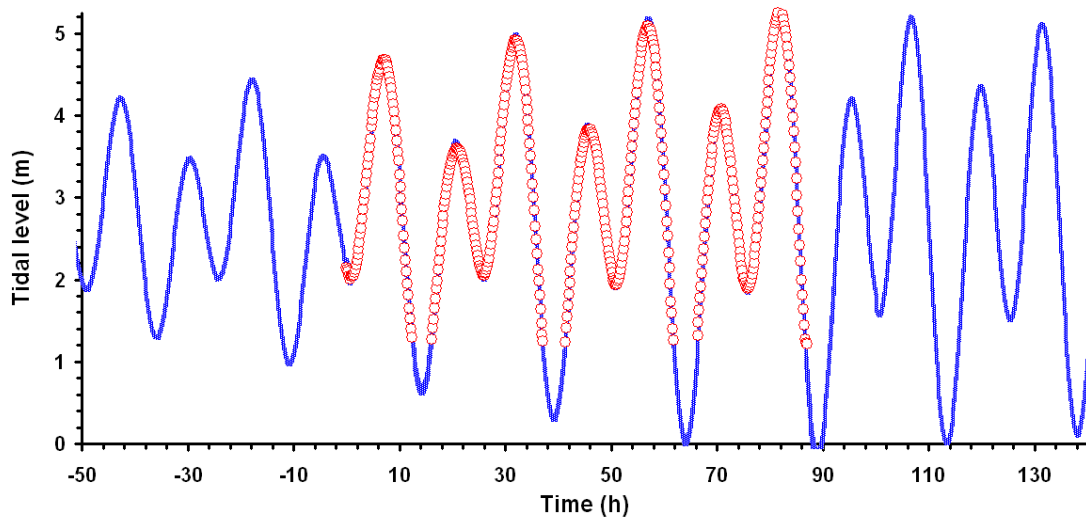
Figure 3.5 Observed water level above surface of R6 (circle symbol) and tidal level fitting results (line). Elapsed times are defined as number of hours since 6/29/2008 3:30:51 PM (the started time for field monitoring works, t=0 h). Tidal parameter values are also presented in Table 3.2.

3.2.2 Laboratory and Field Measurements of Sediment Properties

Twenty nine sediment samples were collected in the field to measure the saturated hydraulic conductivity for freshwater flow (K_0 in equation (2.1)) and also the capillary parameters (α, n and S_r in equation (2.6)). These parameters were used as prior information for the numerical model (MARUN model) and then were updated by calibrating the model (more details will be presented in the next chapter). The sediment samples (125 cm^3 to 750 cm^3) were obtained at three depths (30 cm, 60 cm, and 75-90 cm) at each well and were shipped to the lab for analysis. The porosity of the samples was measured in the lab using the water saturation method (Dullien, 1992).

In the lab, sediment samples were sieved to generate the grain size distribution according to the procedure ASTM D 422-63. Based on the grain size distribution, effective diameter (D$_{10}$) which is the grain diameters in (mm) corresponding to 10% passing on the cumulative grain-size distribution curve was calculated. The porosity and D$_{10}$ values were used to predict the hydraulic conductivity using the Kozeny-Carman equation (Carrier, 2003) which is presented below. A review of empirical formulae to yield hydraulic conductivity can be found in (Odong, 2007).

$$K = \frac{g}{v} \times 8.3 \times 10^{-3} \times \left[\frac{\phi^3}{(1-\phi)^3} \right] \times D_{10}{}^2 \qquad (3.2)$$

In this equation, g is acceleration due to gravity (g= 9.81 m/s^2), υ is kinematic viscosity (υ=1.0×10^{-6} m^2/s) and ϕ is porosity.

The capillary parameters were estimated by fitting the van Genuchten model (van Genuchten, 1980) to capillary retention experiment (Bear, 1972; Boufadel et al., 1998).

The van Genuchten model was presented in equation (2.4) to equation (2.6).

In addition to calculating the hydraulic conductivity of the sediments based on grain size distribution, in situ conductivity tests were performed at three close by locations at three different elevations. After digging a hole, a clear PVC pipe was placed in the hole and the annular space between the casing and the borehole was sealed with grout and sediment at top. Then, the falling head test was performed and the hydraulic conductivity was computed from the appropriate Hvorslev (1951) equation as follows (Bodocsi et al., 1994; Daniel, 1989):

$$K = \frac{\pi D}{11(t_2 - t_1)} \ln\left(\frac{H_1}{H_2}\right) \tag{3.3}$$

where K is the mean hydraulic conductivity (m/s), D is diameter of the pipe (m), t is the time (s), and H_1 and H_2 are the water head (m) in the pipe at t_1 and t_2, respectively.

The results of these measurements are presented in the next section.

3.3   Results

3.3.1 Sediment Properties

Based on the water saturation method, the average porosity of the samples was equal to 0.31 (Table 3.3). The porosity does not affect the water flow greatly (Sanford et al., 1993) so the average value was used in the numerical model (MARUN model, next chapter). The grain size distribution of the samples collected at different depths from each well is presented in Appendix B. Based on the grain size distribution, effective diameter (D_{10}) was calculated which is reported in Table 3.3. The hydraulic conductivity

at each well, estimated by the Kozeny-Carman equation (by taking the averaged D_{10} and porosity values) is also reported in Table 3.3. The average hydraulic conductivity at the left transect was equal to 2.6×10^{-3} m/s while it was equal to 2×10^{-3} m/s at the right transect. In addition, the maximum ratio of hydraulic conductivity on the left to that on the right was around 4 (for the most landward well), and the average ratio was around 1.0. Noting that the experimental uncertainty of the method is within five folds (half an order of magnitude), one concludes that the hydraulic conductivities of both transects are essentially the same.

Based on the in-situ hydraulic conductivity test that was conducted at three different elevations (20 cm, 65 cm and 70 cm deeper than the beach surface), the hydraulic conductivities were computed as 9.1×10^{-3} m/s, 1.4×10^{-6} m/s and 8.0×10^{-7} m/s, respectively. It is interesting that the hydraulic conductivity was four orders of magnitude smaller for a sample that was collected only 40 cm deeper. These results show that the hydraulic conductivity decreased with depth exponentially. Bobo et al. (2012) explored hydraulics in a gravel beach in PWS, Alaska and reported that the hydraulic conductivity and porosity decreases sharply with depth. This is probably because of more sediment compaction by increasing depth. Other researchers noted the decrease in the porosity with depth in the beaches of PWS (Page et al., 2008; Atlas and Bragg, 2009) and in other coastal aquifers (Briggs and Richardson, 1997; Kimura and Tsurumi, 2004).

For the same depth, the hydraulic conductivity calculated by the Kozeny-Carman equation was two to three orders of magnitude larger than the results of the in-situ test. The reason could be that the sediments were probably more compacted in the field than

after extraction and usage in the lab. The estimated hydraulic conductivity values based

on the in-situ and lab experiments were used as an initial guess for running the numerical

model (MARUN model in Chapter 4).

The average values for capillary parameters were α=12.7 m^{-1}, n=1.66, and

S_r=0.064 based on the capillary retention experiment.

Table 3.3. The Average D_{10}, Laboratory Porosity Measurement, and the Hydraulic
Conductivity (*K*) Estimated By the Kozeny-Carman Equation for Each Well

Well Number	Left transect			Right transect		
	D_{10} (mm)	Porosity (m^3/m^3)	*K* (m/s)	D_{10} (mm)	Porosity (m^3/m^3)	*K* (m/s)
1	1.39	0.311	0.0099	0.74	0.316	0.0029
2	0.79	0.306	0.0030	0.50	0.298	0.0011
3	0.38	0.297	0.0006	0.68	0.308	0.0023
4	0.70	0.310	0.0024	0.76	0.306	0.0028
5	0.60	0.305	0.0017	0.65	0.307	0.0020
6	0.58	0.310	0.0017	0.58	0.302	0.0015
Average	0.74	0.306	0.0026	0.65	0.306	0.0020

The D_{10} and the Porosity values are the average value of D_{10} and porosity of each well.
The hydraulic conductivity (*K*) is not the arithmetic average of *K*-values of different
elevations at each well, but it is calculated by the Kozeny-Carman equation using the data
of the average D_{10} and average porosity.

3.3.2 Water Table

3.3.2.1 Water Table at the Left Transect. Figure 3.6 shows the variations of

the observed water table with time at wells L1, L2, L4, and L6 along the left transect for

the duration of 89 h. During falling tides, the water level at L1 and L2 kept falling at the

same speed as the tide then it abruptly became almost constant (the falling speed was

very low), at an elevation higher than elevation of the pressure transducer. This behavior of the water table variation is an indication of the two layer system from the hydraulic point of view. In this system, beach sediments can be conceptually modeled as two piecewise homogenous layers: a permeable upper layer of coarse, loose material (with the depth of 10 cm to 35 cm) and a much less permeable lower layer with compacted fine material (Li and Boufadel, 2010; Xia et al., 2010; Guo et al., 2010; Bobo et al., 2012). This two layer system can be also confirmed by the results of the in-situ hydraulic conductivity test (discussed in the previous section). The presence of the two layer system was also noted by the change in the material of the pit (smaller sediment size for deeper parts). In addition, digging pits became more difficult after a certain depth. The two layer stratigraphy was further supported by the numerical modeling (discussed in the next chapter).

The water table at L4 and L6 began to diverge from the falling tides once they fell below the beach surface and kept falling with a lower speed than tide. Then, the water level became constant at the same elevation of transducer. It is because that the tide fell below the sensor elevation and the sensor is not able to read the water level data (the transducer was basically recording the atmospheric pressure). It seemed that the two layer system was not formed in these two pits. The field observations during the digging these pits supported this fact as digging was easier in these two pits comparing to that in other pits.

The water table at L6 during the first low tide ($t \approx 15$ h) showed the same behavior of the tide and the sensor could read all part of the water level data. So, it is possible that the water level dropped only a few centimeters below the sensor elevation at other low

tides at this well. When the subsequent flood tide arrived, the water level started rising with tide with a bit delay at these two sensors.

Figure 3.6 also shows that the water tables at L4 and L6 during lower low tides were smaller than that during low tides. This is due to that the water volume in the beach decreases more during lower low tide than during low tide due to desaturation of the beach.
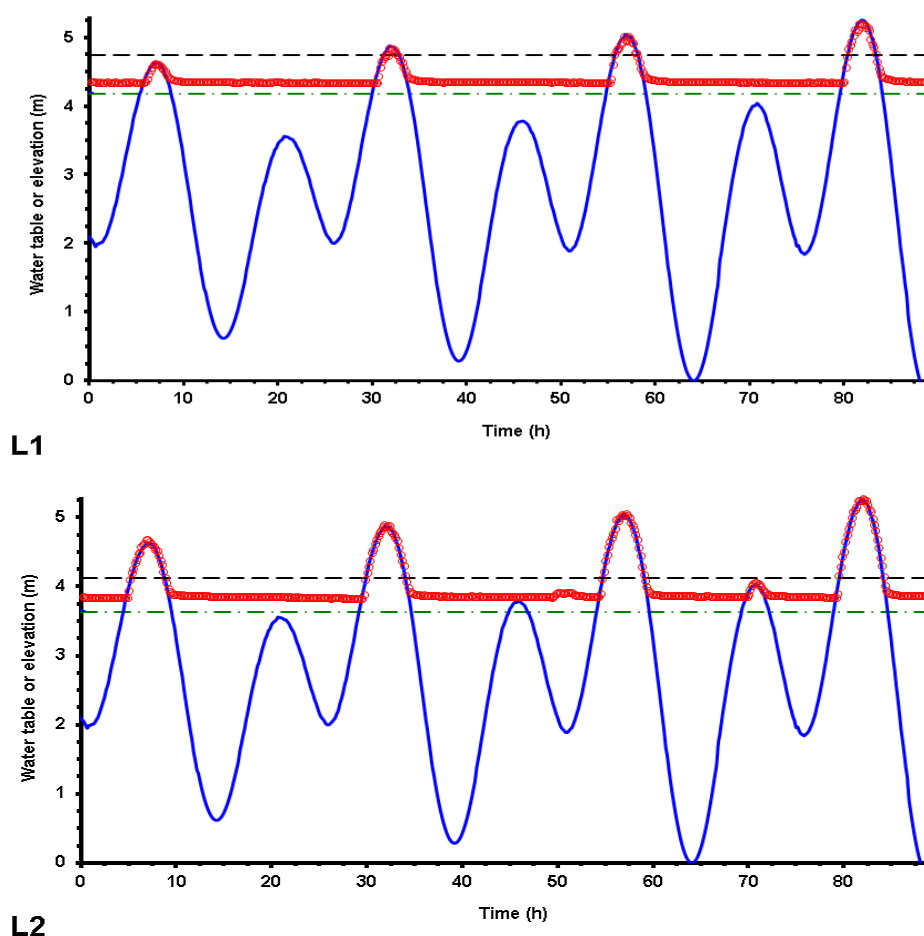
Figure 3.6 Observed water table (circles) at L1, L2, L4, and L6 along the left transect. The tidal level, the beach surface elevation and the elevation of the pressure transducers installed in these observation wells are shown to indicate the submersion period.
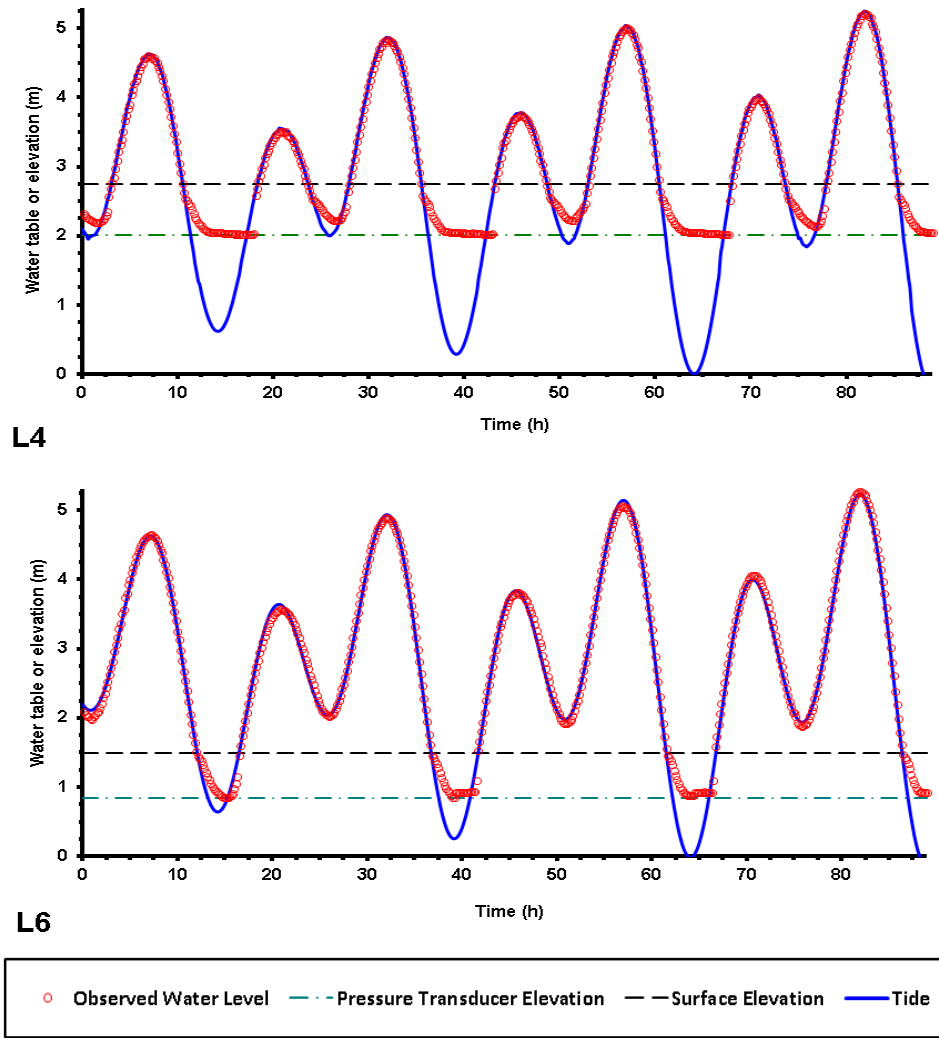
Figure 3.6 Observed water table (circles) at L1, L2, L4, and L6 along the left transect. The tidal level, the beach surface elevation and the elevation of the pressure transducers installed in these observation wells are shown to indicate the submersion period. (Continued)

3.3.2.2 Water Table at the Right Transect. Figure 3.7 reports the observed water table at wells R1, R2, R4, and R6 along the right transect. During falling tides, the water level at R1, R2 and R4 showed the same behavior of the water table at L1 and L2 (Figure 3.6) which indicates the two layer system. The water table at these wells kept falling at

the same speed as the tide then it abruptly became almost constant at a certain elevation higher than the pressure transducer

Water level at R6 showed the same behavior and the water level at this well remained higher than the sensor elevation. But the water level was decreasing slowly with time at this well until the subsequent flood tide reached this well. This decrease in water level can be due to higher permeability of the sediment at R6 or less freshwater recharge.

At the right transect, the water table at all four wells remained above the pressure transducer when the tide level dropped below the transducer elevation. At the left transect the water table at only L1 and L2 stayed at an elevation higher than that of the transducer, though. Moreover, R4 and L4 had almost the same distance to the low tide line and also the transducers in them had the same elevation (Table 3.1). However, the water table was at least 15 cm higher at R4 comparing to L4 during low tides (the water table dropped below the transducer elevation at L4). This is also the case for R6 and L6 which shows that the water table at the middle intertidal zone of the right transect was higher than that of the left transect at low tides. The difference in the beach geomorphology between the two transects or difference in the amount of freshwater recharge could be the reasons for higher water table at the right transect comparing to that in the left transect. This will be investigated in the next section.
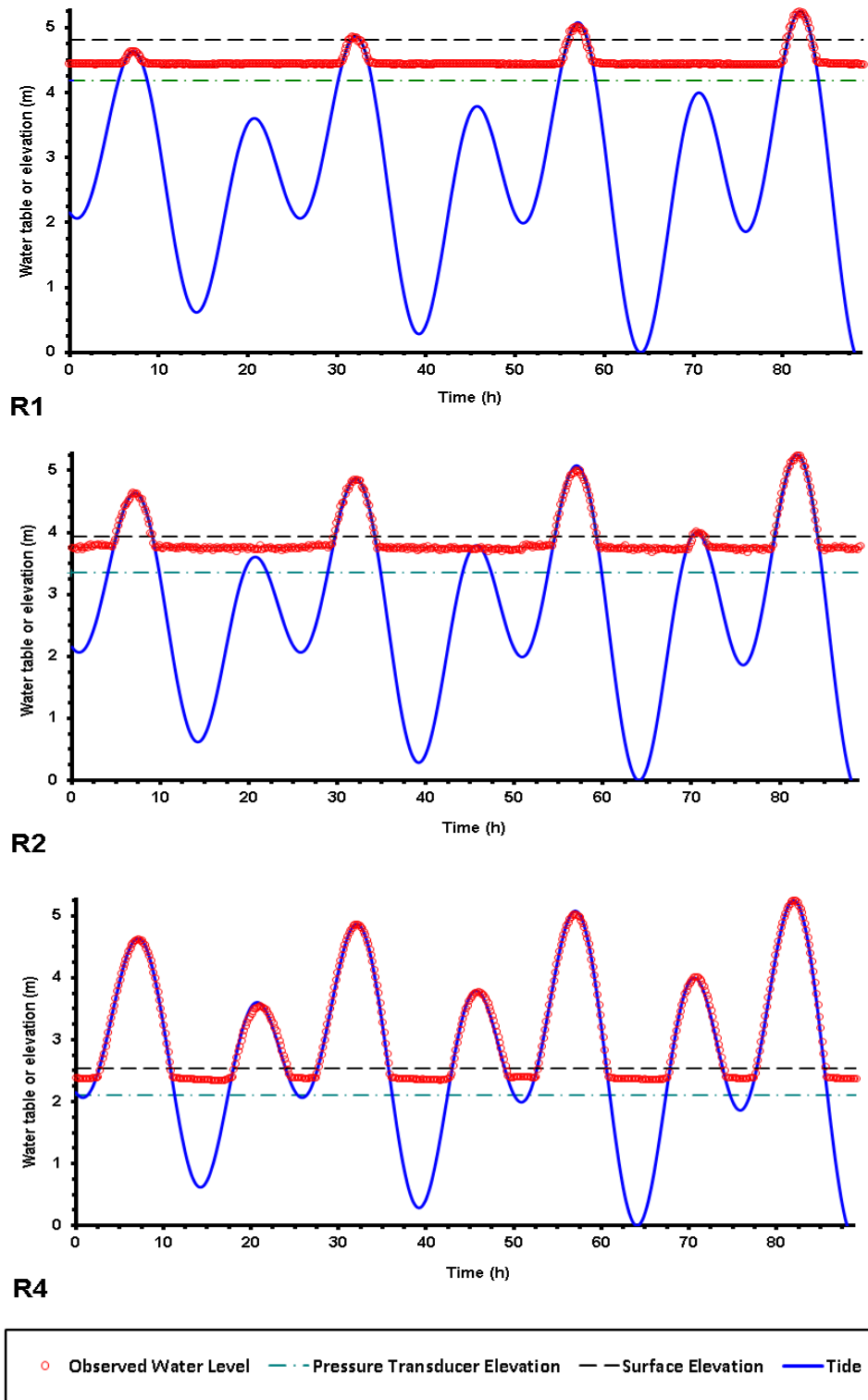
Figure 3.7 Observed water table (circles) at R1, R2, R4, and R6 along the right transect. The tidal level, the beach surface elevation and the elevation of the pressure transducers installed in these observation wells are shown to indicate the submersion period.

R6
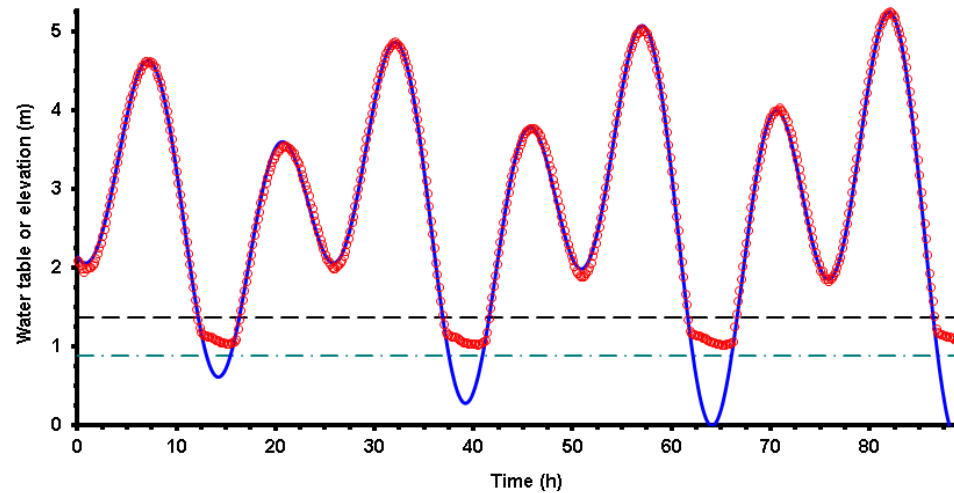
Figure 3.7 Observed water table (circles) at R1, R2, R4, and R6 along the right transect. The tidal level, the beach surface elevation and the elevation of the pressure transducers installed in these observation wells are shown to indicate the submersion period. (Continued)

3.3.3 Salinity

Figure 3.8 presents the variation of observed salinity with time along the left (except L6) and right transects. In this figure, the triangle, the square and the full circle are representing ports A, B and C, respectively. Also, the thick line, the dashed line and the dashed dotted line are tide, surface elevation and the port A elevation (which is 19 cm above the bottom of the pit), respectively. The salinity values are demonstrated from t=49 h (almost two days after starting of water table measurement) until t=90 h. Two seawater samples were collected from the sea adjacent to the beach which resulted in the average seawater salinity of 31 g/L. Results from some of the ports were not available due to clogging.

3.3.3.1 Salinity at the Left Transect. As the port C of L1 and L2 were clogged, only two samples were obtained at ports A and B of these two wells. Before the seawater reached to port A of well L1, the salinity at this port was decreasing from 26 g/L to 21 g/l showing some dilution at this location which could be the result of freshwater flow. When the tide rose close to the surface elevation of L1, the salinity at both ports A and B rose up to 31 g/L, showing that seawater was entering the well from the top. The port B was clogged at the second high tide. Second high tide was a neap tide so the tide could not reach to port A. The salinity at this port was decreasing from 28 g/L to 20 g/L with an exception at t=73 h when the salinity rose again to 28 g/L.

At L2, the salinity at port A was always close to the seawater salinity. But, at port B the salinity was decreasing from 23 g/L to 20 g/L when the tide was falling and rose to 31 g/L when the tide reached the well. At L3, there was still indication of freshwater flow and seawater dilution especially at port B. However, the salinity variation at port B for instance (26-31 g/L), was smaller than the variations at the same port of L1 (20-31 g/L) and L2 (22-31) g/L. This means that the freshwater was diminishing moving seaward. In other wells of this transect (L4 and L5) the salinity at all ports was close to the seawater salinity. One could conclude that, lower salinity at L1, L2 and port B of L3 is an indication of freshwater flow from L1 to L3.

3.3.3.2 Salinity at the Right Transect. Figure 3.8 also reports the observed salinity values at the six wells of the right transect. The port C of R1 was clogged. Consequently, the results of ports A and B are presented. The observed salinity at ports A and B of well R1 fluctuated with the tidal level, dramatically. At low tides, the salinity values were small close to 1 g/L. But as soon as tide reached to the ports, the salinity

rose abruptly and reached to 20 g/L. However, this value was almost 10 g/L lower than the seawater salinity. At R2, salinity of ports A, B and C were ranging from 10-28 g/L, 5-30 g/L and 1-31 g/L, respectively. At this well, the deepest port (port A) had the highest salinity and its minimum value was 10 g/L. The pore water salinity of port B was equal to 30 g/L at t=71 h (high tide) and it started decreasing with the tide falling. The salinity at this port became eventually equal to 14 g/L at t=77 h (almost low tide). Port C, which was located in the surface layer, showed the same behavior of ports A and B of W1. The salinity at this port was almost equal to zero at low tide and it became equal to seawater salinity at high tide. At W3, the salinity of port C was ranging from 23-31 g/L and it was smaller than the values of port B. The salinity at this well does not follow a specific pattern. Note that this well was located 4 m seaward of the tracer injection manifold and the increase of the salinity value around t=50 h was probably because of tracer arrival at R3 at this time. At R4, salinity of ports A, B and C were ranging from 17-27 g/L, 17-29 g/L and 16-31 g/L, respectively. The tracer arrived at R4 around t=50.2 h. As the result, the salinity increases in all ports. It is interesting that the increase of salinity at R4 because of the tracer injection happened shortly after the salinity increase at R3 noting that R4 was 5 m seaward of R3. This indicates the fast travel time for the tracer probably due to the high freshwater recharge and/or high hydraulic conductivity of the upper layer (refer to next section for more information). Surprisingly, the average salinity at R4 was smaller than that of at R3. This means that there was higher amount of freshwater at this well comparing to the R3, even if the R3 was closer to the pond. One reason for that could be the existence of different flow path due to the heterogeneity of the beach.

At low tide, the salinity at port B of R5 was around 18 g/L and when the tide reached to this port, the salinity rose to 31 g/L. The salinity at port A was also ranging from 24-30 g/L. The salinity at port C was around 31 g/L for most of the times except when the tide fell below the beach surface at R5 (t≈76 h). At this time, salinity dropped to 27 g/L. There were only two readings at port A of R6. The average of salinity at this port was 10 g/L, showing the existence of freshwater even in this well.

Based on Figure 3.8 whenever tide dropped the surface elevation at each well of the right transect, the salinity dropped rapidly as well (especially at more landward wells). This shows the high quantity of freshwater recharge from inland which could travel relatively fast in the upper layer (with high permeability) in the right transect. This was also noted in the field while digging the pits as the freshwater seepages were observed on the walls of the new dug pits. However, the salinity only dropped at L1 for 5 g/L during the low tide. The salinity was modeled numerically and the results are presented in Chapter 4.
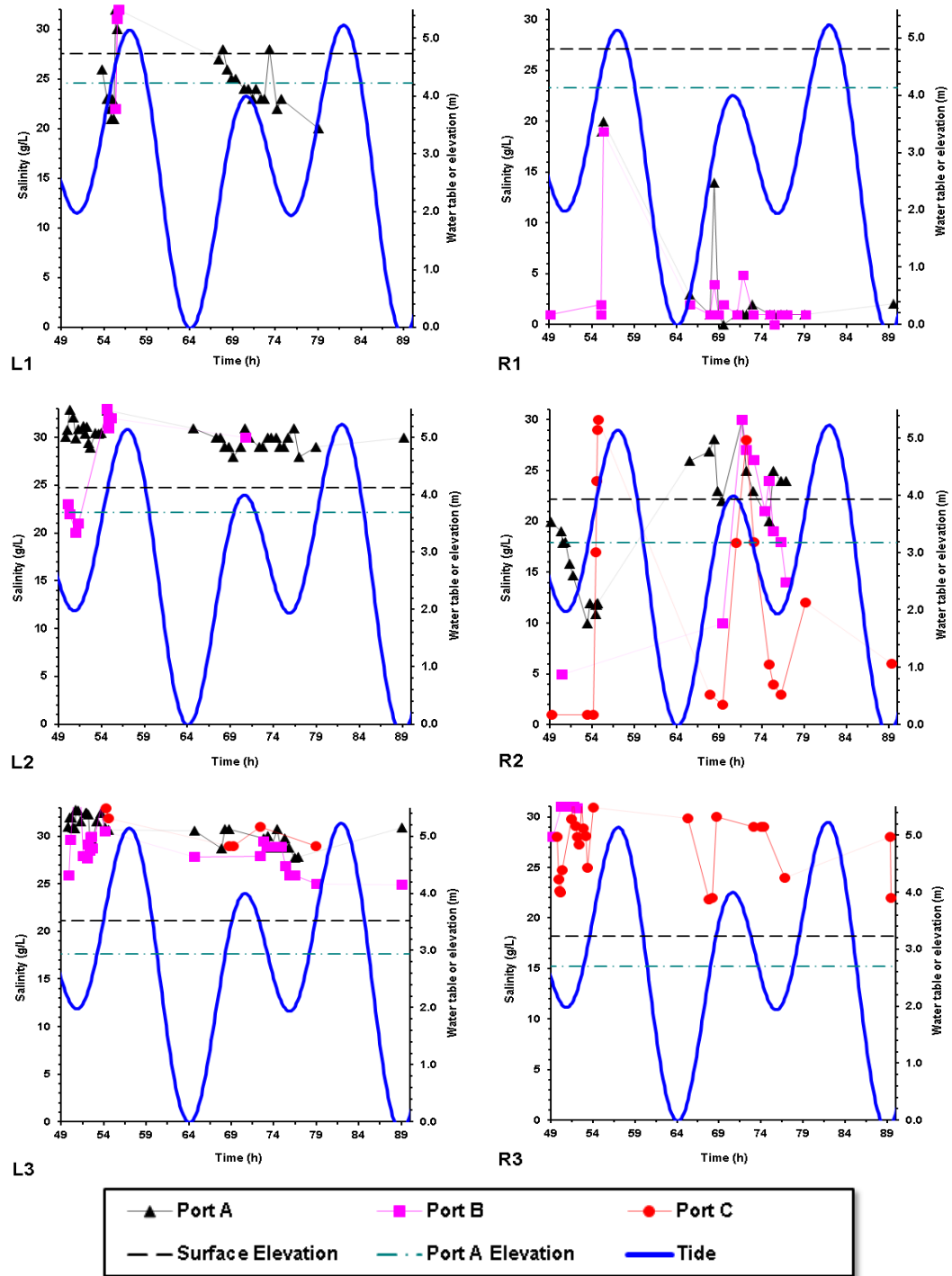
Figure 3.8. Observed salinity at ports of all wells (except L6) along the left and right transects. The tidal level, the beach surface elevation and the elevation of the port A at these observation wells are also shown.
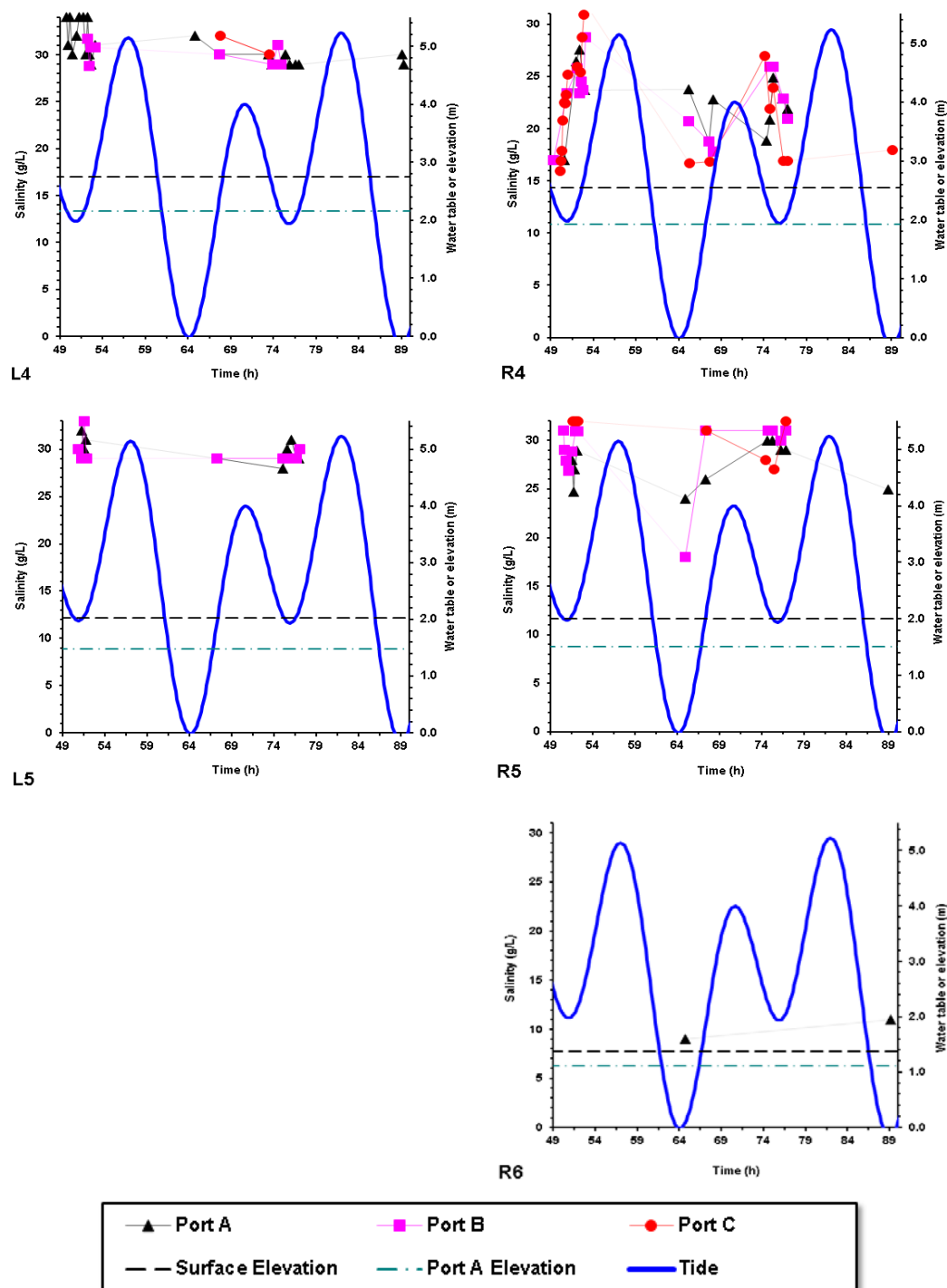
Figure 3.8 Observed salinity at ports of all wells (except L6) along the left and right transects. The tidal level, the beach surface elevation and the elevation of the port A at these observation wells are also shown. (Continued)

3.3.4 Lithium Concentration

Figure 3.9 shows the observed lithium concentration of the pore water at different ports of the wells in the two transects except at R6 and L6. No sample was collected from L6 and only two samples at R6 were collected (with the values of 0.6 mg/L and 2.0 mg/L). The shaded columns in the figures show the tracer application period. The tracer application lasted 2 hours and 4 minutes. The lithium concentration in the tank was 355 mg/L.

The maximum lithium concentration at L1 was detected in port A, 6 hours after the application was over. Except the first value which was equal to 8 mg/L, other values were less than 3 mg/L. The maximum lithium concentration at port A of R1 was 3 mg/L (t=68.8 h) and it was 13 mg/L for port B (t=71.8 h).

The lithium concentration at port A of L2 was very high during the application period with a maximum concentration of 325 mg/L. After application was stopped, the lithium concentration started decreasing and was equal to 16 mg/L at t=54.8 h. This is an indication of landward movement of the plume in the left transect. Lithium concentration at port B of this well was close to zero for the whole time. It was probably due to the shallow depth of port B (only 10 cm deeper than beach surface) and the plume that spread landward did not fill the pore space to rise to it. In addition, based on Figure 3.8 the salinity at port B decreased from 23 g/L to 20 g/L during tracer application. However, the salinity at port A remained equal to 31 g/L. This indicates that brackish water propagated seaward through port B and it was floating above the high density seawater at port A.

The lithium concentrations at ports A and B of R2 didn't rise significantly during the application period and their maximum value was only 3 mg/L, showing much less landward movement of the plume in the right transect in comparison with the left transect. The reason for that could be the higher freshwater recharge to the right transect in comparing to the left transect. At the second high tide, the lithium concentration at port A of R2 rose again with the maximum concentration of 9 mg/L. The maximum lithium concentration among the three ports was observed in port C with the maximum value of 13 mg/L at t=70.8 h.

The lithium concentrations at L3 for both ports A and B, were initially zero then reached maxima of 70 and 365 mg/L, respectively. The peak of the concentration occurred almost 1 hour after the end of application (t=52.4 h). Also, the plume occupied the shallow port (port B) first. The lithium concentration at port C of L3 was the smallest. This indicates that the plume traversed mostly through port B, with a sharp concentration gradient. When seawater arrived at L3 (t≈63.8 h) the lithium concentration dropped sharply. The maximum lithium concentration at L3 was close to the lithium concentration in the tank. It shows that the plume wasn't washed out by freshwater before reaching L3.

R3 was four meters seaward of the application manifold. The lithium concentration at port C of this well started rising 40 minutes after the application was started (t=50.1 h) and reached its maximum (230 mg/L) at t=50.5 h. After the application was stopped, the lithium concentration at port C was higher than 200 mg/L for four hours. Then, when the tide reached this port, the lithium concentration dropped sharply to 16 mg/L. The lithium concentration at port B was at the background value during the

application and had its maximum (17.6 mg/L) at t=52.2 h, one hour after the application was stopped. The lithium concentration rose much faster at R2 comparing to L2. However, the maximum value of lithium concentration at R3 (230 mg/L) was smaller than the maximum value at L3 (350 mg/L). This could be again due to larger amount of freshwater recharge to the right transect which could cause the tracer to travel faster in longer distance but to get more diluted.

At L4, 30 minutes after the application was finished, the lithium concentration reached its maximum values of 19 and 30 mg/L at ports A and B, respectively. The lithium concentration at R4 followed the same behavior as R3. It started rising 55 minutes after the application was initiated and reached its maximum at t=52.2 h. The maximum value for both ports B and C was 220 mg/L, which was almost 10 times larger than the lithium concentration at L4. When the tide reached these ports, the lithium concentration dropped to 50 mg/L.

The lithium concentrations remained at the background level at L5 for all of the samples. Oppositely, the lithium concentration at port A of R5 started rising 80 minutes after the start of application and reached its maximum at t=51.8 h. The maximum lithium concentrations for ports A and B were 30 mg/L and 16 mg/L, respectively.

Comparing the tracer study results between the right and left transects, one could say that the average lithium concentration at the right transect was smaller than the lithium concentration at the left, indicating that the tracer was diluted in the clean transect. Also, tracer could travel longer before it was completely diluted at the right transect.
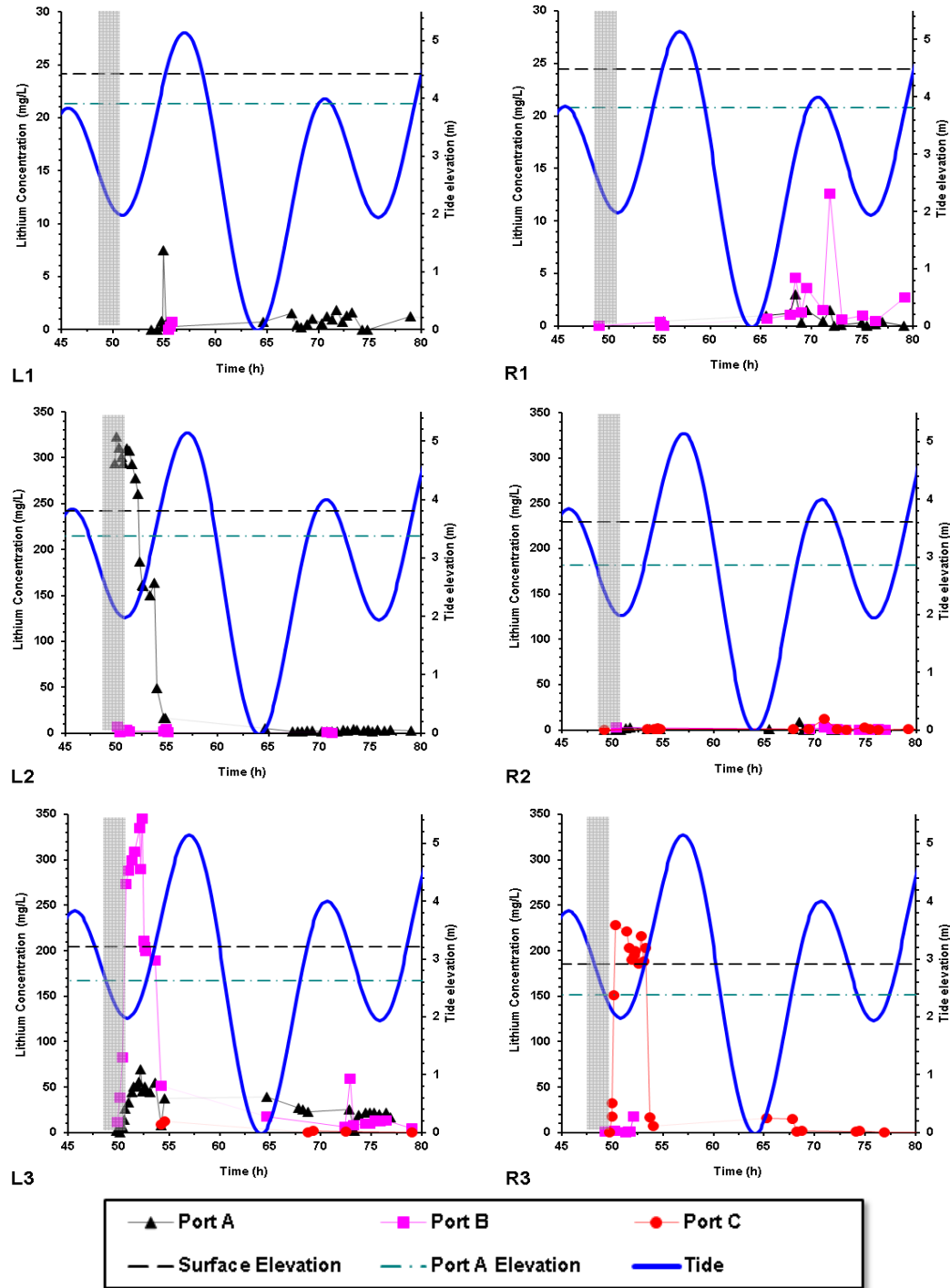
Figure 3.9. Observed lithium concentration of the pore water at ports of all wells along the left and the right transects (except L6 and R6). The application was started at *t*=49 h and was stopped after 2 hours and 4 minutes. The applied concentration of lithium was 355 mg/L. The injection period is indicated using the shaded column in this figure. The tidal level, the elevation of the beach surface and the elevation of port A at these observation wells are also shown.

Figure 3.9 Observed lithium concentration of the pore water at ports of all wells along the left and the right transects (except L6 and R6). The application was started at $t=49$ h and was stopped after 2 hours and 4 minutes. The applied concentration of lithium was 355 mg/L. The injection period is indicated using the shaded column in this figure. The tidal level, the elevation of the beach surface and the elevation of port A at these observation wells are also shown. (Continued)

3.3.5 Tracer Plume Movements

An integral means to quantify the overall motion of the plume is tracking the variation of

its centroid with time. The centroid or the center of mass is the mean location of all mass

in the system. The center of mass of a system of particles is defined as the average of

their positions weighted by their masses. Using the available ports, the coordinates of the centroid of the plume were estimated by:

$$X_G = \frac{\sum\limits_{i=1}^{np} x_i \; c_i}{\sum\limits_{i=1}^{np} c_i} \tag{3.4}$$

$$Z_G = \frac{\sum\limits_{i=1}^{np} z_i \; c_i}{\sum\limits_{i=1}^{np} c_i} \tag{3.5}$$

where x and z are the horizontal and vertical coordinates of the port where the concentration c_i is measured, np is the total number of ports used to compute the moments. In order to provide sufficient points for the evaluation of the centroid coordinates, the concentration data were interpolated linearly with time. The results are reported in Figure 3.10a and Figure 3.10b for the centroid of the left and right plumes, respectively. The centroid at five different times after the beginning of the tracer application (t=49.2 h) was marked with the filled squares in these figures.

Based on Figure 3.10a, the centroid of the plume at the left transect (oiled transect) at t=50.08 h (1 hour after tracer application was started) was below the application manifold. The centroid of the plume traveled 8 m seaward of the application manifold in 26 hours.

Figure 3.10b indicates that one hour after the start of the application (at t=50.08 h), the centroid of the plume travelled 6 m seaward of the application manifold at the

right transect. For the rest of times, the centroid was travelling between R3 and R4 with the total travel distance of 6 meters and the average depth of 0.25 meter. The fact that the center of plume travelled more seaward in the right transect comparing to the left transect, is probably due to higher freshwater recharge in the right transect which can carry the tracer with itself.

Michel et al. (2009) studied several beaches in Prince William Sound. Based on their observations there was no subsurface oil lingering in the beaches like Knight Island, Perry Island, and Evans Island, particularly where a small pond occurred behind the storm berm, but also where topography allows groundwater to be discharged through the beach. Therefore the joint action of higher freshwater recharge to the right transect, larger beach slope in the right transect (11 % in comparison with 9 % in the left transect) and also difference in the depth of bedrock could be the reasons for disappearance of the oil from the right transect.

In terms of the bulk of the plume delineated by the 10% value (i.e., 36 mg/L), the tracer migrating with the tide reached a concentration of 10% of the maximum at 1.12 h and 1.0 h at Port B of L3 and Port C of R3, respectively (Figure 3.9). Based on these values the travel speeds for the left and right transects were almost 4.64 m/h (5.2 m/1.12 h) and 4.75 m/h (4.75 m/ 1.0 h), respectively. These results indicate that the tracer is moving relatively fast and with the same speed at both transects which is confirmed by the relatively equal hydraulic conductivity of sediments in two transects as discussed earlier.
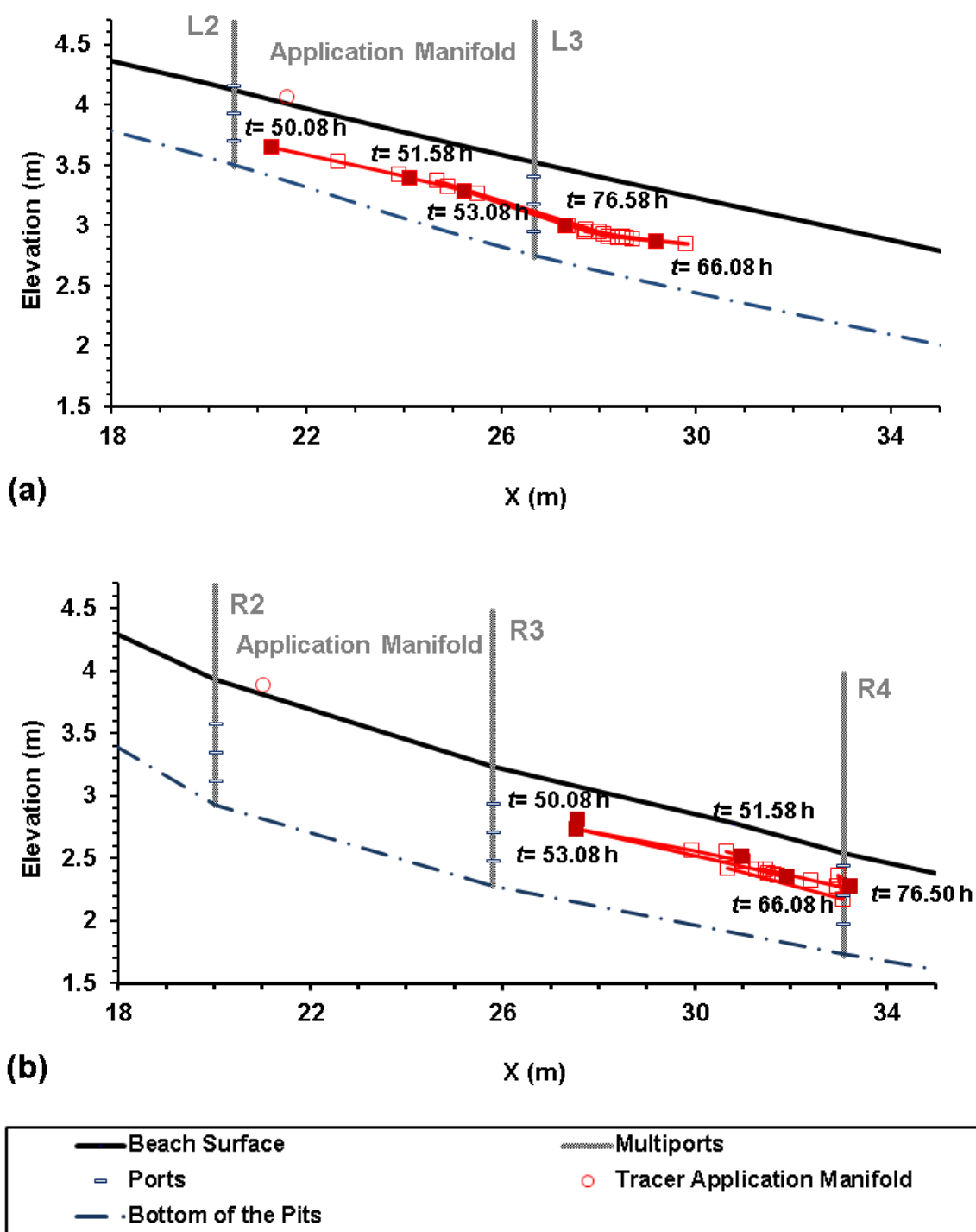
Figure 3.10 Movements of the tracer plume centroid for (a) the left (oiled) transect and (b) the right (clean) transect. The dashed-dotted line connects the bottom of the pits.

3.4   Conclusion

The beach hydrodynamic factors were investigated through the field measurements of water table, salinity and tracer (lithium) concentration in a tidal gravel beach in PWS. This beach was polluted by the Exxon Valdez oil spill in 1989 and the oil was observed at the left side of the beach.

The observed water level results, the in-situ and lab sediment analyses and the field observations indicated the presence of a two-layer structure in the beach. This system is characterized by a high permeability layer over a much lower permeability layer. This two-layer system was also reported in the recent studies of gravel beaches in PWS (Li and Boufadel, 2010; Xia et al., 2010; Guo et al., 2010; Bobo et al., 2012). The two-layer system could promote oil persistence:

The observed salinity and the tracer study suggested higher freshwater recharge to the right transect in comparison to the left transect. The bedrock in the right transect seemed to be deeper than that in the left transect. This means that the freshwater could be discharged to the sea easier in the right transect. Freshwater recharge from the land promotes the removal of oil by sustaining a high water table in the beach during low tides and subsequently preventing the oil from dropping into the lower layer. Also, high seaward flow could cause the dislodgement of oil and its washout to sea.

If the tracer is taken as nutrients, the tracer study implies that the bioremediation via nutrient application on the beach surface should be conducted very cautiously, one need to determine appropriate application location(s) to prevent the nutrient solution from washing into the sea during application before it reached to all oiled locations. However, the results showed that the tracer was transporting closer to the application manifold at

the left (oiled) transect comparing to the right transect. If one chooses the oiled locations accurately, it is highly possible that the nutrient application at the surface can be successful at this beach and chemicals can get to the oily locations in order to stimulate the bioremediation.

Moreover, the tracer traveled shorter at the left transect and also there was a large landward movement in this transect. These factors can be an indication of oil in the gravel beaches of Prince William Sound.

CHAPTER 4

NUMERICAL INVESTIGATION OF WATER FLOW AND SOLUTE TRANSPORT IN A GRAVEL BEACH POLLUTED BY THE EXXON VALDEZ OIL

4.1 General

The right side of the gravel beach studied in summer of 2008 was clean while the oil was found at the left side of the beach (100 m away from the right side). There was a freshwater pond behind the beach close to the right transect. The results in Chapter 3 revealed that higher freshwater was recharging to the beach at the right transect. In this chapter and the next chapter, the focus is to numerically simulate the right transect using the MARUN model in order to understand the beach hydrodynamic factors and to relate these factors to the disappearance of the oil from the right transect. The MARUN model was used to reproduce the observed data of water table and pore water salinity (the tracer data was not modeled).

The governing equations of the MARUN model were explained in Chapter 2. The MARUN model was introduced by Boufadel et al. (1999a). The model was verified and validated and has been extensively used to simulate water flow and solute transport in beach environment (e.g., Abdollahi-Nasab et al., 2010; Boufadel, 2000, Boufadel et al., 2011; Guo et al., 2010; Li et al., 2007; Li et al., 2008; Li and Boufadel, 2010; Li and Boufadel, 2011; Naba et al., 2002; Xia et al., 2010).

4.2   Modeling Implementation

The simulation domain of the right transect across the shoreline is presented in Figure 4.1 which was extended from the pond to the sea. The simulated beach was 95 m long and 3 m deep. The average slope at this transect in the intertidal zone was 11%. The observed water level and salinity at the pond were used as the left boundary condition. During the field study, the pond water level was 6.5 m and the salinity was measured as almost 0 g/L. The boundary condition at the intertidal and subtidal zones was determined by the tide. For the submerged part of the beach, the water pressure was seawater column above the beach surface, as $\psi = \beta_{tide}\left[H_{tide}(t) - z\right]$, where β_{sea} is the density ratio of seawater to freshwater (equation (2.2)), $H_{tide}(t)$ is the tide level (equation (3.1)), and z is the elevation. The "outflowing" boundary condition was applied for salinity for the submerged part (refer to the works of Galeati et al., 1992; Boufadel et al., 1999a; Park and Aral, 2008). Based on this method, when the seawater was entering the beach (i.e., rising tide), the salt concentration at the boundary was equal to the seawater concentration (31 g/L). When the groundwater was discharging to the sea (i.e., falling tide), the zero dispersive flux for the salinity was applied. Along the domain bottom and unsaturated zone boundaries, which include the upper part of the landward boundary and the beach surface above tidal level, a zero-flow and zero-mass transport boundary conditions were used

In order to define the initial condition for the salinity distribution in the model, it was assumed that the beach was filled with freshwater and the interface of the seawater and freshwater was located between mid-tide and low-tide zones. Then, the simulations were conducted for few spring-neap tidal cycles until additional runs couldn't improve

the water table and salinity simulation results further (and movement of the interface became negligible).

It was mentioned in Chapter 3 that after installing the multiports and PVC pipes, the pits were backfilled using the excavated materials. The field sampling started almost two days after filling the pits. As a result, the time was not enough for materials in the pits to get compacted by tidal action. Consequently, the pits should be treated differently with the intact part of the beach and different sediment properties (like hydraulic conductivity) should be assigned to them. This "pit effect" was considered in the model (by assigning the same hydraulic conductivity of the upper layer to the materials of the pit).
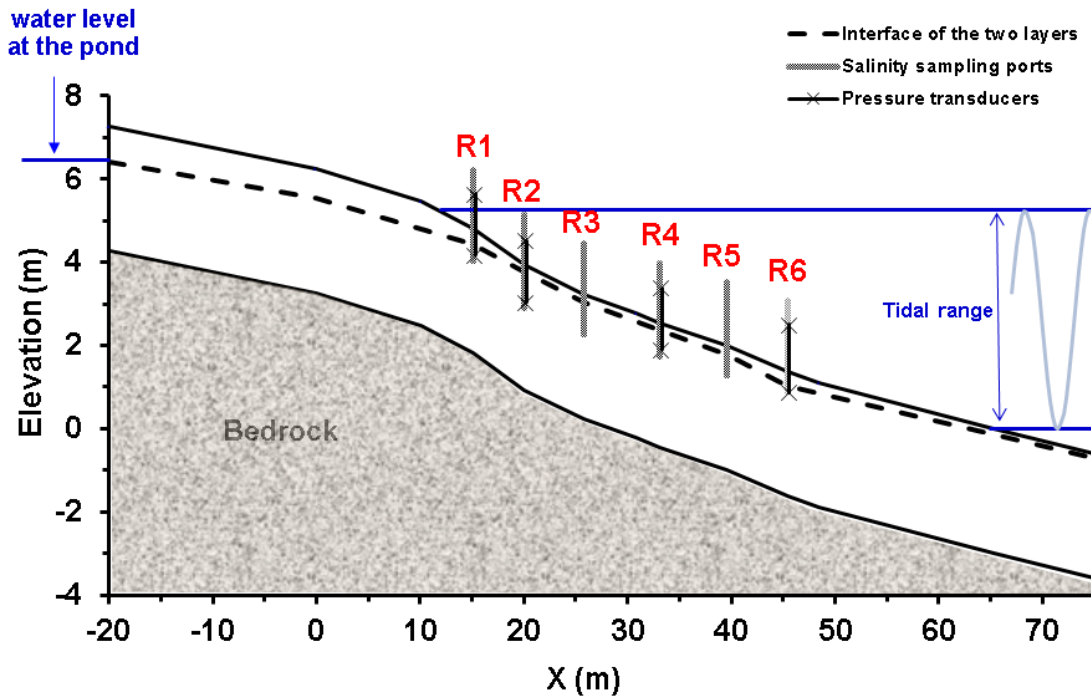
Figure 4.1 Schematic cross-section of the right transect as the simulation domain. The thickness of the aquifer was 3 m. Well locations (multiports/PVC pipes), high tide line and water level at the pond (landward boundary condition) are shown here. The tidal range was around 5.2 m. The pits are not shown in this figure.

Numerical Implementation

In order to discretize the beach domain, different combinations for number of nodes in horizontal and vertical directions were tested. More simulation time was needed for higher number of nodes. The final values for the mesh size were selected so that the requirements for accuracy of the results and simulation speed were both fulfilled. For model calibration, the domain was discretized using 21 and 442 nodes in vertical and horizontal directions, respectively. This resulted in 9,982 nodes and 17,640 triangular elements. The Courant number is defined as $C_r = v\,\Delta t\,/\,\Delta l$, where "v" is the Darcy velocity, Δt is the maximum time step and Δl is the maximum mesh size. In the simulations, the time step was variable but it was selected in a way to ensure that the Courant number was less than 0.95 for numerical stability. The mesh spacing was selected in a way to keep the grid Peclet number equal or less that 2.0 (Zheng and Bennett, 2002). More documentation regarding the MARUN model is presented in Appendix A.

No seepage face was observed during the study. Therefore, the seepage face subroutine in MARUN (Naba et al., 2002) was disabled. Similar implementations were considered in the work of Li et al. (2010), Guo et al. (2010) and Xia et al. (2010) who studied the beach hydrodynamics in gravel beaches of PWS, Alaska.

4.3   Model Calibration\Validation

It was intended to fit the simulation results of both water table and pore water salinity to the observed data while keeping the model as simple as possible. The sediment properties such as capillary parameters, hydraulic conductivity and porosity were

estimated (Table 4.1) by analyzing the samples obtained in the field (Chapter 3) or by conducting the in-situ tests. These values were used as the initial estimates to run the simulations. Although the observed results (water table and in-situ hydraulic conductivity test) suggested that the beach can be viewed to be consisted of two layers with very different hydraulic conductivities (Chapter 3), the beach was considered as homogenous (i.e., one layer, the approach which is used to numerically simulate sandy beaches) at the first try. Different values (a range from 1×10^{-4} m/s to 5×10^{-2} m/s) were selected for the hydraulic conductivity of this one-layer beach but none of those cases could explain the water table behavior in the pits (Figure 3.7). The simulation result of one of the homogenous cases is presented in the next section.

Table 4.1 Values of the Model Parameters used in Numerical Simulation (of the Control Case)

Parameter	Definition	Unit	Value
ϕ	Porosity	-	0.31
K_0	Saturated hydraulic conductivity for freshwater	m/s	5×10^{-2} and 7×10^{-3} (surface layer) 10^{-5} (lower layer)
α	Capillary fringe parameter of the van Genuchten (1980) model	1/m	40.0
n	Sand grain size distribution parameter of the van Genuchten (1980) model	-	7
S_r	Residual soil saturation.	-	0.01
S_0	Specific storativity	m	10^{-5}
ε	Fitting parameter of density-concentration relationship	m^3/kg	7.63×10^{-4}
α_L	Longitudinal dispersivity	m	0.1
α_T	Transverse dispersivity.	m	0.01
τD_m	Product of tortuosity and diffusion coefficient	m^2/s	10^{-9}

In the next step, the two-layer approach was used to model the beach. For the upper layer in the intertidal zone, the average hydraulic conductivity value (2×10^{-3} m/s, Chapter 3) estimated based on the Kozeny-Carman equation (Carrier, 2003) was used as the initial guess. The domain was extended to the pond at the left boundary. Based on field observations, the sediments in the area close to the pond at the surface were consisted of a mixture of fine gravel and organic soil. This suggests that hydraulic conductivity of the upper layer in the supratidal zone should be lower than that in the intertidal zone. Therefore, two values were selected for the hydraulic conductivity; a smaller value for Zone 1 (-20 m < x < 0 m) and a larger value for Zone 2 (0 m < x < 75 m). The pond was located at x= -20 m (Figure 4.1). For the lower layer, the average results of the in-situ test at the depths of 0.65 m and 0.70 m (1×10^{-6} m/s) were chosen as the initial estimate.

Model was calibrated based upon the observed data and the values of the saturated hydraulic conductivities for the two layers and for Zone 1 and Zone 2 were determined. For the lower layer, the hydraulic conductivity was found to be around 10^{-5} m/s. The hydraulic conductivity for the upper layer was around 7×10^{-2} m/s for Zone 1 (-20 m < x < 0 m), and around 5×10^{-2} m/s for Zone 2 (0 m < x < 75 m). The initial estimates for the hydraulic conductivity were only one order of magnitude different with the calibrated values. Field observations were used to estimate the thickness of the upper layer (by measuring the depth below which the sediments in the walls of the pits looked more compacted). However, the model calibration based on the water table simulations was the main method to find the thickness of the upper layer.

The measured capillary parameters in the lab were used in the model and were updated by model calibration. It should be noted that the lower layer in the intertidal zone always remained submerged and as a result, the capillary parameters were not applicable to this layer. The longitudinal and transverse dispersivities (equation (2.9)) were selected based on the model calibration. The model parameters and their values are listed in Table 4.1.

Figure 4.2 compares the observed water table with the simulated results. This figure shows that the numerical model can reproduce the observed data very well and except R6, the difference between the observed water table and simulated results was only 2 cm. The numerical model could predict the overall behavior of the water table at R6, as well. The observed water table at R6 diverged from the falling tide when the tide fell below the beach surface. This behavior could be due to local variation in the hydraulic conductivity around R6. Based on the simulations, if the hydraulic conductivity of the sediments in the pit at R6 (and of the sediments around R6) is decreased, the agreement between the observed and simulated water table will improve at R6. However, in order to keep the model simple and more general, the hydraulic conductivity of the materials in the pit at R6 was kept equal to that in other pits (the hydraulic conductivity of the pits was equal to that of surface layer because of the pit effect discussed above).
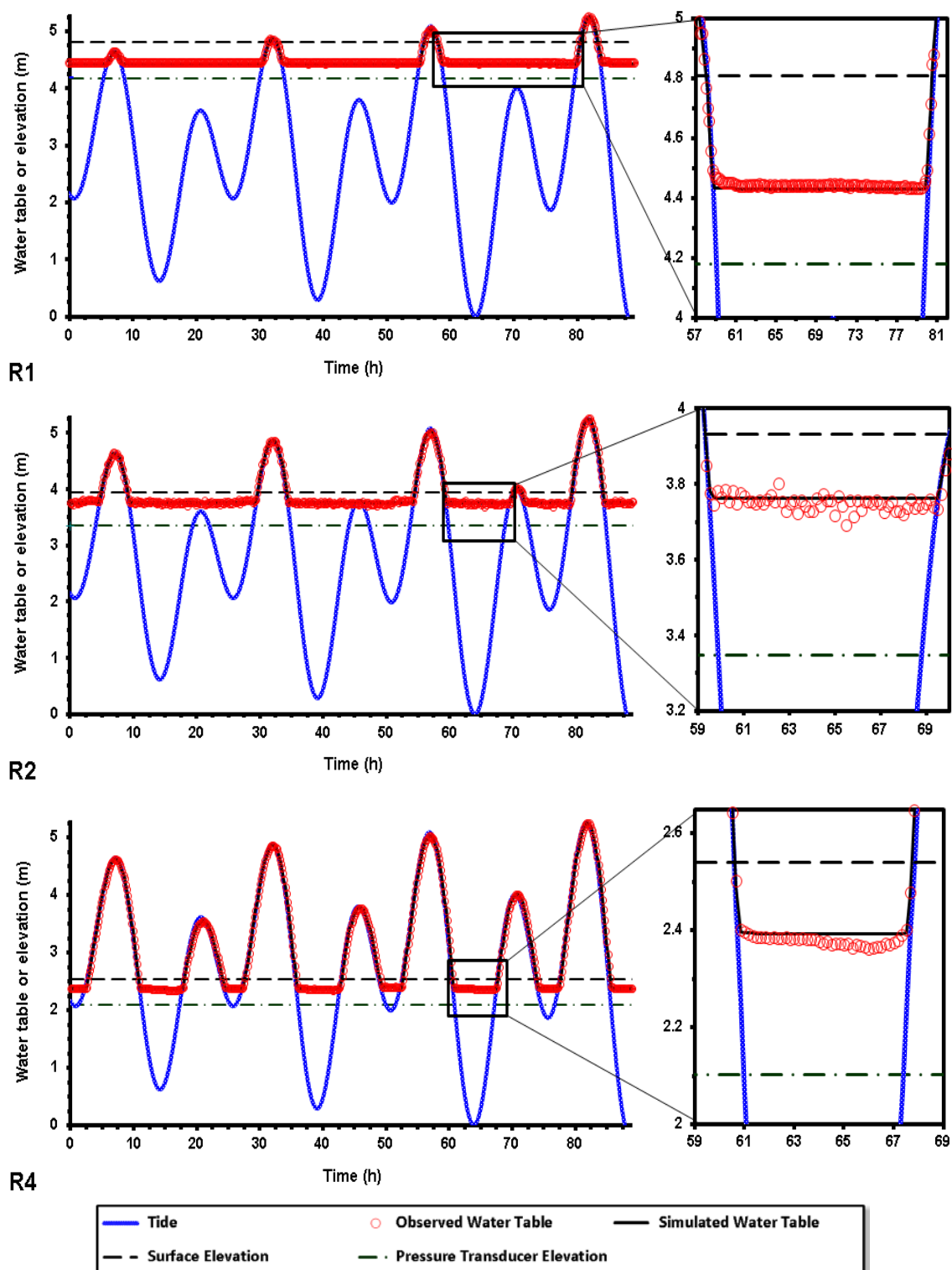
Figure 4.2 Comparison of the observed (circles) and simulated water table (black solid lines). The tidal level, the beach surface elevation and the elevation of the pressure transducers installed in these observation wells are shown.
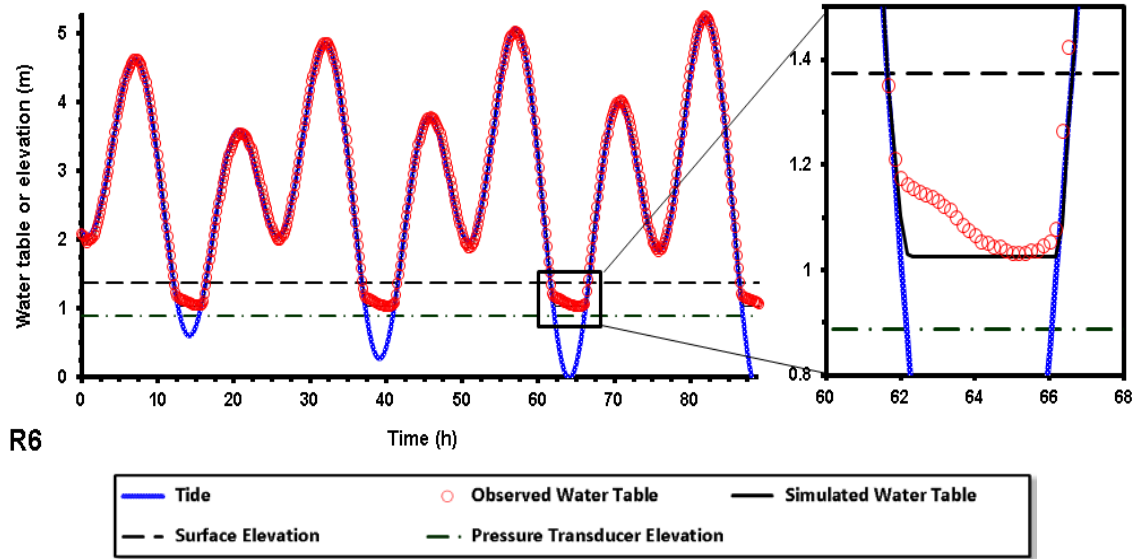
Figure 4.2 Comparison of the observed (circles) and simulated water table (black solid lines). The tidal level, the beach surface elevation and the elevation of the pressure transducers installed in these observation wells are shown. (Continued)

Figure 4.3 reports the observed and simulated salinities at the wells of the right transect. There was a high degree of uncertainty in the beach characteristics (such as sediment heterogeneity). However, Figure 4.3 shows that there was a good agreement between observations and simulation results. The observed salinity at ports R5B and R6A was smaller than the simulated one. This could be due to the local heterogeneity at these locations.
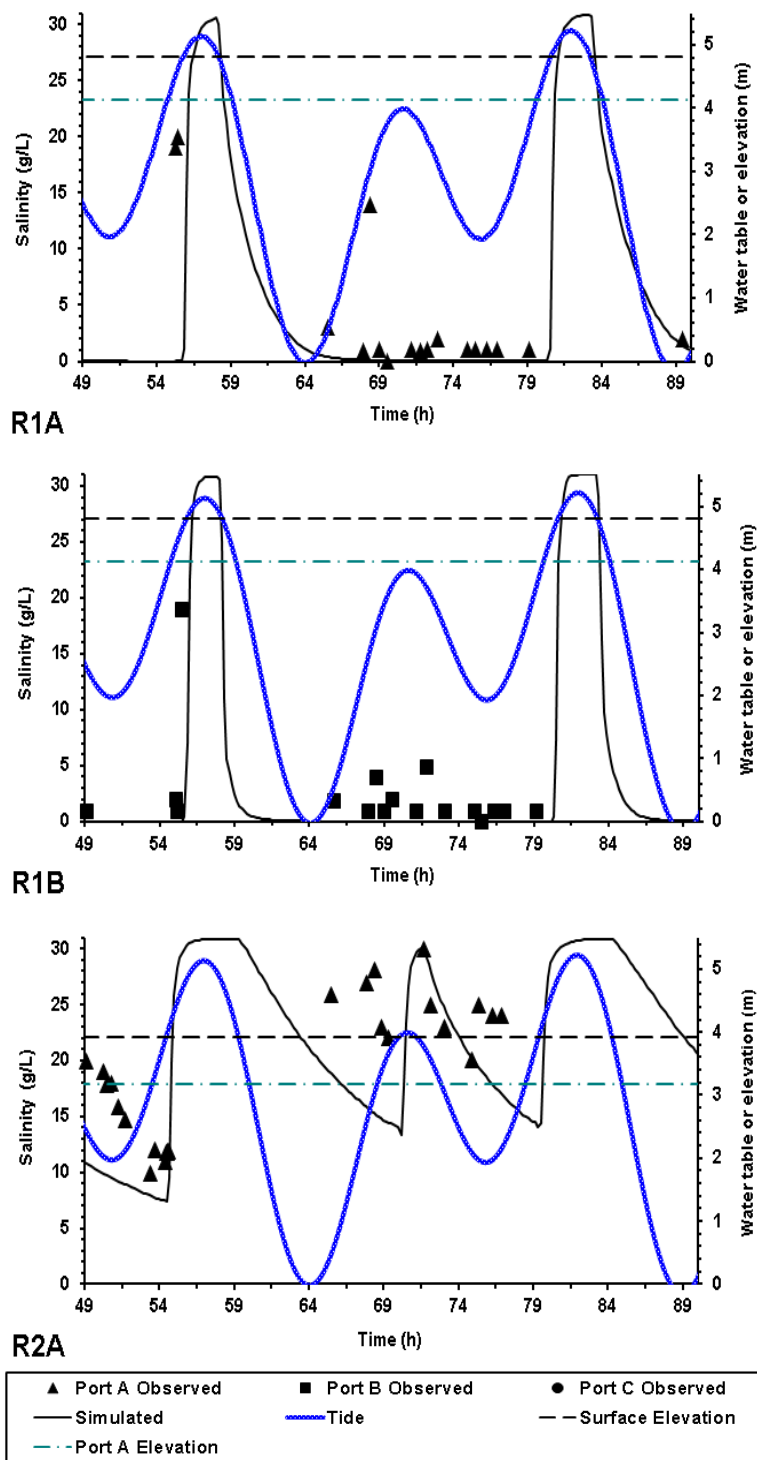
Figure 4.3 Comparison of the observed (symbols) and simulated (thick lines) salinities of the pore water at ports of all wells along the right transect. The tidal level, the beach surface elevation and the elevation of port A in these observation wells are shown.

Figure 4.3 Comparison of the observed (symbols) and simulated (thick lines) salinities of the pore water at ports of all wells along the right transect. The tidal level, the beach surface elevation and the elevation of port A in these observation wells are shown. (Continued)

Figure 4.3 Comparison of the observed (symbols) and simulated (thick lines) salinities of the pore water at ports of all wells along the right transect. The tidal level, the beach surface elevation and the elevation of port A in these observation wells are shown. (Continued)

Figure 4.3 Comparison of the observed (symbols) and simulated (thick lines) salinities of the pore water at ports of all wells along the right transect. The tidal level, the beach surface elevation and the elevation of port A in these observation wells are shown. (Continued)

Figure 4.3 Comparison of the observed (symbols) and simulated (thick lines) salinities of the pore water at ports of all wells along the right transect. The tidal level, the beach surface elevation and the elevation of port A in these observation wells are shown. (Continued)

4.4 Sensitivity Analysis

In order to evaluate the effect of beach hydraulic conductivity, the hydraulic conductivity of the pits and dispersion coefficients on the results, seven cases were designed for sensitivity analysis. Table 4.2 reports a summary of the parameters that were used for each case. The results of each case were compared with the simulation results of the control case with the parameters listed in Table 4.1. Guo et al. (2010) conducted similar analyses. For the sake of brevity, only the results at selected wells (and ports) are presented.

Table 4.2 The Parameters used in Simulating the Eight Cases

Case No.	Hydraulic Conductivity (m/s)				Longitudinal Dispersivity (m)	Transverse Dispersivity (m)
	Upper (surface) Layer		Lower Layer	Pits		
	Zone 1[*]	Zone 2[*]				
1 (Control Case)	7×10^{-3}	5×10^{-2}	10^{-5}	5×10^{-2}	0.1	0.01
2	7.5×10^{-3}	7.5×10^{-3}	7.5×10^{-3}	7.5×10^{-3}	0.1	0.01
3	7×10^{-3}	5×10^{-2}	10^{-4}	5×10^{-2}	0.1	0.01
4	7×10^{-3}	5×10^{-2}	10^{-6}	5×10^{-2}	0.1	0.01
5	5×10^{-2}	5×10^{-2}	10^{-5}	5×10^{-2}	0.1	0.01
6	7×10^{-3}	10^{-2}	10^{-5}	10^{-2}	0.1	0.01
7	7×10^{-3}	5×10^{-2}	10^{-5}	5×10^{-3}	0.1	0.01
8	7×10^{-3}	5×10^{-2}	10^{-5}	5×10^{-3}	0.5	0.05

[*]Zone 1 is defined as the zone starting from the pond and extending to x=0 (-20 m < x < 0 m). Zone 2 starts from 0 and extended to the right boundary (0 m < x < 75 m).

4.4.1 Effect of Beach Hydraulic Conductivity (Cases 1 to 6)

Homogenous beach (Case 2)

The Case 2 was designed to compare the results of a homogenous (one-layer) beach with the results of a two-layer system. The initial guess for the value of the hydraulic conductivity of the homogenous beach was the average value (2×10^{-3} m/s) that was obtained by using the Kozeny-Carman equation in Chapter 3. When this value or smaller values were used, the seepage face was observed in the simulations. The seepage face was not noted in the field, though. Therefore, a larger value (7.5×10^{-3} m/s) for the hydraulic conductivity of the homogenous beach was adopted. Figure 4.4 compares the simulated (and observed) water table at R2 between the one-layer (homogenous) and two-layer cases. The results of water table at R1 and R4 were presented in Appendix C

(Figure C1). Based on Figure 4.4 when tide dropped below the beach surface in the homogenous case (Case 2), the water table at R2 continued to drop with tide (with different speed) but did not remain constant at a certain elevation like the observed water table data or the simulation results of the two-layer case (Control Case). Figure 4.5 compares the pore water salinity at R2C between the homogenous case (Case 2) and the two-layer case (Control Case). The comparison results at R1B, R4A and R4B are presented in Appendix C (Figure C2). Based on Figure 4.5 the salinity in the homogenous case during the first high tide (t=57 h), rose to the seawater salinity with delay and then dropped to a value around zero. In the following two high tides the maximum salinity value was only 9 g/L. The results at other wells (Figure C2) suggest high freshwater recharge to the beach in the homogenous case (salinity dropped to zero in the wells at low tides). In conclusion, the simulations that considered the beach as homogenous could not reproduce the observed water table and pore water salinity.
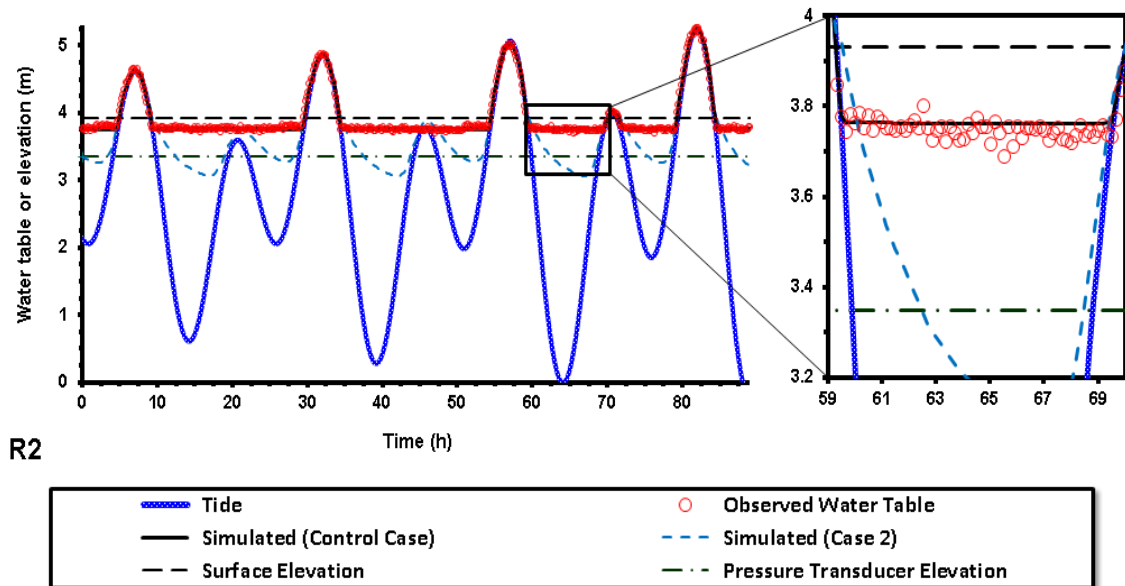
Figure 4.4 The water table at well R2 in the homogenous case (Case 2, blue dashed line) comparing to the water table in the two-layer system (Control Case, black solid line). Symbols represent the observations. The tidal level, the beach surface elevation and the elevation of the pressure transducers installed in these observation wells are shown.
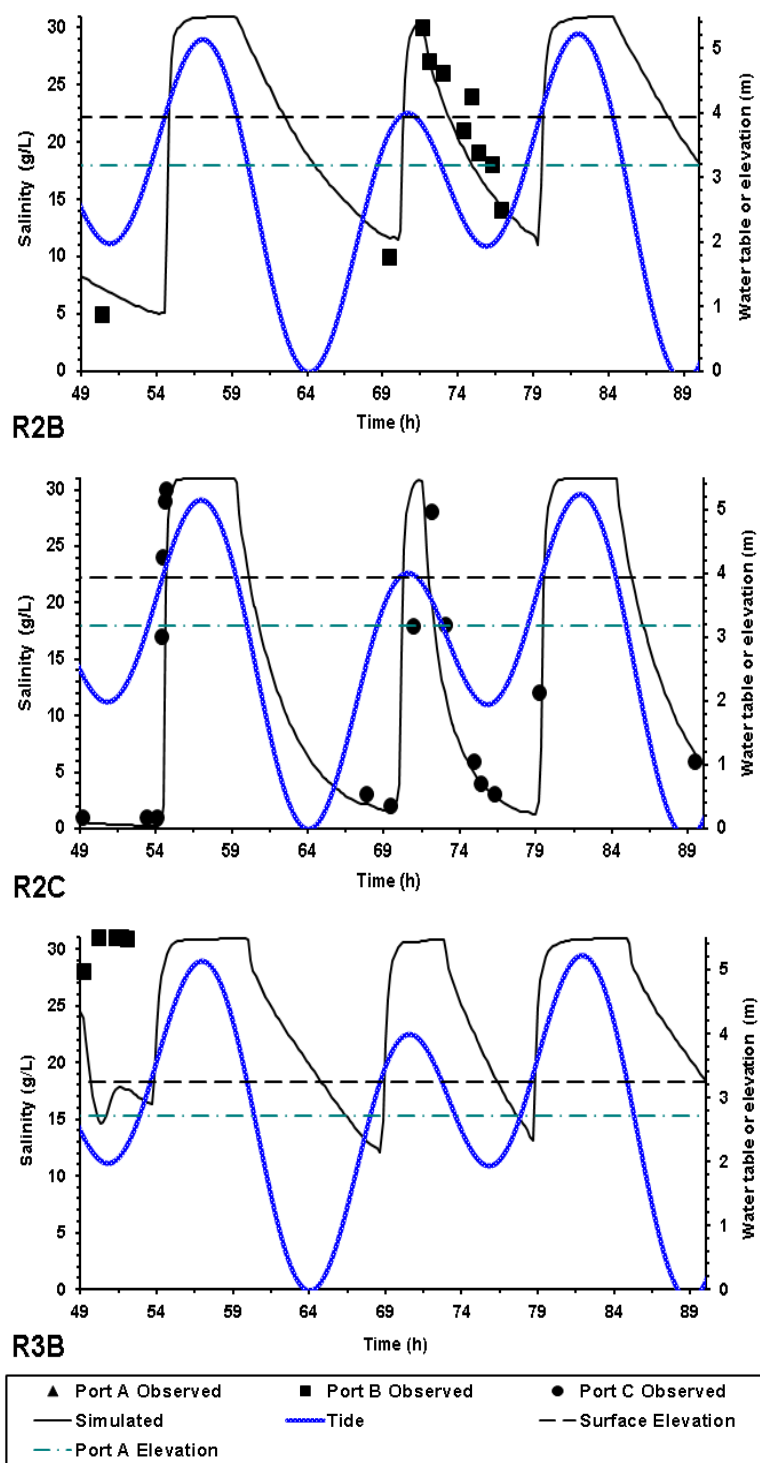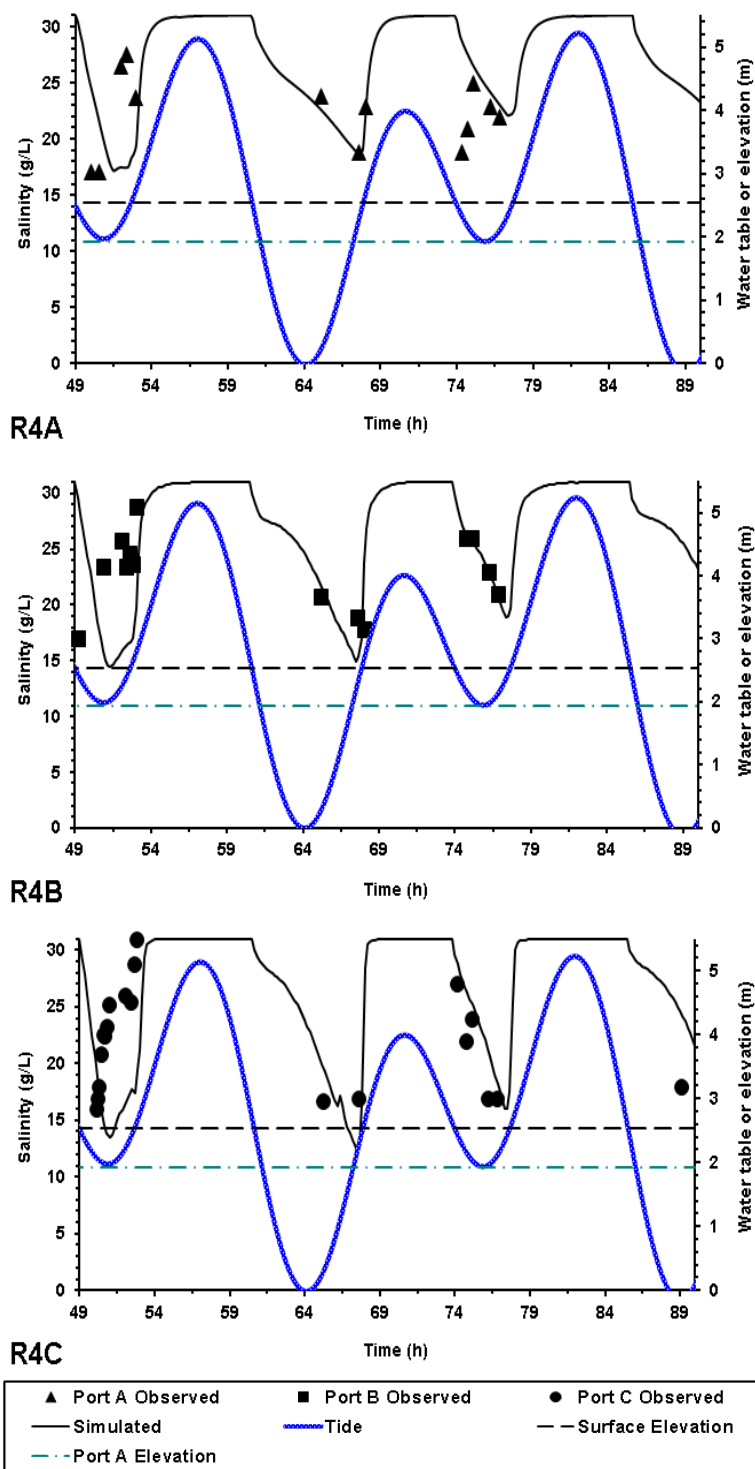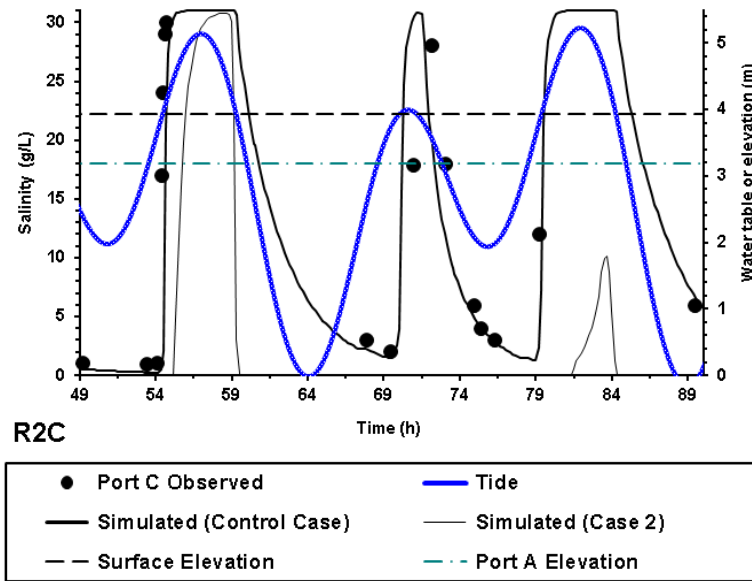
Figure 4.5 The pore water salinity at R2C in the homogenous case (Case 2, thin line) comparing to the pore water salinity in the two-layer system (Control Case, thick line). Symbols represent the observations. The tidal level, the beach surface elevation and the elevation of port A in the observation well are shown

Different Hydraulic Conductivity for the Lower Layer (Cases 3 and 4)

When the hydraulic conductivity of the lower layer increased by one order of magnitude (became 10^{-4} m/s) the water table was few centimeters lower than the observed data and simulated results of the Control Case (Figure C3 in Appendix C). The simulated water table in Case 4 was close to that of the Control Case at R1 and R6 (not shown here). The simulated salinities modeled by Case 4 were lower than the observed salinity data (Figure C4 in Appendix C). As an example, the observed salinity obtained from R2B at t=77 was equal to 14 g/L. The Control Case could reproduce the results very well. However, the simulated results in Case 4 was equal to 1 g/L at this time which is very low comparing to the observed data and simulated results of the Control Case. It should be noted that increasing the hydraulic conductivity of the lower layer affected the deeper ports more than the shallower ports (compare the results of R2B and R2C in Figure C4). In Case 3,

more freshwater could enter the pits while the water table was lower than that in the Control Case.

The water table results were not affected when the hydraulic conductivity of the lower layer decreased by one order of magnitude (became 10^{-6} m/s). The results are not shown here. Therefore, one can argue that decreasing the hydraulic conductivity of the lower layer beyond the value of the hydraulic conductivity of the lower layer in the Control Case (became 10^{-5} m/s) does not affect the water table results. However, the simulated salinities were affected by decreasing the hydraulic conductivity of the lower layer. Figure C5 reports that the salinity values simulated by Case 4 were higher than the observed values at most of the ports (For example the results at R2C). The match between the observations and the simulated results of the Control Case was better than that of Case 4. Based on the results, less freshwater could enter the pits in Case 4 in comparison to the Control Case.

Larger Hydraulic Conductivity for the Upper Layer in Zone 1 (Case 5)

When the same hydraulic conductivity (5×10^{-2} m/s) was selected for both zones of the upper layer, the salinity results indicated more freshwater recharge from the pond (Figure C6 in Appendix C). At low tides, the salinity was around zero in all of the ports even in the ports of the seaward wells (see the results at R4A and R4B). The water table was not affected by changing the hydraulic conductivity of Zone 1 (results are not presented here).

Smaller Hydraulic Conductivity for the Upper Layer in Zone 2 (Case 6)

The hydraulic conductivity of Zone 2 was decreased from 5×10^{-2} m/s (Control Case) to 10^{-2} m/s (Case 6) to test the sensitivity of the results to the hydraulic conductivity of the

upper layer in the intertidal zone. The hydraulic conductivity of Zone 1 was unchanged to keep the same recharge from the pond. The water table results simulated by Case 6 were close to that of the Control Case (the results are not presented here). Figure C7 in Appendix C compares the pore water salinity between Case 6 and the Control Case for R1B, R2C, R4A and R4B. Based on this figure, at high tides, the simulated salinity was lower in Case 6 in comparison to the observed data and to that of the Control Case (for example, note the results at R2C). At low tides, the salinity modeled by Case 6 was lower in landward wells (R1 and R2) comparing to the salinity that was modeled by the Control Case. However, the salinity in Case 6 was higher in seaward wells (like R4) comparing to the salinity in the Control Case. The salinity values in the pits were determined by the amount of seawater and freshwater entering the pits. The salinity contours of the pits (not presented here) showed that when the hydraulic conductivity of the upper layer in the intertidal zone was decreased, less amount of both freshwater and seawater entered the pits. Due to more proximity of the landward wells to the pond, the decrease in the amount of seawater entering the pits affected the salinity results more in these wells. In other hand, the pond was located farther away from the seaward wells comparing to the landward wells. Therefore, the decrease in the amount of freshwater entering the pits affected the salinity results more in the seaward wells and the salinity values at these wells were higher comparing to those in Control Case during low tides.

In conclusion, the Control Case could reproduce the observed salinity better in comparison to the Case 6.

4.4.2 Effect of Hydraulic Conductivity of the Sediments in the Pits (Case 7)

When the pits were dug, a mixture of the sediments of the surface layer and lower layer where used to backfill the pits. Despite that, in order to simulate the Control Case, the same hydraulic conductivity value of the surface layer was assigned to the hydraulic conductivity of the materials in the pits (pit effect). In other hand, the pit hydraulic conductivity (5×10^{-3} m/s) was one order of magnitude less than that of the surface layer (5×10^{-2} m/s) in Case 7. The water table results were not affected much by changing the hydraulic conductivity of the pits (the results are not presented here). However, the simulated salinity results of Case 7 were consistently lower than the observed data (Figure C8 in Appendix C). It was assumed that the beach was filled with freshwater initially. By decreasing the hydraulic conductivity of the pits, less amount of seawater could penetrate the surface layer and also penetrate deeper into the pits to raise the salinity of the pore water. As a result, the salinity values were lower for Case 7 in comparison with the observed salinity data and also in comparison with the simulated results modeled by the Control Case. Based on Figure C8, the maximum salinity values for deeper ports were less than those values for shallower ports in Case 7. For example, the maximum salinity at R1A was 14 g/L while the maximum salinity at R1B was around 21 g/L. For the Control Case, the maximum salinity at both ports was equal to the seawater salinity (31 g/L), though. Moreover, it should be noted that for Case 7 the maximum salinity values increased going seaward due to the proximity of the landward wells to the pond. For instance, the maximum salinity at R4A was 29 g/L while it was around 14 g/L for R1A in Case 7.

4.4.3 Effect of Dispersion (Case 8)

The dispersion affects the mixing between freshwater and saltwater in the beach environment. The longitudinal and transverse dispersivity coefficients were found by the calibration of the Control Case model to be equal to 0.1 m and 0.01 m, respectively. In Case 8, these coefficients were increased five times, but the water table result was not impacted. On the other hand, the salinity results were affected by increasing the dispersivity coefficients (Figure C9). The maximum salinity at all of the ports was lower in Case 8 in comparison with that in the Control Case. This indicates higher mixing of the seawater and freshwater when the dispersion was higher (higher dispersion means bigger mixing zone). Going seaward, the maximum salinity in Case 8 was closer to the seawater salinity at high tides.

4.5 Conclusion

In this chapter, the MARUN model was used to model the observed salinity and the water table data obtained from the right transect of the gravel beach in Smith Island, PWS, in the summer of 2008. There was a good agreement between the observations and the simulation results of Case 1 (Control Case). Sensitivity analysis was conducted to assess how the hydraulic conductivity and dispersivity coefficients affect the simulation results of water table and pore water salinity.

CHAPTER 5

HYPOTHESES

5.1   General

Previous chapter indicated how the MARUN model was calibrated by the observed water table and pore water salinity. Also, a sensitivity analysis was conducted to assess the effect of hydraulic conductivities, dispersivities and parameterization of the pits on the results. The sensitivity analysis revealed that the estimated parameters were well determined, especially when the goal was to match both observed water table and salinity. This chapter will define and test the following hypotheses that further explore the hydrodynamic factors in beaches:

1. Maximum seawater-groundwater exchange occurs in the mid-tide zone.

2. The high salinity wedge reduces seaward flow in the subtidal zone.

3. In the intertidal zone of the beach, the density gradient between saltwater and freshwater does not play a role.

4. Hypotheses regarding the role of bedrock in water and solute transport within the beach:

    a. Depth of bedrock (uniform depth or variable depth) and its slope greatly affects solute transport in the beach.

    b. Shallow bedrocks (small bedrock depth) minimize the effect of density gradient between saltwater and freshwater.

5. In locations with a source of freshwater recharge like a pond or freshwater stream, it is less likely to find oil

5.2   Hypothesis 1: the Maximum Seawater-Groundwater Exchange Occurs in the Mid-Tide Zone

In order to test this hypothesis, the model that was used to simulated water flow and solute transport in a gravel beach in Alaska (Chapter 4) was selected and the pit effect was excluded in the simulations (simulations of intact beach without perturbation).

The volume of seawater entering the beach (inflow) or flowing out (outflow) through the beach domain in unit length of the beach surface in the cross-shore direction and unit length in the along-shore direction per day over a spring-neap tidal cycle was calculated. Figure 5.1 outlines the percentage of inflow and outflow rates in the subtidal and intertidal zones averaged over a spring neap tidal cycle (almost 14 days).

R5 was located at the mid-tide zone of the beach. The maximum outflow rate (16.5% of the total rate) was observed around the location of R6 and the maximum inflow rate (15.5% of the total rate) was observed around R4. The higher outflow rate at R6 could be due to the change in the beach slope and also due to thicker high permeability layer in this zone. These findings suggest that during the seawater-groundwater circulation, seawater enters the beach mostly from the mid to high tide zones and groundwater leaves the beach mostly from the mid to low tide zones. In other words, the maximum seawater-groundwater occurs in the mid-tide zone and therefore the first hypothesis is validated. The works by Guo et al. (2010) and Xia et al. (2010) also confirm this finding. Sharifi et al. (2011) conducted a field study in the summer of 2009 in the same beach that this study focuses on. They concluded that the dissolved oxygen was highest in the mid-tide zone comparing to that in the high tide and low tide zones. This could be due to the higher exchange in the mid tide zone (the seawater was saturated of dissolved oxygen). This is in line with the first hypothesis.
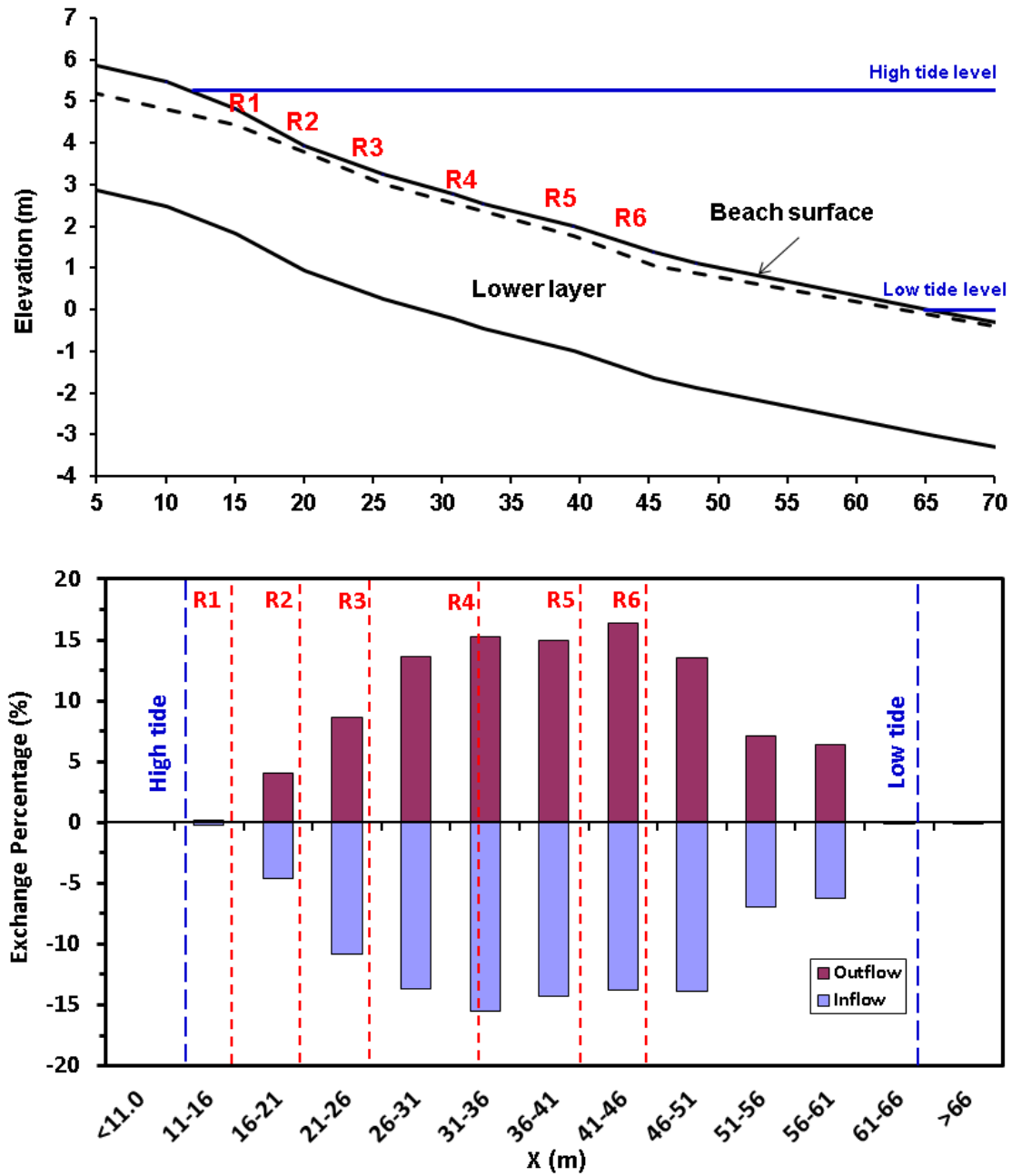
Figure 5.1 The inflow and outflow rates averaged over a spring‑neap tide cycle in subtidal and intertidal zones of the beach. The beach profile, the wells location and the high tide and low tide marks are presented.

5.3   Hypothesis 2: The High Salinity Wedge Reduces the Seaward Flow
in the Subtidal Zone (zone seaward of the low tide line)

Figure 2.6b and Figure 2.7b in Chapter 2 presented the Darcy velocity field and water table for the low and high salinity cases, respectively. These simulations were conducted under steady state condition and the beach sediment was homogenous. Based on these two figures, the flow in the offshore beach aquifer (submerged portion of beach) was negligible especially for Case 2 (high salinity case with seawater salinity similar to salinity in coastal waters).

The tidal gravel beach that was numerically simulated in in Chapter 4 was used to test this hypothesis. Figure 5.2 reports the pore water velocity and salinity (only 2 g/L and 28 g/L are presented) within the beach averaged over a spring-neap tidal cycle. The velocity vectors are shown with uniform length to indicate only the velocity direction (not the magnitude). The freshwater in the beach originated from the pond landward of the beach (velocity vectors were seaward at the domain left boundary) and the seawater entered the beach from the right boundary (seaside). The velocity values were much larger in the surface layer in comparison to the velocity values in the lower layer due to higher permeability of the surface layer. Based on Figure 5.2, the velocity magnitude significantly decreased seaward of the freshwater/saltwater interface (approximately after x = 60 m) and reached its minimum value at the right boundary of the domain.

The salt wedge seaward of the low tide line was almost stagnant considering the strong tidal action in the beach. The percentage of inflow and outflow rates seaward of the low tide line was almost equal to zero based on Figure 5.1, indicating that the high salinity wedge reduces the seaward flow in the subtidal zone. This was observed in previous studies of homogenous beaches (Abdollahi-Nasab et al., 2010; Ataie-Ashtiani et

al., 1999; Boufadel, 2000; Li et al., 2008) or two-layer system beaches in PWS, Alaska (Guo et al., 2010; Li and Boufadel, 2010; Xia et al., 2010). The effect of high salinity wedge on reducing the flow in the subtidal zone is confirmed by the investigations conducted here. As a result, the second hypothesis is validated.
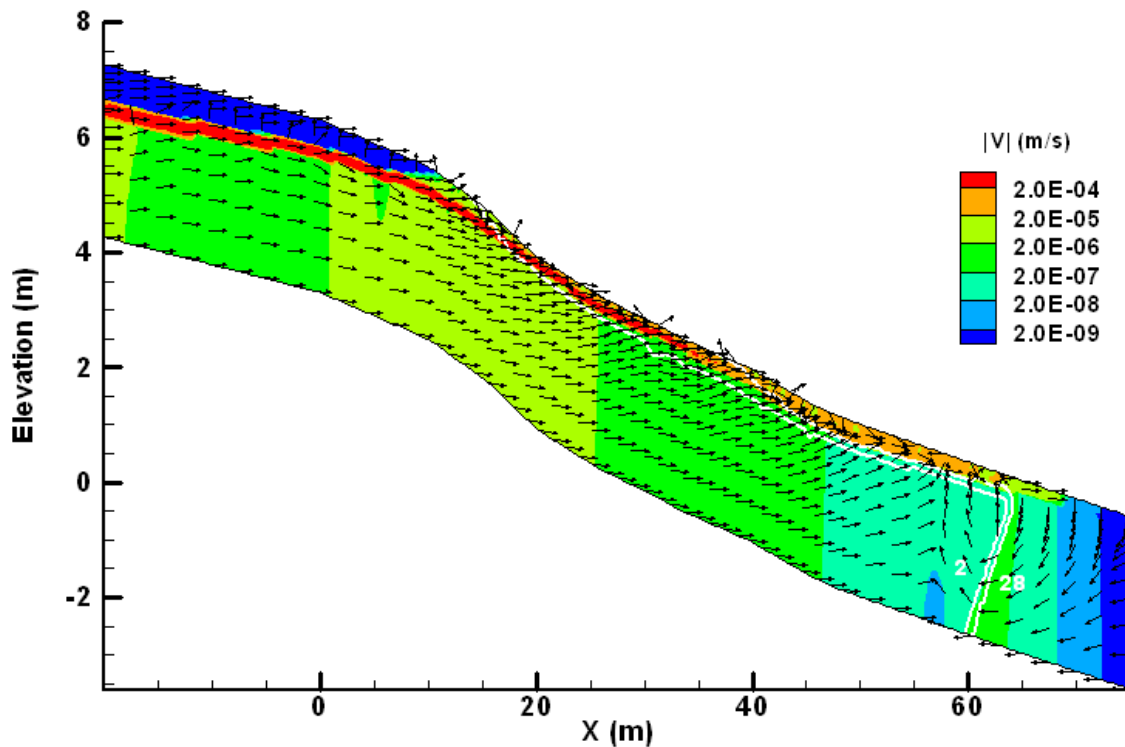
Figure 5.2 Average pore water velocity and salinity in the right transect calculated over a spring-neap tide. Vectors with uniform length were used to indicate the velocity direction but not the magnitude.

5.4   Hypotheses 3: Density Gradient Does not Play a Role in the Intertidal Zone

Abdollahi-Nasab et al. (2010) conducted experiments to investigate the flushing of saltwater out of a homogenous laboratory beach by freshwater considering no tidal action (results were presented in Chapter 2). They found that density difference between freshwater and seawater plays an important role for the high salinity case (seawater concentration of 34 g/L). On the other hand, Ataie-Ashtiani et al. (2001) used a numerical model to investigate the influence of tidal fluctuation on contaminants carried by saline groundwater to the sea. They didn not include the higher density of seawater in their model as they assumed that the gradients generated by tidal fluctuations would be substantially larger than gradients and consequential velocity components because of the density effects. The hypothesis is designed to examine how the density gradient will affect water flow and solute transport when strong tidal fluctuations are present.

In order to test this hypothesis, the simulations of water flow and solute transport in the beach studied in the previous chapter were conducted while cancelling the density effect. The term β (equation (2.2)) is the density ratio between groundwater (seawater) and freshwater. This term was set to 1 to neglect the density effect in the simulations.

In the first set of simulations, the pit effect was included and the observed salinity and water table were compared with the simulation results of the case with no density effect. Figure 5.3 shows the variation of observed and simulated water table with time at wells R1 and R4. Two simulation results are presented in the figure with one including the density effect (control case) and the other one neglecting it. For the sake of brevity only the results of only two of four wells are demonstrated. Based on this figure, ruling out the density effect was not affecting the water table results, and there was a perfect

match between the two simulated cases. Figure 5.4 shows the observed salinity at ports R1B, R2C, R4A and R4C and compares these results with the simulation results including and neglecting the density effect. For the case with no density effect, the salinity was very low at ports R1B and R2C (the maximum value was 1.5 g/L) and salinity did not fluctuate over time anymore. When the density effect was cancelled, the simulated results did not reproduce the observation results.
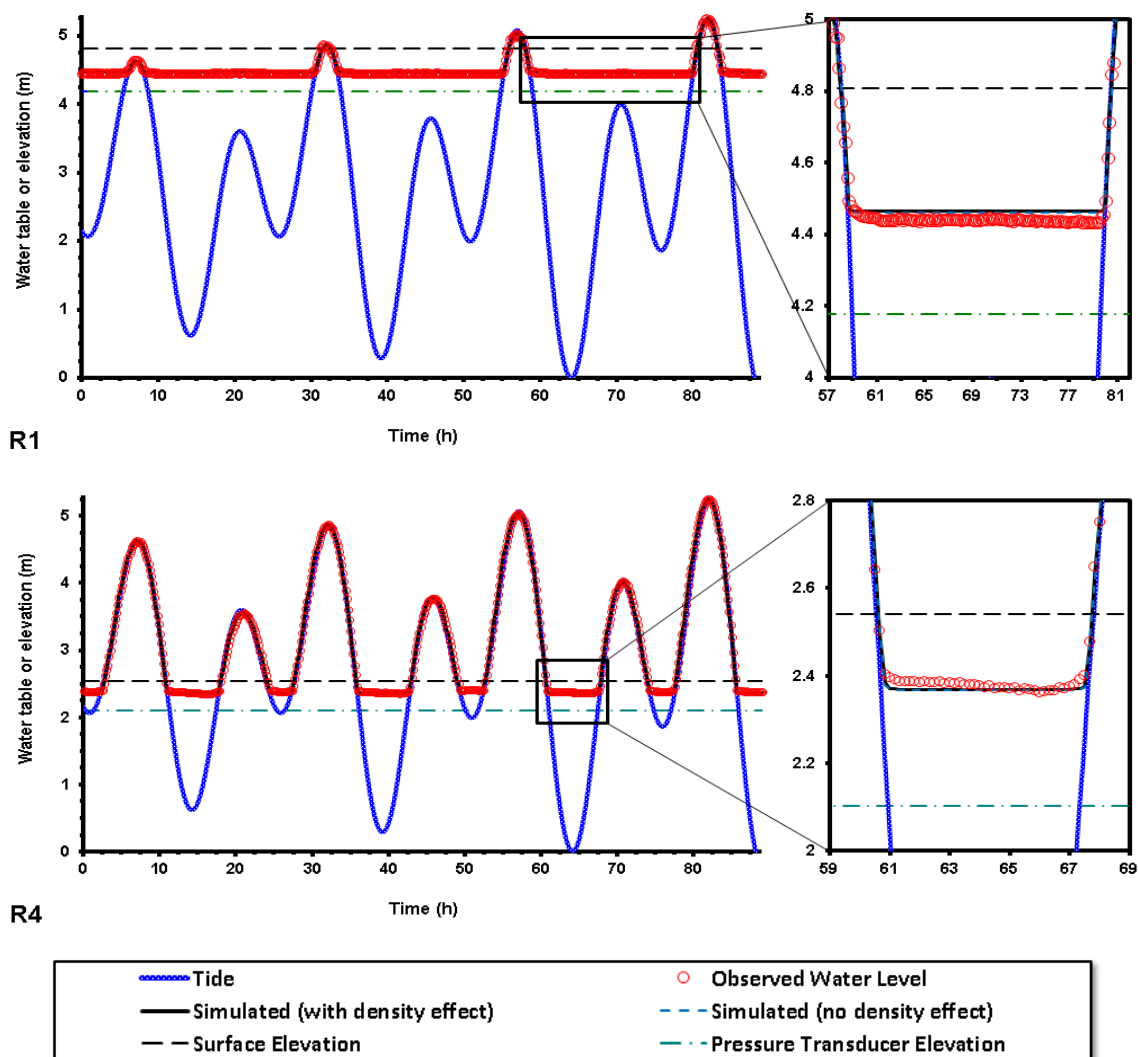
Figure 5.3 Comparison of observed (circles) and simulated water table when the density effect was neglected (blue dashed lines). The black solid lines are simulation results of the control case (including the density effect).
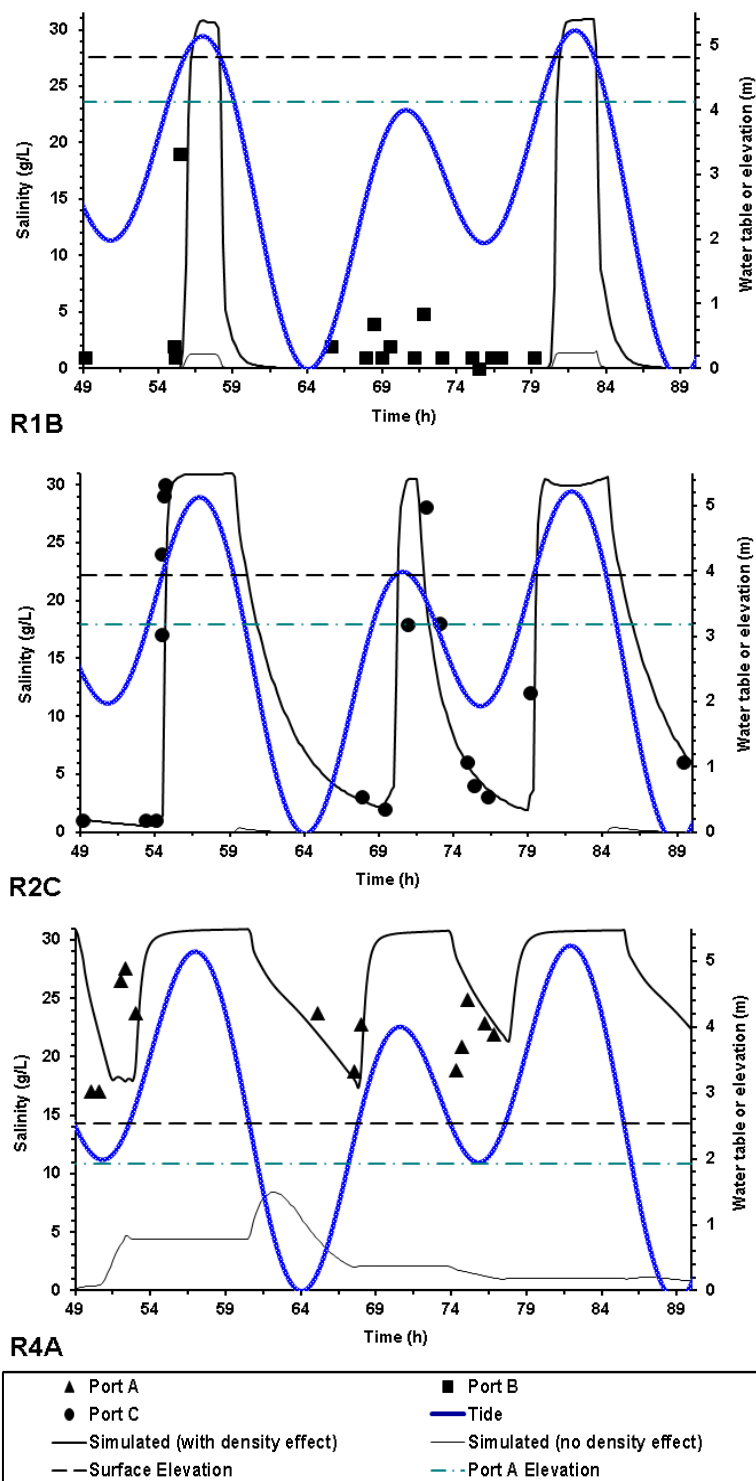
Figure 5.4 Comparison of observed salinity (symbols) with simulated results when the density effect was neglected (thin lines). The simulated salinity including the density effect is shown with thick lines.
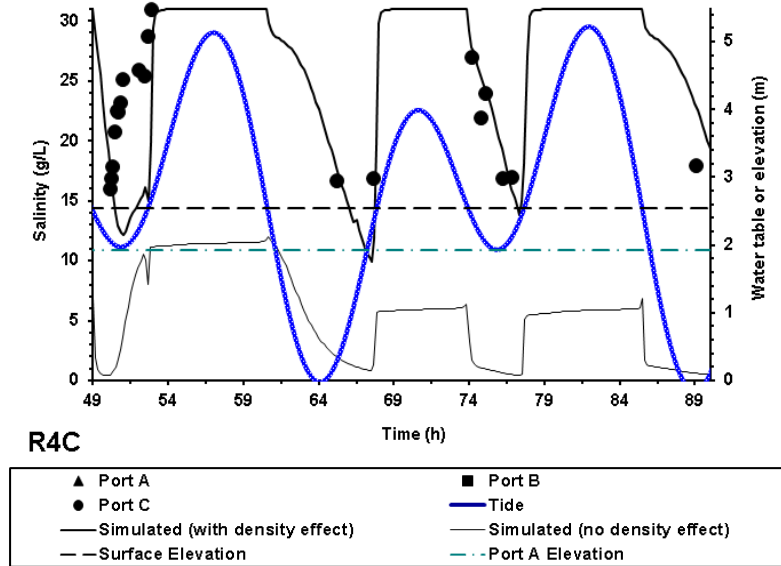
Figure 5.4 Comparison of observed salinity (symbols) with simulated results when the density effect was neglected (thin lines). The simulated salinity including the density effect is shown with thick lines. (Continued)

Figure 5.5 compares the salinity distribution at falling tide (t= 75 h) in the intact beach between the case with the density effect included and the case that neglected it. The water table in the beach is shown by black dashed line and the sea level is shown with dashed blue line. Based on Figure 5.5a, when the density effect was considered, the seawater occupied the upper layer in the submerged part of the beach. Moreover, the seawater was diluted by freshwater, landward of the intersection between the groundwater and the beach surface. In the other hand, when the density effect was not incorporated in the model (Figure 5.5b), the freshwater washed out the seawater in the upper layer. Also, the seawater did not penetrate the beach in the submerged part. Neglecting the density effect means that the seawater and freshwater have the same density and therefore buoyancy will not affect solute transport anymore. Therefore, density gradient plays a role in solute transport in the intertidal zone and the third hypothesis is consequently rejected.

It was mentioned that the density gradient between freshwater and groundwater did not affect the water table in the beach based on Figure 5.3. Moreover, comparing Figure 5.5a and Figure 5.5b suggests that the shape of water table was unaffected when the density gradient was neglected. Consequently, one could argue that density gradient does not significantly affect the water flow in the beach. This is important because density gradient between freshwater and groundwater adds to the nonlinearity of the flow and solute transport equations and as a result, more computational efforts are needed to numerically solve the equations. For example, the simulation time for the case with no density effect was 15% less than that for the control case (with density gradient). This means that for the simulations of only water flow, neglecting the density gradient will increase the simulation speed while not considerably affecting the accuracy of water flow simulations.

(a)

(b)
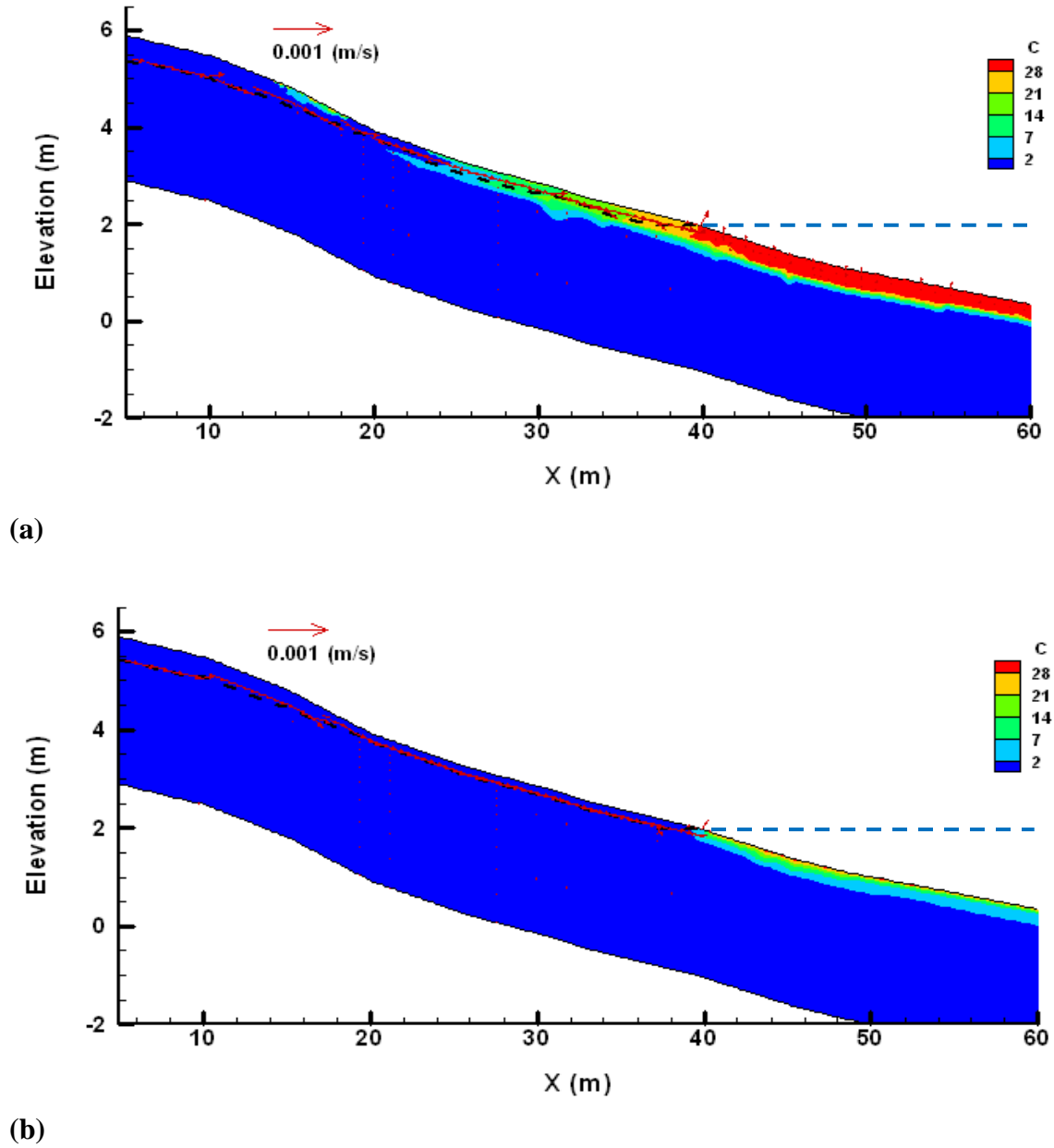
Figure 5.5 Spatial salinity distribution, groundwater table and sea level at falling tide (t=75 h) for (a) the control case (the density effect was included), (b) the case with no density effect. Banded colors are contours of salinity of the pore water, and black and blue dashed lines represent water table and sea level, respectively. Vectors indicate the velocity direction and magnitude.

5.5   Hypothesis 4: Effect of Bedrock on Solute Transport

5.5.1 Depth of Bedrock Greatly Affects the Solute Transport in Beaches

The volumetric flow rate can be defined as the flow velocity of water (or fluids) multiplied by the cross-sectional area. If the flow passage area shrinks while the flow rate is constant, the velocity magnitude consequently decreases. The flow passage area in a simple unconfined beach aquifer is bounded by the beach surface from the top and the bedrock at the bottom. Alternating the flow passage area (e.g., by considering various depths of bedrock with respect to the beach surface) could affect the solute transport in beaches. The effect of depth (and slope) of the bedrock on solute transport was noted by Li et al. (2008) who investigated the tide-induced seawater-groundwater circulation in shallow beach aquifers. The saltwater wedge seaward of the low tide line was not observed in their beach aquifer in contrast to many other studies of coastal aquifers (e.g., Ataie-Ashtiani et al., 1999; Werner and Lockington, 2006). The shallow depth of the aquifer they studied resulted in high seaward groundwater flow that washed out the saltwater wedge to sea.

In order to investigate how the depth and slope of bedrock affect solute transport, two beach domains with different depths (and slopes) of bedrock (Figure 5.6) were designed. The first domain was designed to model a shallow beach aquifer. In this case, the bedrock was assumed to be few centimeters deeper than the bottom elevation of the pits at each well (Table 3.1) and the slope of the bedrock was variable. In the second domain, the bedrock was horizontal (deep aquifer with zero slope for the bedrock) and located at the elevation of -3.6 m (with respect to the lowest low tide elevation during the

field study). As mentioned in the previous chapter, the thickness of the domain for the control case was 3 m (uniform depth, or parallel bedrock).

The simulations of water table and salinity were conducted using the three types of bedrock. The pit effect was taken into account in the first set of simulations. Results (which were not presented in this manuscript) show that the depth of bedrock didn't affect the water table in the pits and there was a perfect agreement across all the cases.

There were minor discrepancies between the salinity results for deep aquifer (horizontal bedrock) and the control case (parallel bedrock, 3 m uniform thickness of the domain). Figure 5.7 compares the observed salinity at all ports of well R4 with the simulation results of the shallow aquifer and deep aquifer. This figure shows that the maximum difference between two cases was only 2 g/L which is 6% of the seawater salinity. The salinity in the deep aquifer was lower than the salinity in the shallow aquifer most of the time. The thickness of the lower layer (low-permeability layer) in the deep aquifer was much larger than the thickness in the shallow aquifer. This means that higher freshwater recharge from left in the deep aquifer, can further dilute the seawater. Figure 5.8 compares the spatial salinity at falling tide (t=75 h) among the three domains with different bedrock depth for the intact beach. One could conclude that the upper saline plume in the intertidal zone was not greatly affected by the depth of bedrock (with respect to the beach surface). This could be due to the existence of the two layer system. The permeability of the upper layer was around three orders of magnitude higher than the permeability in the lower layer and as a result, the velocity values were much larger in the upper layer comparing to the lower layer (Figure 5.2). This means that for this

system most of the exchange occurs in the upper layer and therefore, the depth of bedrock

will not affect water flow and solute transport in the upper layer of the two-layer system.
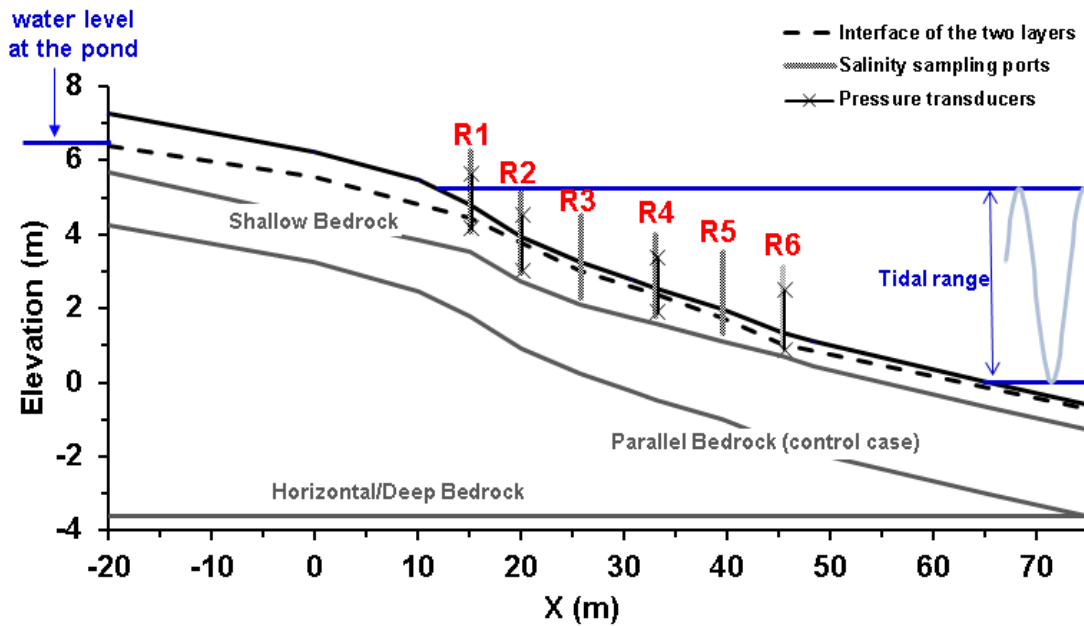
Figure 5.6 Schematic cross-section of the right transect showing the three different shapes for bedrock. Well locations (multiports/PVC pipes), the interface of the two layers, high tide line and water level at the pond are shown here.
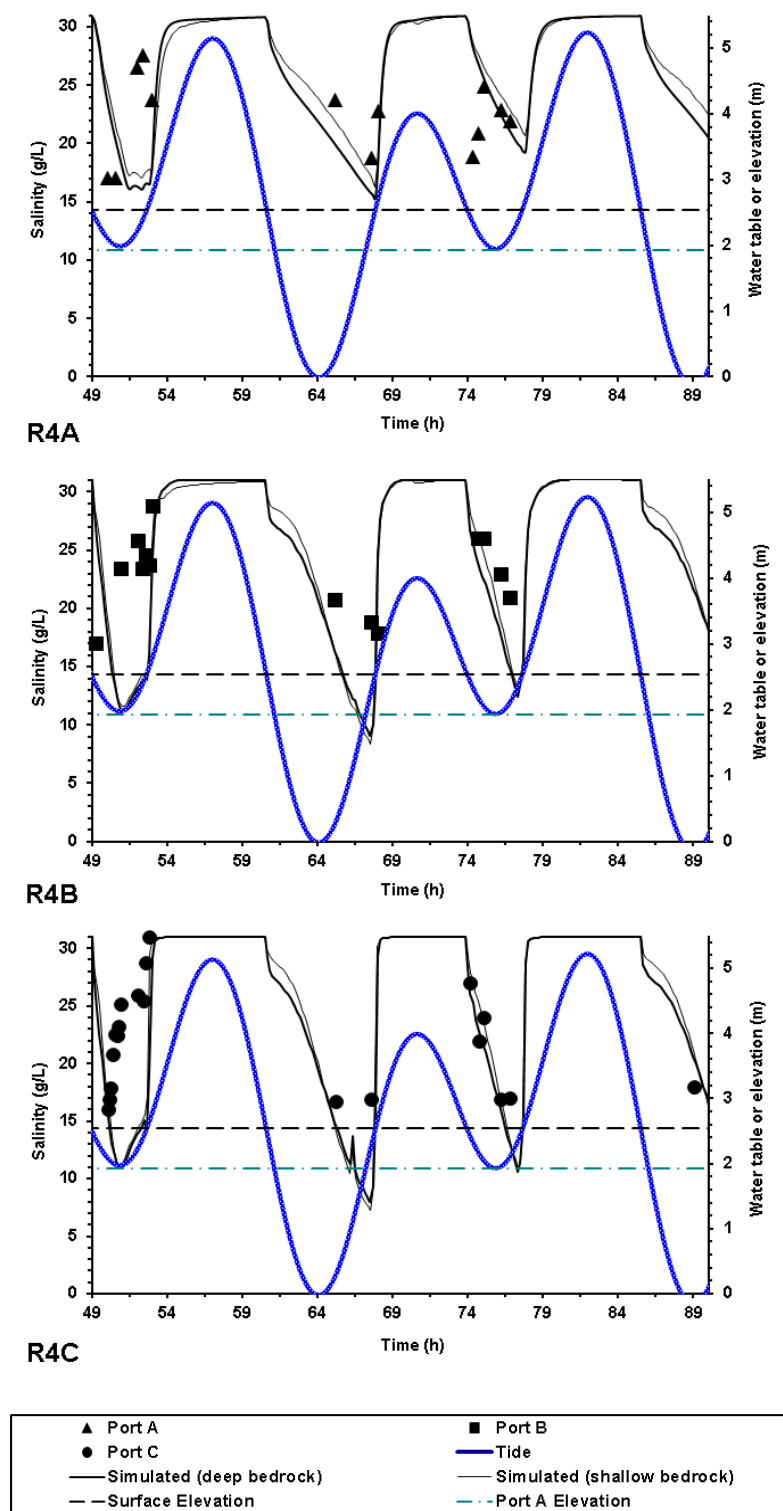
Figure 5.7 Comparison between the observed salinity data (symbols) and simulated results of the shallow aquifer (thin lines) and deep aquifer (thick lines).
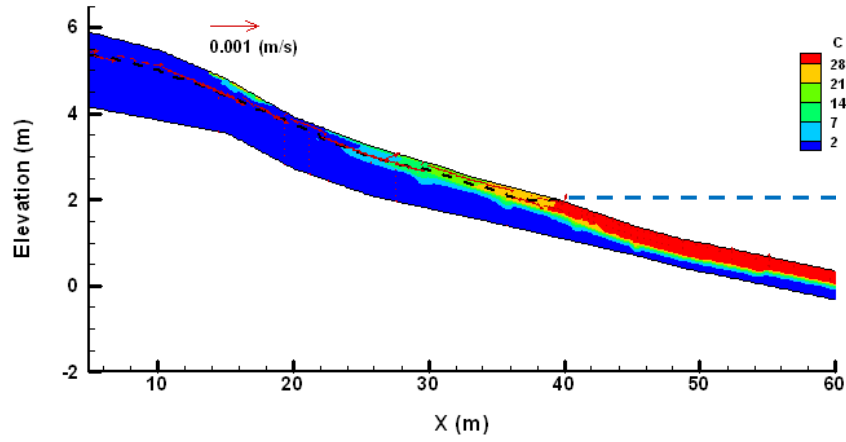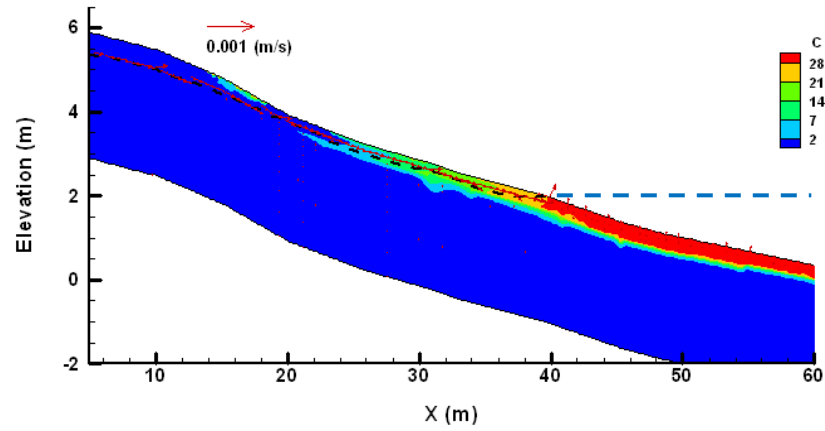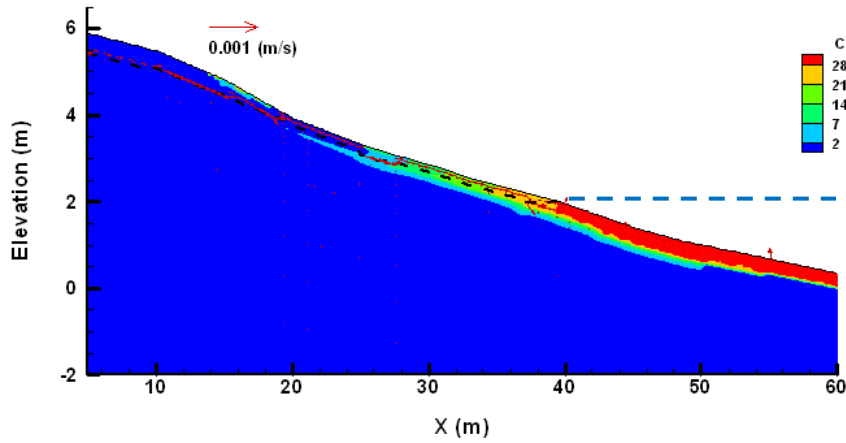
Figure 5.8 Spatial salinity distribution, groundwater table and sea level in the two-layer system beach at falling tide (t=75 h) for (a) the shallow bedrock (b) the parallel bedrock (Control Case), and (c) the deep (horizontal) bedrock. Banded colors are contours of salinity of the pore water, and black and blue dashed lines represent water table and sea level, respectively. Vectors indicate the velocity direction and magnitude.

In order to understand how the depth of bedrock (with respect to the beach surface) affects the water flow in the lower layer of the beach, a particle tracking code was developed. Random walk particle tracking (RWPM) has been used to simulate transport in porous media (Tompson, 1993, LaBolle et al., 1996). The basic idea is to approximate the travel path of a quantity by a collection of particles transporting by the velocity (and dispersion) field in the domain. In this research, this method is used to track the water particles in the beach aquifer. The equation for particle tracking can be expressed as (LaBolle et al., 1996):

$$\vec{X}_p(t + \Delta t) - \vec{X}_p(t) = (\mathrm{v} + \nabla \cdot D)\Delta t + B \cdot \Delta w \qquad (5.1)$$

where $\vec{X}_p(t)$ is the coordinates of particle p [L] at time t, Δt is the time step [T], v is the average groundwater velocity vector in the porous medium [LT^{-1}], D is the local hydrodynamic dispersion tensor [L^{2}T^{-1}] (Bear, 1972; it is defined by equation (2.9)), Δw is a vector of independent normally distributed random variables with zero mean and unit variance given as $\langle \Delta w \rangle = 0$, and B is a tensor [LT$^{-1/2}$] defining the strength of dispersion, $2D = B \cdot B^T$. The dispersion coefficient D can vary in space and in time (Aral et al., 1996; Fried, 1975; Sposito and Barry, 1987).

The pore water velocity from the MARUN simulation of the intact beach was used to run the particle tracking code. Because of the low permeability of the lower layer, the particles traveled in this layer very slowly and therefore, the MARUN code was run for several spring-neap tidal cycle to generate long term data as the input for the particle tracking code. The reason for using the particle tracking was to compare the

water pathways among the cases with different depths of bedrock. Therefore, the transport by convection was only considered and dispersion was cancelled in the code. Particles were released from a location close to the pond (x=-19.85 m, z=5.7 m).

Figure 5.9 shows the flow paths of freshwater originated from the pond and compares how the depth of bedrock (with respect to the beach surface) affects the particles transport. The particles moving in the shallow aquifer took the shortest travel distance and the particles moving in the deep aquifer took the longest travel distance. Nevertheless, the travel time of the particles was comparable among the three cases. Based on Figure 5.9, the depth of bedrock affects the solute transport at least in the lower layer of the two-layer aquifer.
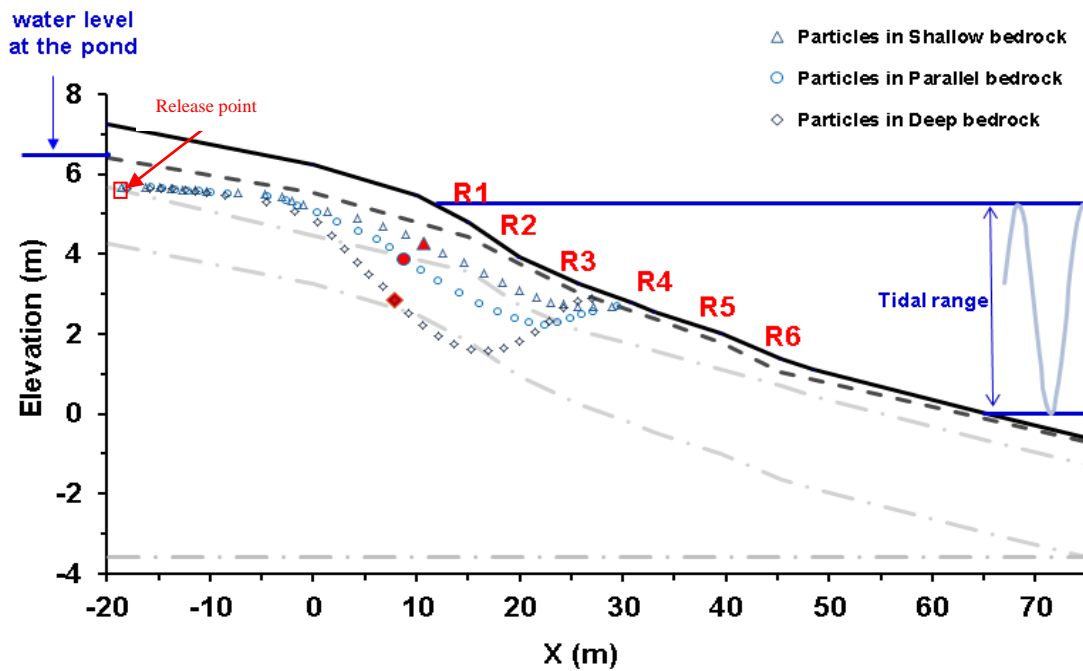
Figure 5.9 Comparison of flow paths of the freshwater particles originated from the pond among the cases with different shape of bedrock. The release point of the particles is marked in the figure. The filled symbols show the particle locations three months after the release. The dash-dotted lines present the shape of bedrock for shallow, parallel and deep aquifers. The locations of the wells are also illustrated.

In order to more generally investigate the effect of bedrock on solute transport, simulations of solute transport in a homogenous beach were conducted, considering different depths of the bedrock. The hydraulic conductivity of the model was selected to be equal to 2×10^{-3} which is the average hydraulic conductivity calculated using the Kozeny-Carman equation and by analyzing the sediment properties (the results were presented in Chapter 3). Figure 5.10 compares the salinity distribution in the homogenous shallow aquifer, aquifer with uniform bedrock depth (parallel bedrock) and deep aquifer. Based on this figure, bedrock depth highly affects water flow and salinity distribution within the homogenous beach. The thickness of beach at the left boundary was largest for the deep aquifer and smallest for the shallow aquifer. This means that more freshwater entered the beach from the left boundary in the deep aquifer comparing to two other cases. Velocity vectors exiting the domain at the interface of water table and beach surface were largest for the deep aquifer as well, due to the higher freshwater recharge. In the shallow aquifer, the diluted seawater occupied most of the intertidal zone form the beach surface to the bedrock probably because of the lower freshwater recharge. In the parallel bedrock aquifer, the freshwater tube can be observed at x=55 m close to the saltwater wedge. The freshwater tube was noted by Boufadel (2000) in a homogenous beach. In the deep aquifer, a thin layer of diffused saline plume occupied the intertidal zone at the top and the remaining part of the beach was filled with freshwater. In a nutshell, the hypothesis is validated for homogenous beaches. In gravel beaches that are consisted of two layers with very different hydraulic conductivities, most of exchange between groundwater and seawater occurs in the upper layer and the solute transport will not be affected by the depth of bedrock in that layer.
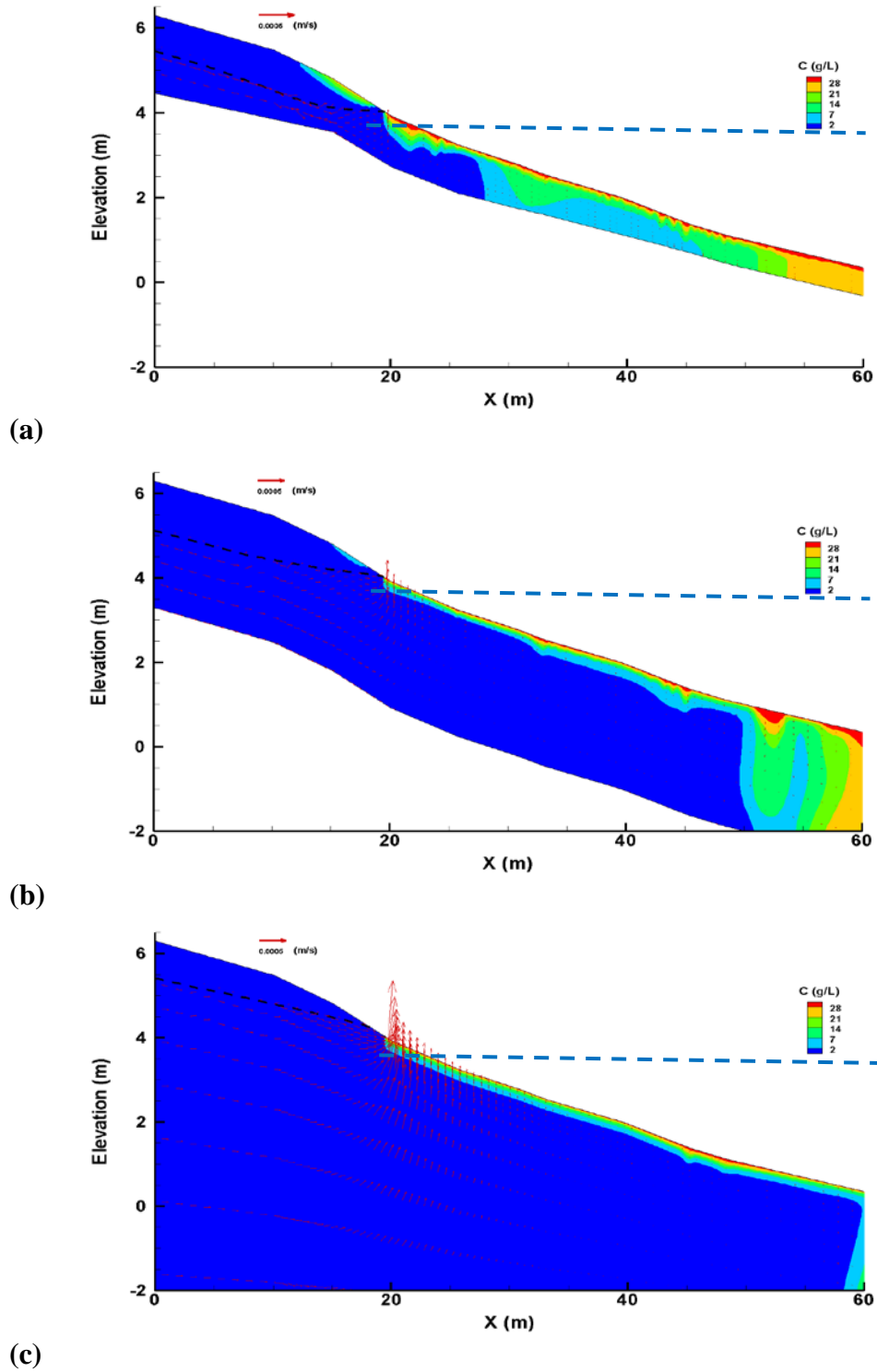
Figure 5.10 Spatial salinity distribution, groundwater table and sea level in homogenous beach at high tide (t=71 h) for (a) the shallow beach aquifer (b) aquifer with parallel bedrock, and (c) the deep beach aquifer (horizontal bedrock). Banded colors are contours of salinity of the pore water, and black and blue dashed lines represent water table and sea level, respectively. Vectors indicate the velocity direction and magnitude.

5.5.2 Shallow Bedrocks Minimize the Effect of Density Gradient between Saltwater and Freshwater

In order to test this hypothesis, the density effect was neglected and simulation results of the salinity were compared between the shallow and deep aquifers. Figure 5.11 highlights this comparison at ports R1B, R2C, R4A and R4C. Based on this figure, although the salinity results in the case with shallow aquifer were improved slightly comparing to the results in the deep aquifer (compare the salinity at R2C), the simulation neglecting the density effect was still not able to reproduce the observed data. The average salinity in the shallow aquifer is higher than that in deep aquifer. This is probably due to slightly higher freshwater recharge in the deep aquifer. However, one could argue that the effect of density gradient on the solute transport is more important than the effect of bedrock shape. In other word, the hypothesis is rejected.
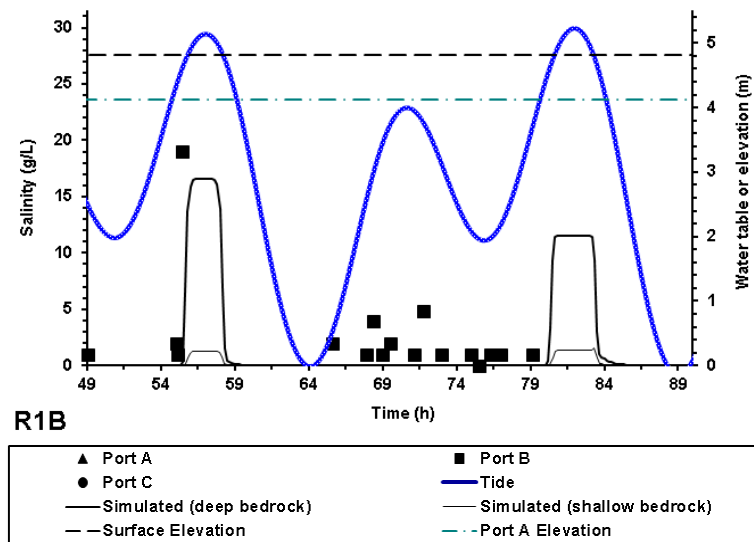
Figure 5.11 Comparison of observed salinity data (symbols) with simulated results of the shallow aquifer (thin lines) and the deep aquifer (thick lines) when the density effect was neglected.
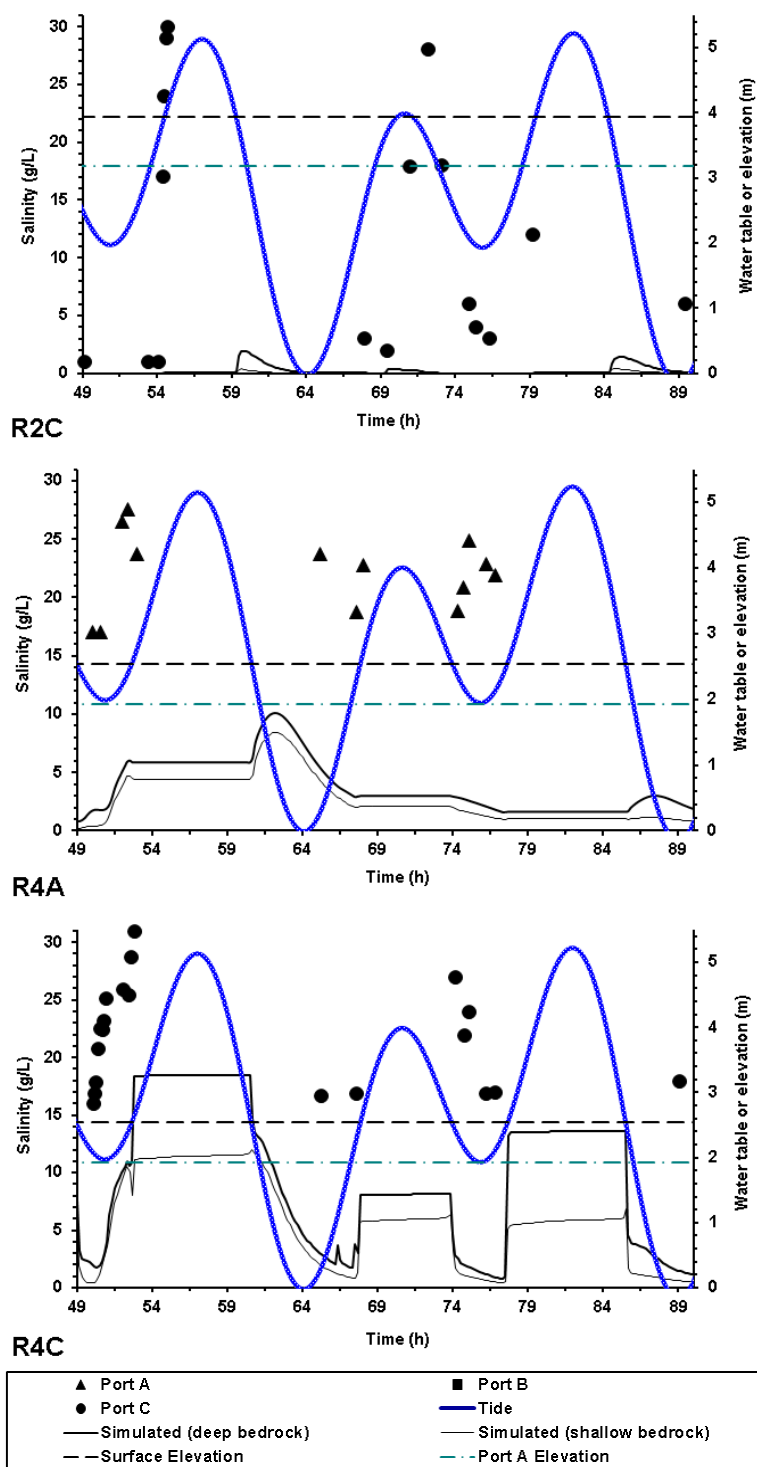
Figure 5.11 Comparison of observed salinity data (symbols) with simulated results of the shallow aquifer (thin lines) and the deep aquifer (thick lines) when the density effect was neglected. (Continued)

5.6 Hypothesis 5: It Is Less Likely to Find Oil in Locations with a Source of Freshwater Recharge like a Pond or Freshwater Stream

Michel et al. (2009) studied several beaches in Prince William Sound. Based on their observations, there was no subsurface oil lingering in the beaches where a small pond occurred behind the storm berm. The mechanism that relates the freshwater recharge to the oil disappearance from some of the gravel beaches in Alaska is explored here.

To monitor the pond water level fluctuations, a PVC pipe was placed in the pond and a pressure transducer was deployed in the PVC pipe.

Figure 5.12 reports the pond water level and water temperature fluctuations over one year after the study period in summer of 2008. The pond water level was equal to 6.5 m during the field study. From July 2008 to June 2009, the minimum, maximum and average water levels were equal to 6.20 m, 7.15 m and 6.75 m, respectively. To explore how the freshwater in the pond affects the water table in the beach, two simulations with different pond water levels were designed. For the first case, the water level in the pond was equal to the yearly average of that (6.75 m). For the second case, the water level at the pond was set equal to 5.6 m which was 40 cm above the level of highest high tide. This level is assumed to be the lowest level of water table in the beach far enough from the intertidal zone. The simulations were conducted with the pit effect included. Figure 5.13 compares the water level at the pits, assuming three different pond water levels.

Based on Figure 5.13, when the water level was lowest in the pond (pond water level at 5.6 m) the water table at R1 and R2 dropped few centimeters below the interface of the two layers. On the other hand, the water table at R4 and R6 stayed on the interface for the whole period. When the water level at pond was at the elevation of 6.5 m (during the field study), the water table at the wells stayed at or above the two layers interface.

When the simulations were conducted considering the water level in the pond equal to the average of that over a year (pond water level of 6.75 m), the water table at the pits stayed few centimeters above the interface of the two layers in all of the wells. This means that even at the lowest low tide there was always freshwater flow in the pits.
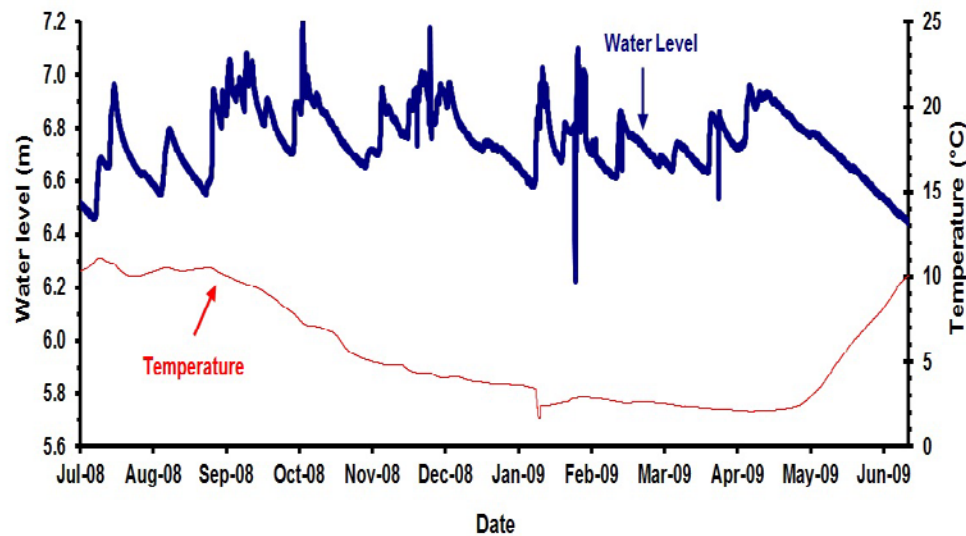
Figure 5.12 Pond water level (with respect to zero elevation) and water temperature fluctuations over one year.

It can be argued that at the time of Exxon Valdez oil spill, after the oil reached the beaches in PWS, the upper layer stored the oil temporarily. Whenever the water table dropped below the two layers interface, the oil penetrated into the lower layer and entrapped there because of the capillary forces due to the fine sediments of the lower layer. The oil persisted on the left side of the beach (studied here) between the mid-tide line and the low tide-line (Short et al., 2004). The right side of the beach was clean at the time of the field study, though. The observed results presented in Chapter 3, suggest that there was higher freshwater recharge to the right side of the beach comparing to the left

side. Based on the results presented in Figure 5.13, for any water levels at the pond, the water table stayed always at or above the interface of the two layers at least at the wells R4 and R6 which were located in the mid tide and low tide zone of the beach, respectively. It can be concluded that high freshwater recharge promotes the removal of oil by sustaining a high water table in the intertidal zone at low tides. The same mechanism was observed in the work of Li and Boufadel (2010) Xia et al. (2010) and Guo et al. (2010). The hypothesis is validated as the water table was always above the interface of the two layers at the zone (low to mid tide zone) where the oil was found at the left side of the beach and other polluted beaches in PWS, Alaska.

If beaches with similar setup of the beach studied here (two-layer system) are polluted, it is important to keep the oil from penetrating to the lower layer. This can be done by injecting water into the upper layer at high tide line to sustain the water table above the interface of the two layers in the intertidal zone.
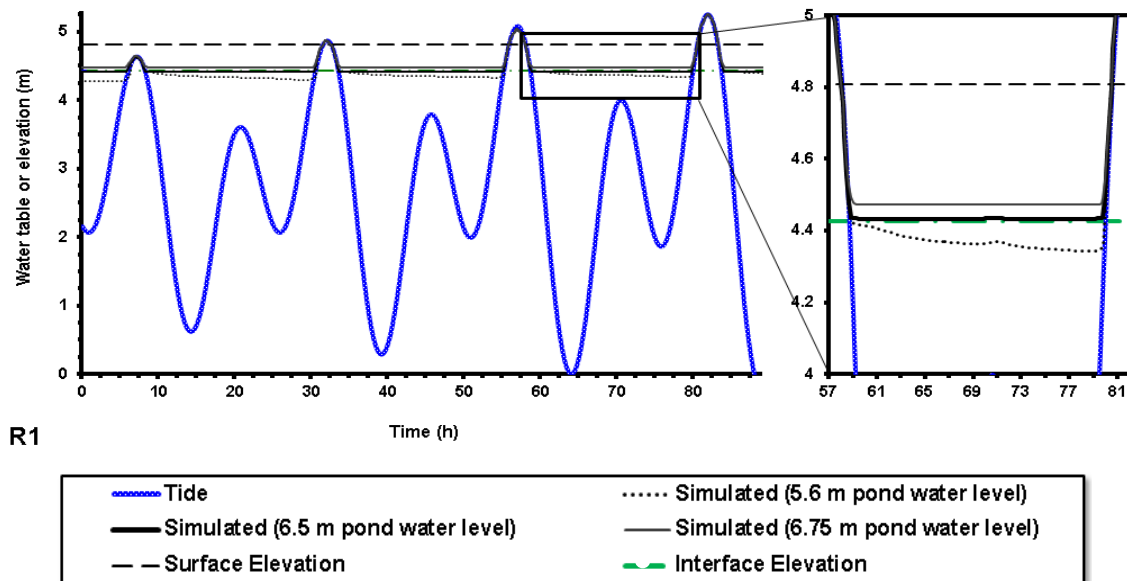
Figure 5.13 Comparison of simulated water table in the beach for the cases with different water level in the pond. The elevation of the interface of the two layers is presented with green dash-dotted line.
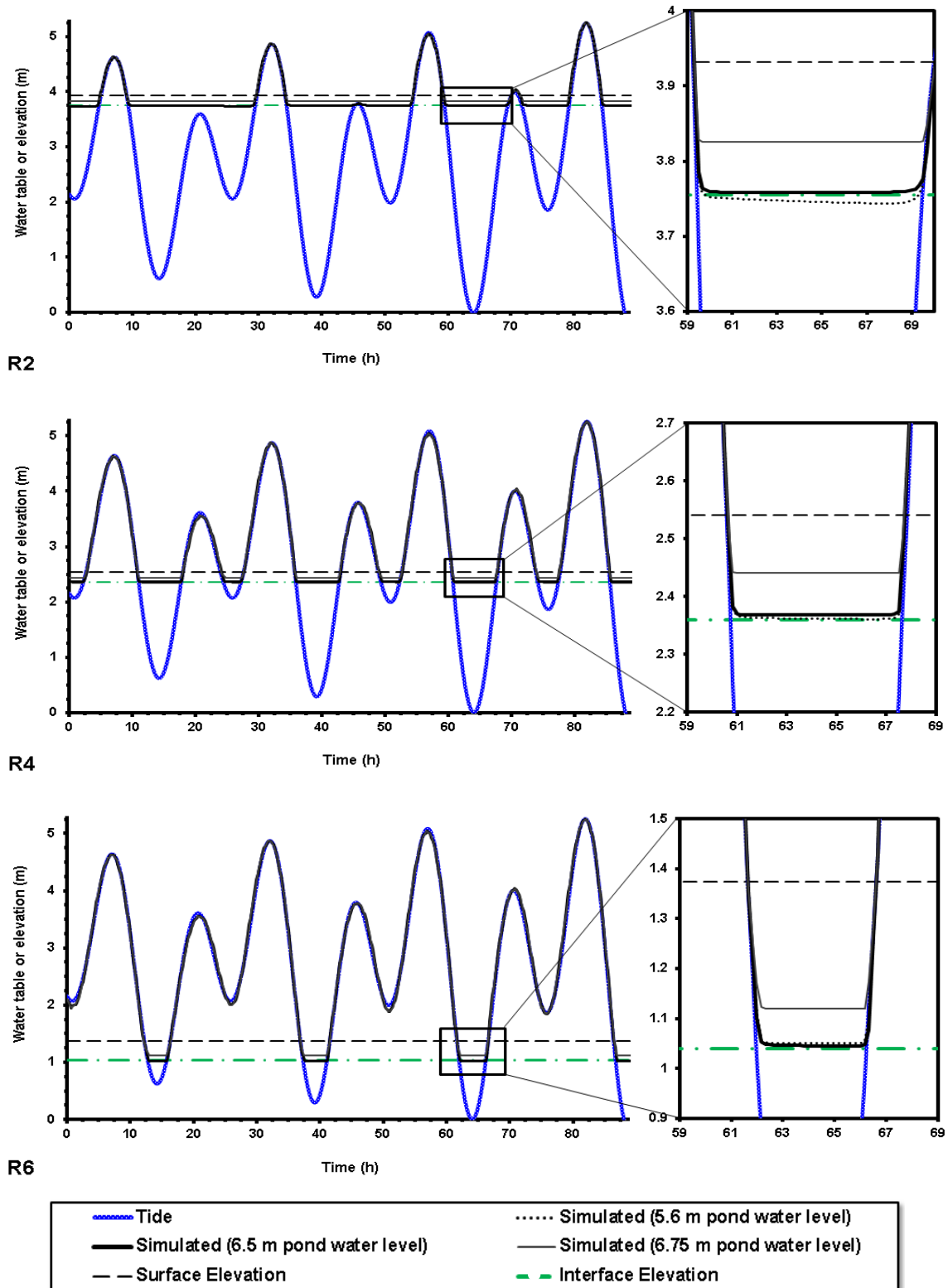
Figure 5.13 Comparison of simulated water table in the beach for the cases with different water level in the pond. The elevation of the interface of the two layers is presented with green dash-dotted line. (Continued)

5.7   Conclusion

Five hypotheses related to the hydrodynamic factors in the beaches were defined and tested by conducting numerical simulations. The following synopses summarize how these hypotheses were addressed.

1. Maximum seawater-groundwater exchange occurs in the mid-tide zone.

2. The high salinity wedge reduces seaward flow in the intertidal zone.

3. The density gradient between the saltwater and freshwater affects solute transport in the intertidal zone of the beach.

4. Depth (and slope) of bedrock greatly affects solute transport in homogenous beaches while it has a minor effect on the solute transport in the upper layer of two-layer beaches. Moreover, depth of bedrock does not play significant role in minimizing the effect of density gradient (between saltwater and freshwater) on the solute transport in beaches.

5. In locations with a source of freshwater recharge like a pond or freshwater stream, it is less likely to find oil as the high freshwater recharge maintains the water table in the intertidal zone at or above the interface of the two layers. This can prevent the oil from penetrating to the lower layer and from persisting there for an extended period of time.

CHAPTER 6

SUMMARY AND CONCLUSIONS

The focus of this work was on the analyses of hydrodynamic factors affecting the water and solute transport in beaches and to evaluation of their potential impact on coastal areas that are subjected to multiple stressors such as saltwater intrusion, sea level rise and oil spills pollution. The investigation was carried out through two case studies; the first one implemented experimental and numerical techniques to quantify the flushing of saltwater in a laboratory beach subjected to steady state condition. Two initial uniform concentrations were used: Case 1: 2.0 g/L (low salinity case), and Case 2: 34.0 g/L (high salinity case). The observed salinity and pressure data were closely reproduced using the MARUN numerical code. The results indicated that buoyancy played an important role in Case 2 but was negligible for Case 1. The results also indicated that the flow in the offshore beach aquifer was negligible compared to the flow in the onshore aquifer in the both cases. For the high salinity case, the pressure increased over time until reaching a peak and then decreased (i.e., humps were formed). This was not observed in the low salinity case. The pressure humps were not noted previously in the literature. The results obtained from the first case study have important implications for analysis of the dynamics of saltwater flushing and the discharge location of an aquifer to its abutting open waters, such as rivers, lakes and sea where the waves and tides are negligible. It was concluded that if the slope of the beach surface is mild below the water surface, then the inland groundwater discharge will then exit around the intersection of the surfaces of the open water and the interface. This gives useful guidelines in relation to the sampling location of the groundwater discharge into open waters using the seepage meter.

The second case study consisted of simulating the observation results of water table and pore water salinity obtained from a field study in a tidal gravel beach located in PWS, Alaska. Oil persisted on the left side of the beach (when looking landward from sea) but no oil residues were found in the right side of the beach at the time of the field study. The observed water level results, the in-situ and lab sediment analyses and the field observations indicated the presence of a two-layer structure in the beach. This system is characterized by a high permeability layer over a much lower permeability later. The two-layer system could promote oil persistence in beaches of PWS: The observed salinity and the tracer study suggested higher freshwater recharge to the right transect in comparison to the left transect. Freshwater recharge from the land promotes the removal of oil by sustaining a high water table in the beach during low tides and subsequently preventing the oil from dropping into the lower layer. Also, high seaward flow could cause the dislodgement of oil and its washout to sea.

In comparison to the studies conducted in the same general region (PWS), the role of freshwater and the effect of salinity were elucidated in more details in this dissertation. Also, absence of the two-layer system was introduced as one of the reasons for the long term persistence of the Exxon Valdez oil. The in-situ hydraulic conductivity test could estimate the value of the hydraulic conductivity of different layers quickly and somehow accurately (one order of magnitude difference in comparison with the values estimated by model calibration, which is fairly accurate for the hydraulic conductivity). This method can be used in the field in similar studies.

Five hypotheses related to the hydrodynamic factors in the beaches were defined and tested by conducting numerical simulations. The following synopses summarize how these hypotheses were addressed.

1. Maximum seawater-groundwater exchange occurs in the mid-tide zone.

2. The high salinity wedge reduces seaward flow in the intertidal zone.

3. The density gradient between the saltwater and freshwater affects solute transport in the intertidal zone of the beach.

4. Depth (and slope) of bedrock greatly affects solute transport in homogenous beaches while it has a minor effect on the solute transport in the upper layer of two-layer beaches. Moreover, depth of bedrock does not play significant role in minimizing the effect of density gradient (between saltwater and freshwater) on the solute transport in beaches.

5. In locations with a source of freshwater recharge like a pond or freshwater stream, it is less likely to find oil as the high freshwater recharge maintains the water table in the intertidal zone at or above the interface of the two layers. This can prevent the oil from penetrating to the lower layer and from persisting there for an extended period of time.

Findings from this work in relation to oiled beaches include: 1) oil tends to persist at locations of small freshwater recharge, 2) Prior to oil arriving to the shoreline, one could minimize oil penetration into the beach by releasing water onto the beach at the high tide line during low tides, and 3) bioremediation of oil polluted beaches should be conducted using deep injection as amendments applied on the beach surface would washout rapidly to sea.

It is proposed to simulate numerically the results of the tracer study and also the observed results of salinity and water table at the left transect in order to better understand the solute transport in a two-layer system beach. .

Waves are one of the factors affecting water flow and solute transport in beaches and are important in quantifying submarine groundwater discharge, transport of

contaminants to ocean and bioremediation of oil spills. Therefore, it is proposed to evaluate the effect of waves on solute transport in beaches especially in two-layer system beaches in future studies.

Sharifi et al. (2011) measured the dissolved oxygen in various locations in the same beach studied in this dissertation. The oxygen depletion as a result of water transport within the beach sediment (and chemical or biological reactions) can be simulated by proper modeling tools.

Different remediation techniques can be explored numerically or in the lab and advantages and disadvantages of each method can be compared to provide guidelines for the remediation of the oil polluted beaches.

APPENDIX A

DOCUMENTATION FOR MARUN MODEL

MARUN model is finite element code capable of solving a wide variety of two-dimensional, variably saturated flow in porous media. The equations were solved using Galerkin scheme in space and a mass lumping backward Euler integration in time. The modified Picard iteration scheme was used to determine the temporal derivatives.

MARUN model has been verified and validated and has been extensively used to simulate water flow and solute transport in beach environment.

A simple flowchart of the MARUN model is presented in the next page. The inputs of the model are mesh and beach soil properties as well as the initial and boundary conditions. The mesh size should be selected in a way that ensures that the grid Courant number is less than 1.0 for numerical stability and that the grid Peclet Number is less than 2.0. The user should conduct a mesh refinement study to get to the block size below which there is no practical change in the solution. This issue is addressed in Boufadel et al. (1999b).

The flowchart for MARUN model

```
                    ┌─────────────┐
                    │    Start    │
                    └─────────────┘
                           │
                           ▼
                 ┌──────────────────────┐
                 │ Set parameters values│
                 │ Read mesh properties │
                 └──────────────────────┘
                           │
                           ▼
                 ┌──────────────────────┐
                 │Read the Initial      │
                 │condition             │
                 └──────────────────────┘
                           │
                           ▼
                 ┌──────────────────────┐
                 │   Next time step     │◄───────────┐
                 └──────────────────────┘            │
                           │                         │
                           ▼                         │
                      ╱Reach   ╲        Yes    ┌──────────┐
                     ╱ maxtime? ╲──────────────│   Stop   │
                      ╲         ╱               └──────────┘
                           │ No
                           ▼
           ┌────────────────────────────────────┐
           │Read the boundary condition if it is│
           │the first time step, otherwise      │
           │update it                           │
           └────────────────────────────────────┘
                           │
                           ▼
                 ┌──────────────────────┐
                 │Start the iteration for│◄──┐
                 │pressure calculation  │    │
                 └──────────────────────┘    │
                           │                 │
                           ▼                 │
                 ┌──────────────────────┐    │
                 │Assemble pressure     │    │ No
                 │matrices              │    │
                 │Solve the matrices    │    │
                 └──────────────────────┘    │
                           │                 │
                           ▼                 │
                      ╱ Results  ╲───────────┘
                     ╱ Converged? ╲
                      ╲          ╱
                           │ Yes
                           ▼
                 ┌──────────────────────┐
                 │Assemble velocity     │
                 │matrices              │
                 │Calculate the velocity│
                 └──────────────────────┘
                           │
                           ▼
        ┌──────────────────────────────────────┐
        │Check the Courant number and modify    │
        │the time step                          │
        └──────────────────────────────────────┘
                           │
                           ▼
                 ┌──────────────────────┐           ╱ Results  ╲   No
                 │Assemble salinity     │──────────╱ Converged? ╲──────┐
                 │matrices              │           ╲          ╱       │
                 │Solve the matrices    │                │ Yes         │
                 └──────────────────────┘                │             │
                           ◄────────────────────────────┘             │
                           ▼                                          │
                 ┌──────────────────────┐                            │
                 │Assemble nutrient     │                            │
                 │matrices              │                            │
                 │Solve the matrices    │                            │
                 └──────────────────────┘                            │
                           │                                         │
                           ▼                                         │
                    ┌─────────────┐                                 │
                    │  Output:    │                                 │
                    │  Results    │                                 │
                    └─────────────┘                                 │
                           │                                        │
                           ▼                                        │
           ┌────────────────────────────────────┐                 │
           │Results ---> Initial values for next │                │
           │iteration                           │                 │
           └────────────────────────────────────┘                 │
```
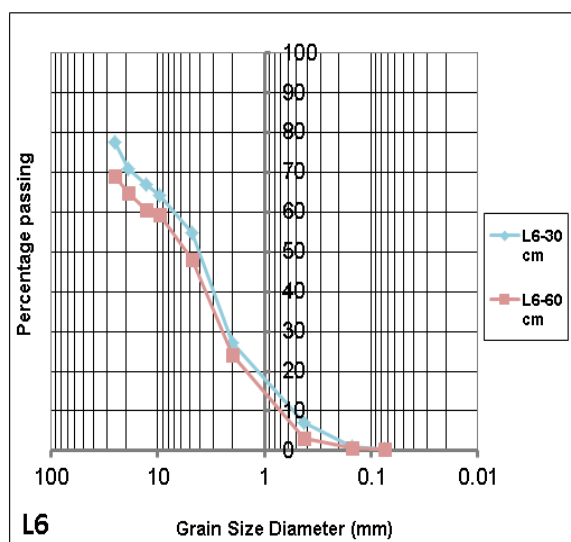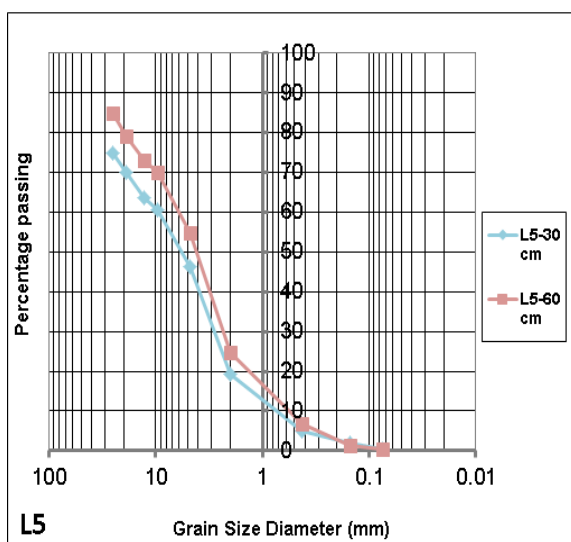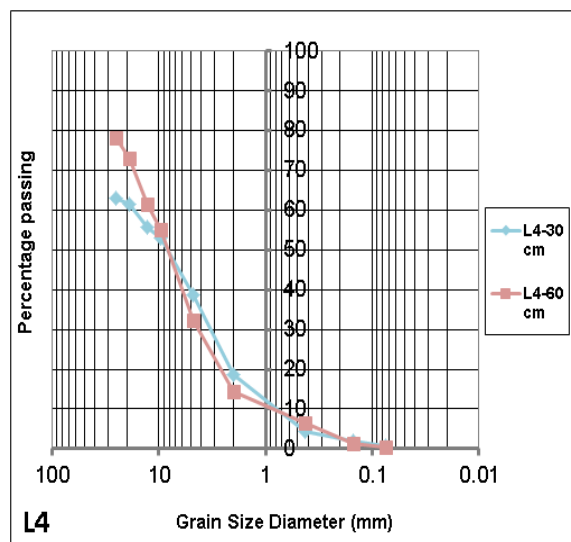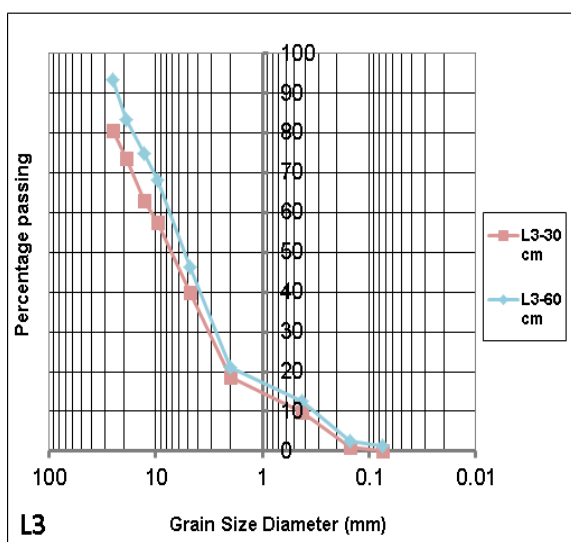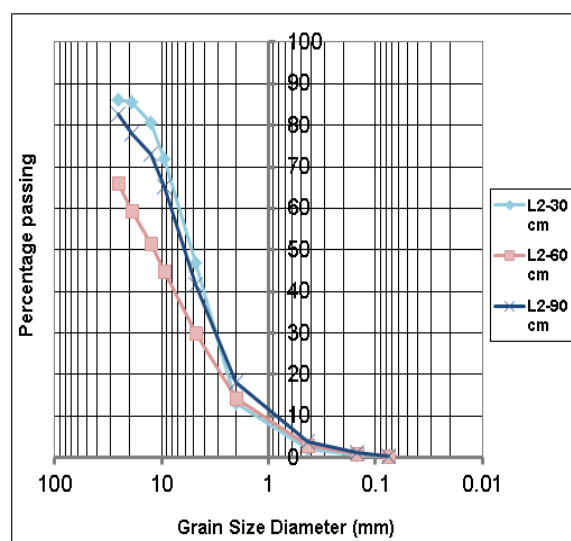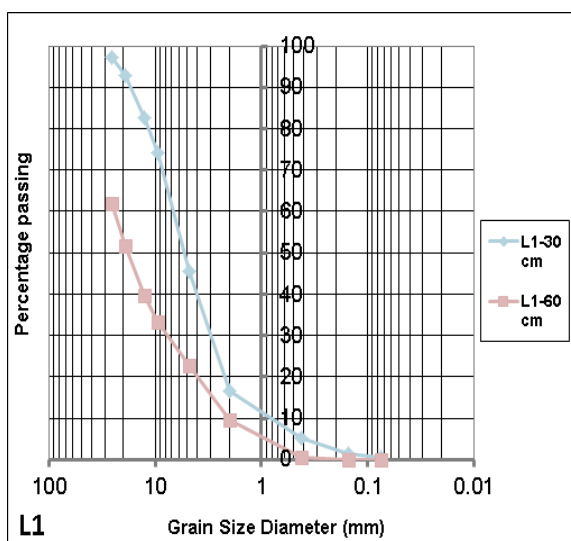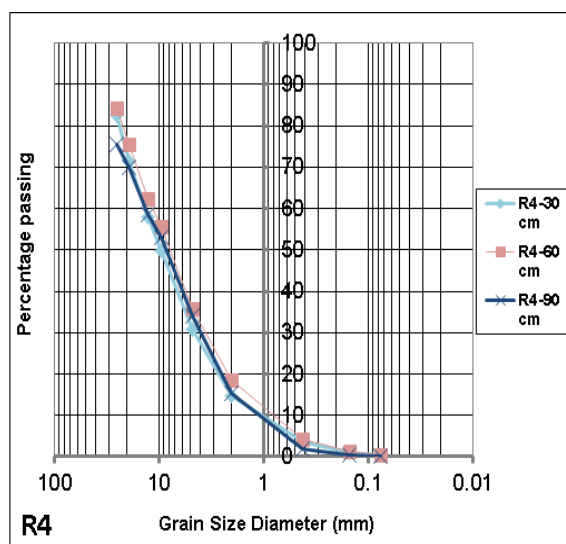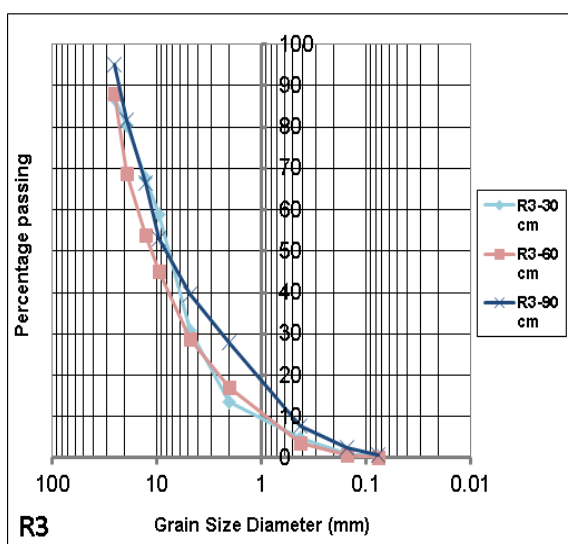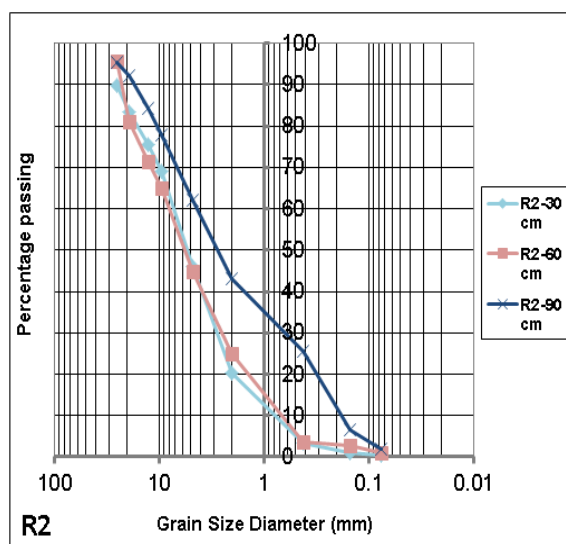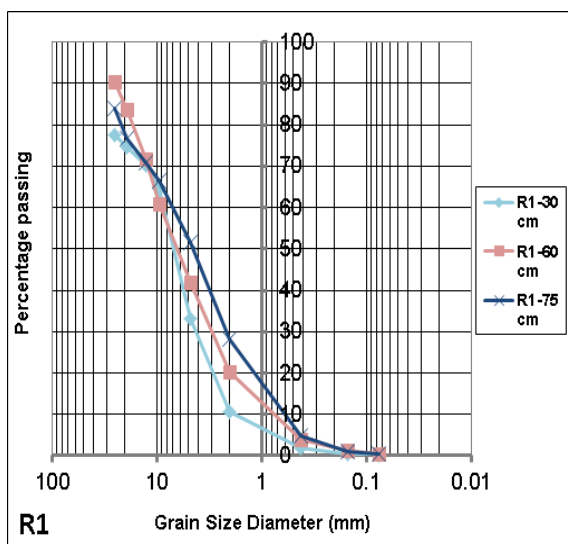
APPENDIX B

**GRAIN SIZE DISTRIBUTIONS OF THE SEDIMENTS SAMPLES
FROM THE TWO TRANSECTS**

In this appendix, the graphs of grain size distribution for the samples that were taken from the wells of right and left transects, are presented.
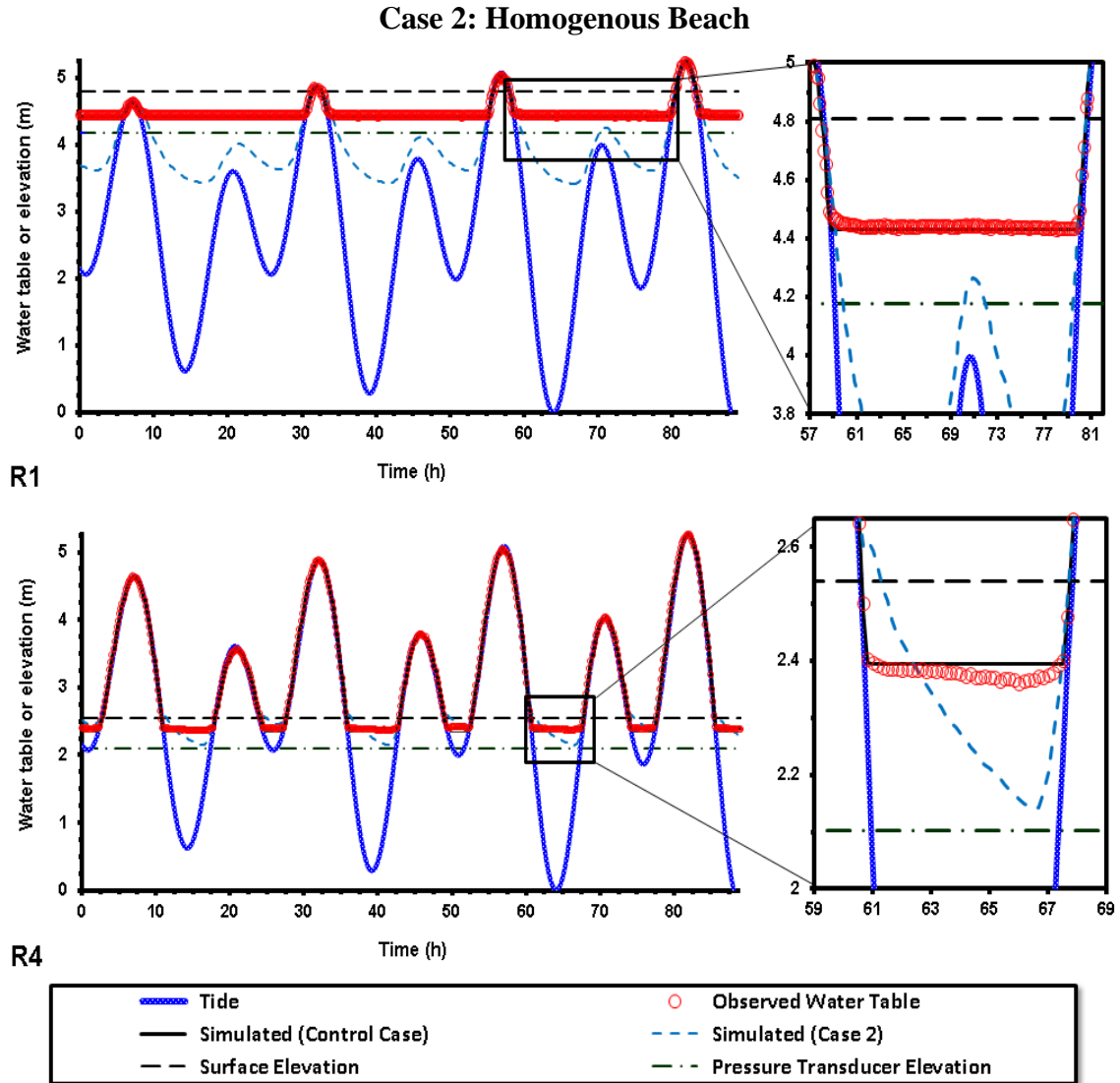
R1

R2

R3

R4

R5

R6
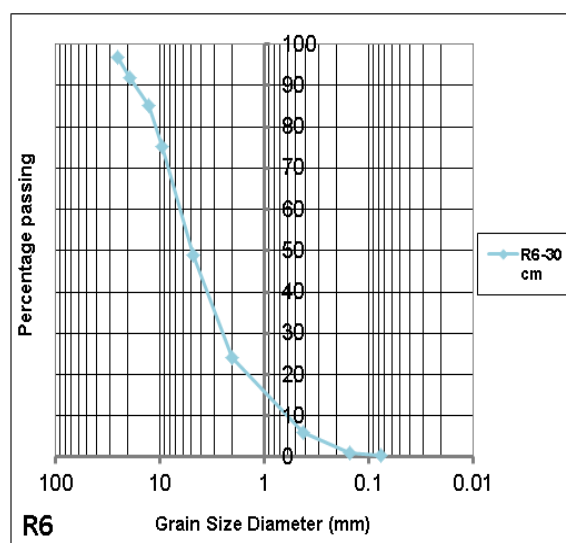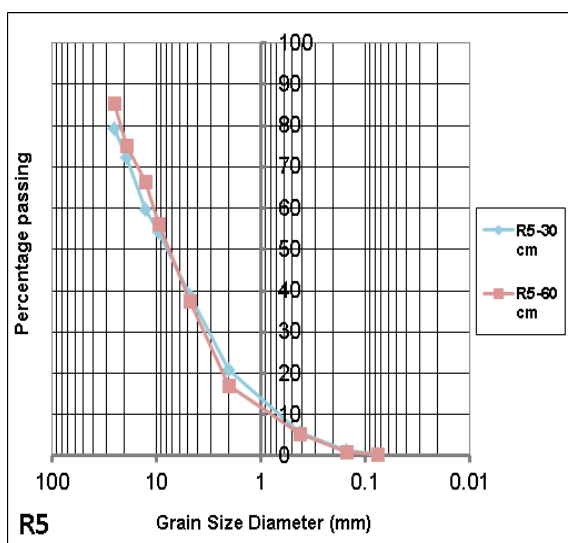
In this appendix, the simulated results of water table and pore water salinity for Case 2 to Case 8 are compared with those of the Control Case (Case 1).

Case 2: Homogenous Beach

Figure C.1 The water table at well R2 in the homogenous case (Case 2, blue dashed line) comparing to the water table in the two-layer system (Control Case, black solid line). Symbols represent the observations. The tidal level, the beach surface elevation and the elevation of the pressure transducers installed in these observation wells are shown.
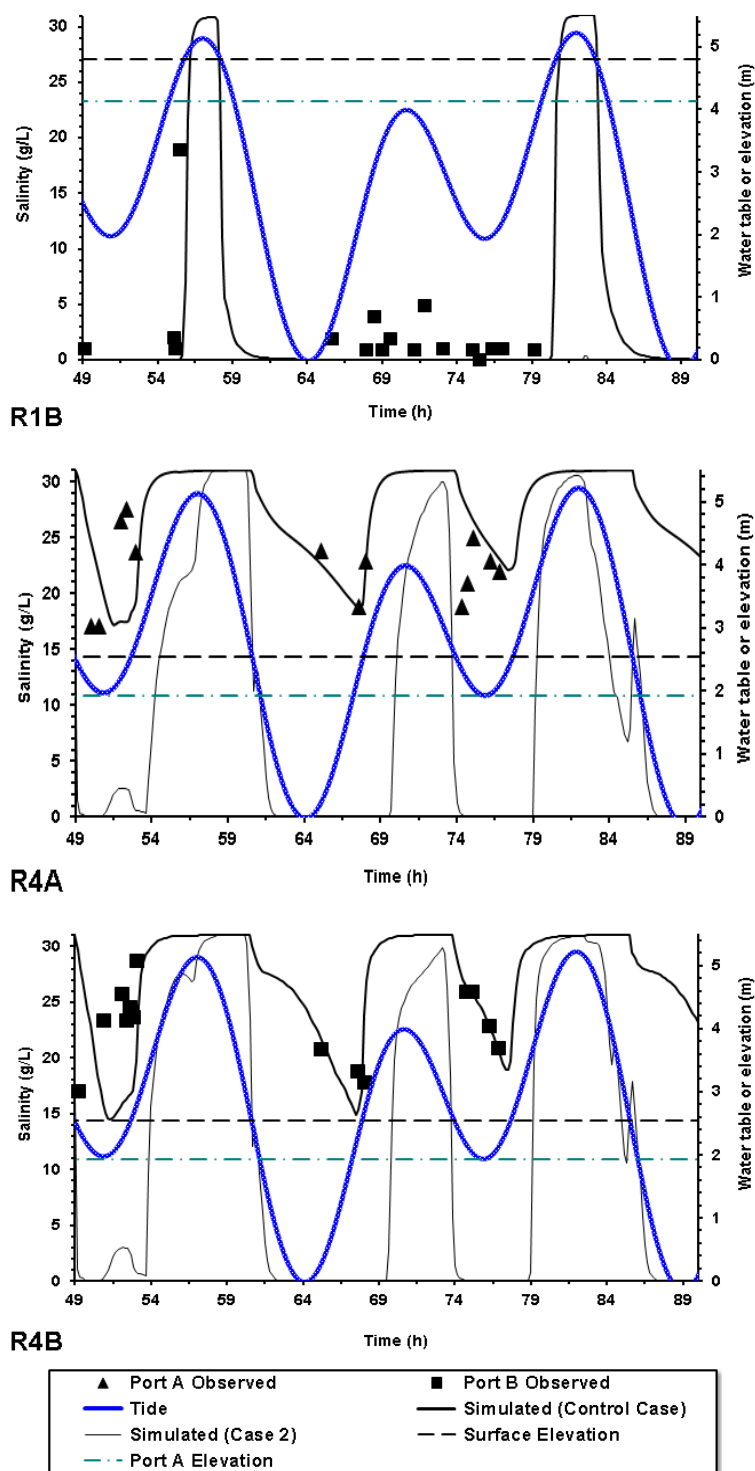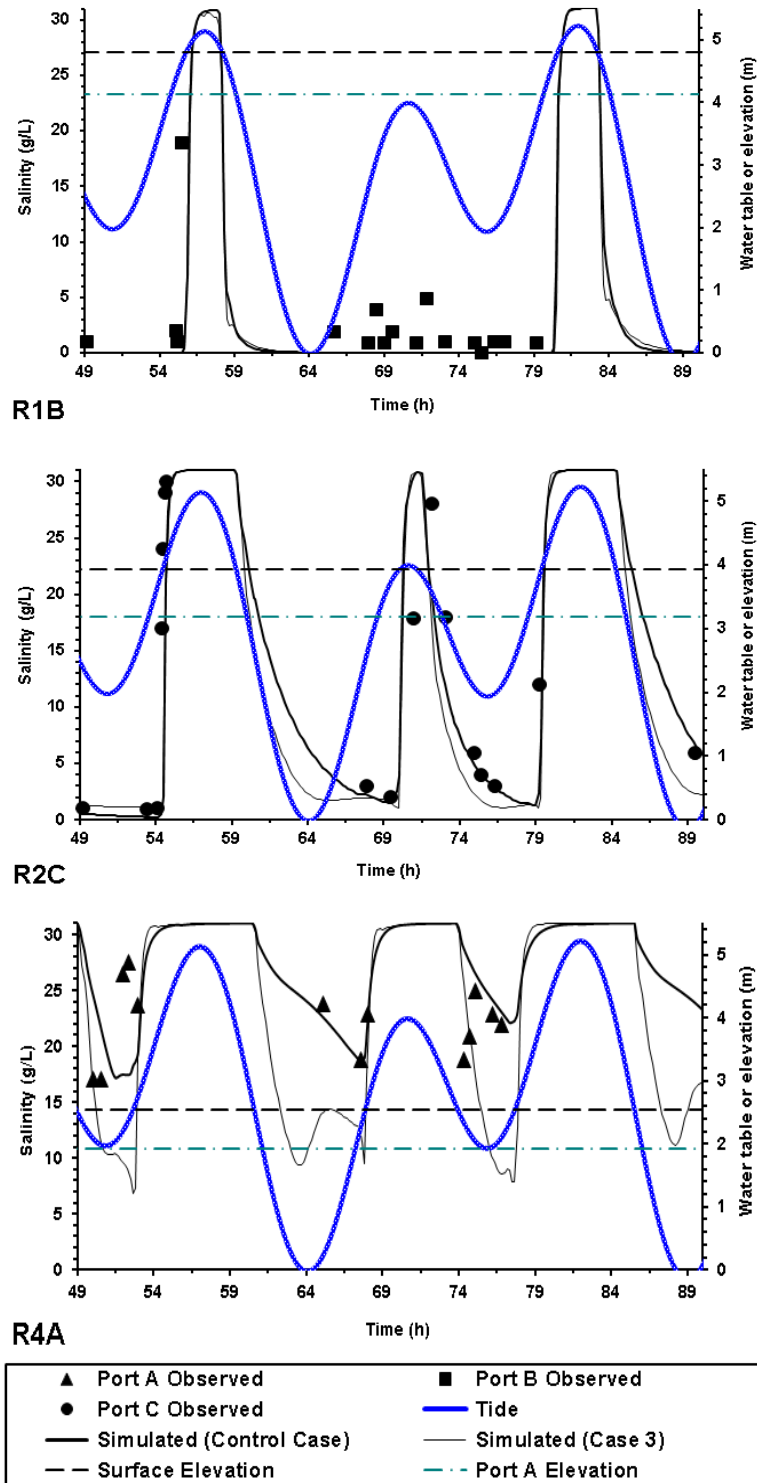
Figure C.2 The pore water salinity at R1B, R4A and R4B in the homogenous case (Case 2, thin line) comparing to the pore water salinity in the two-layer system (Control Case, thick line). Symbols represent the observations. The tidal level, the beach surface elevation and the elevation of port A in the observation well are shown.

Cases 3 and 4: Different Hydraulic Conductivity for the Lower Layer
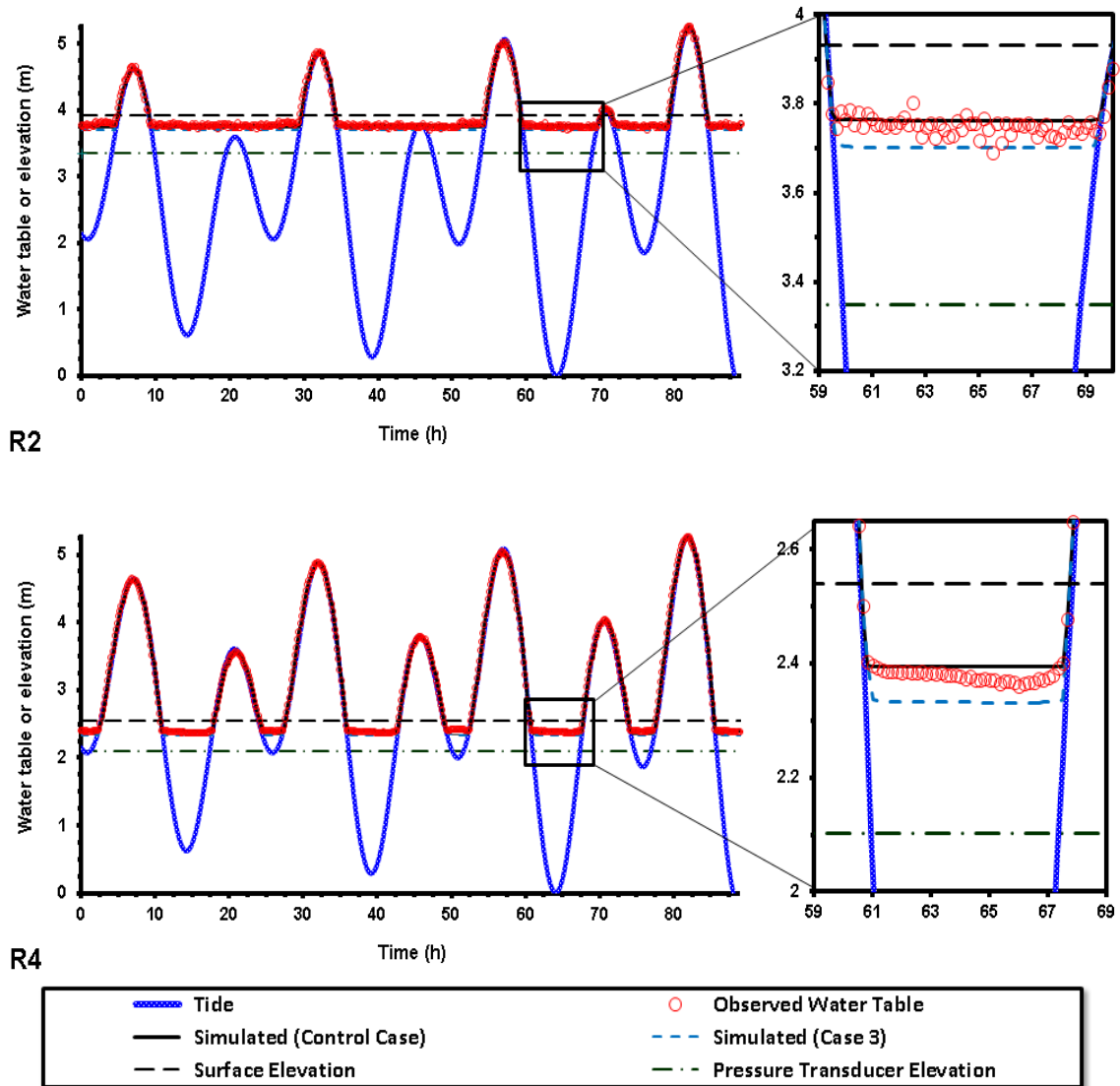
Figure C.3 The water table at wells R2 and R4 when the hydraulic conductivity of the lower layer was increased from 10^{-5} m/s (Control Case, black solid line) to 10^{-4} m/s (Case 3, blue dashed line). Symbols represent the observations.

Figure C.4 The pore water salinity at R1B, R2C, R4A and R4B when the hydraulic conductivity of the lower layer was increased from 10^{-5} m/s (Control Case, thick line) to 10^{-4} m/s (Case 3, thin line).
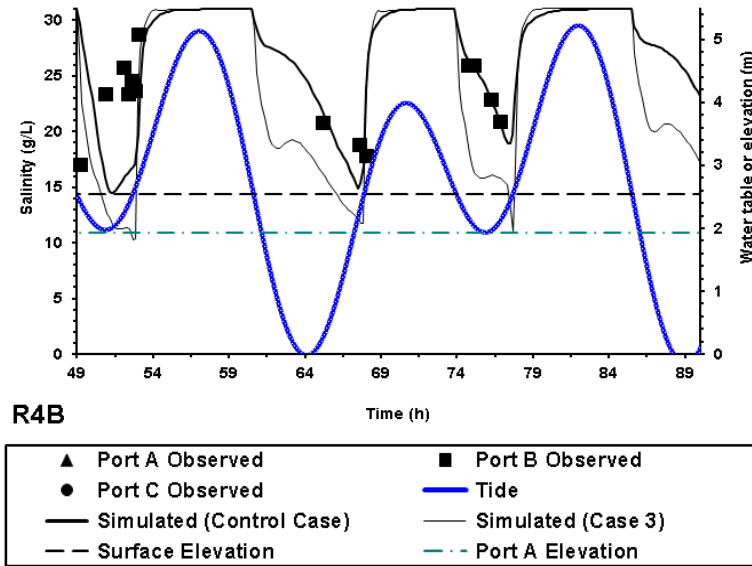
Figure C.4 The pore water salinity at R1B, R2C, R4A and R4B when the hydraulic conductivity of the lower layer was increased from 10^{-5} m/s (Control Case, thick line) to 10^{-4} m/s (Case 3, thin line). (Continued)

Figure C.5 The pore water salinity at R1B, R2C, R4A and R4B when the hydraulic conductivity of the lower layer was decreased from 10^{-5} m/s (Control Case, thick line) to 10^{-6} m/s (Case 4, thin line).
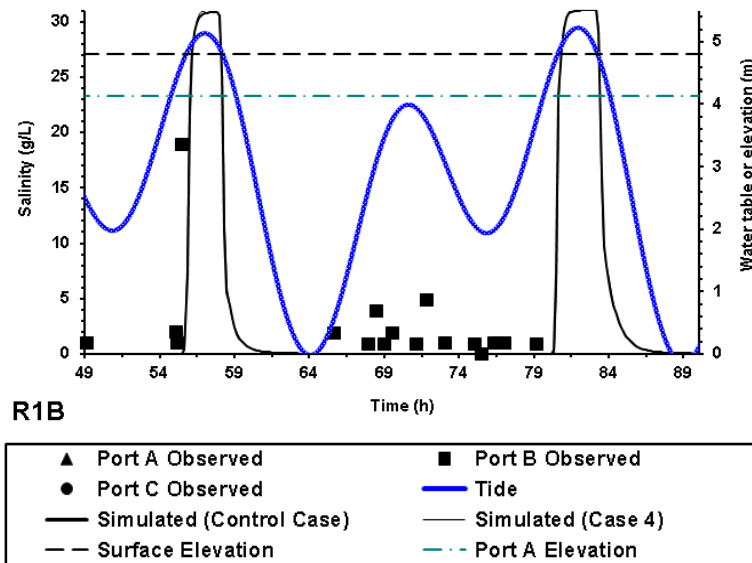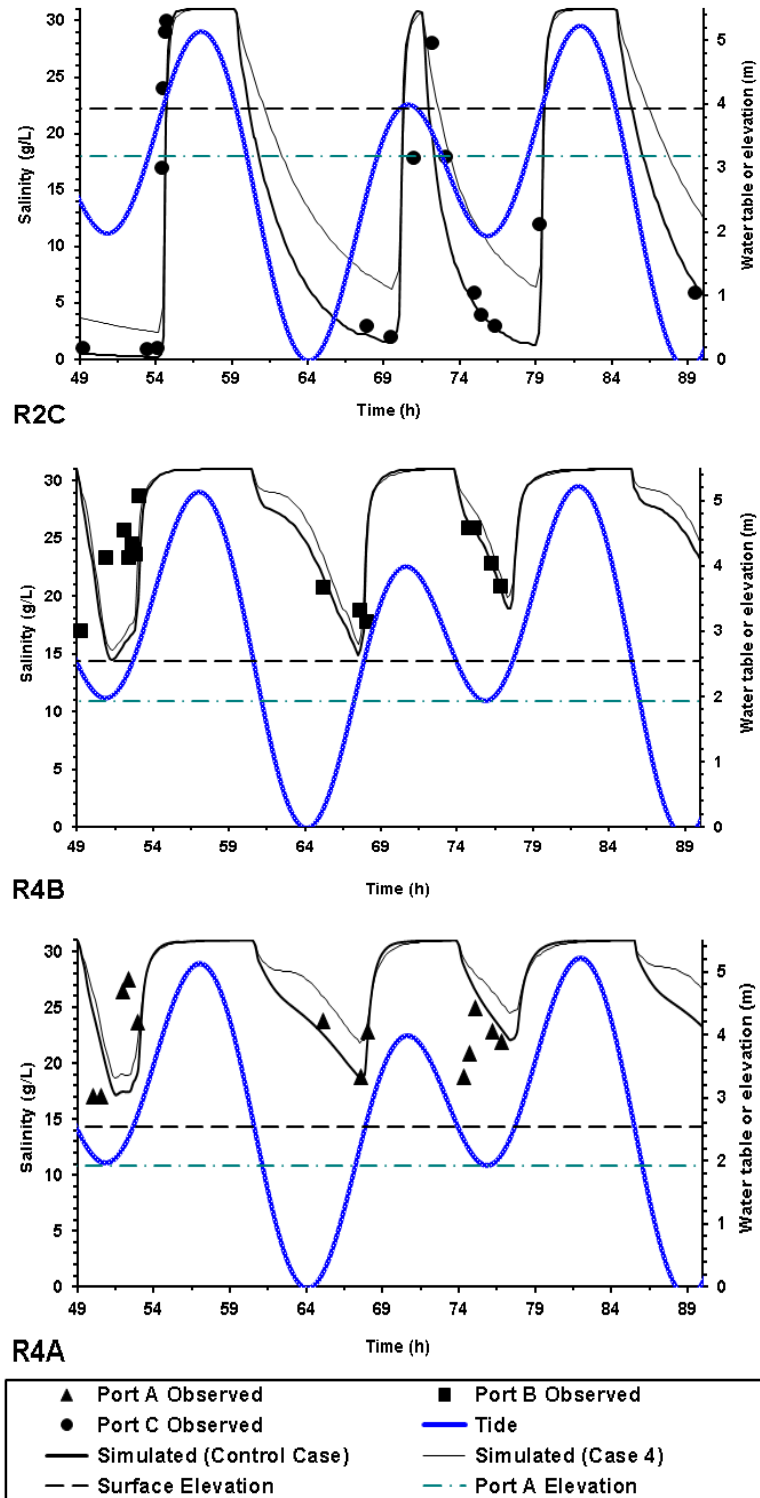
Figure C.5 The pore water salinity at R1B, R2C, R4A and R4B when the hydraulic conductivity of the lower layer was decreased from 10^{-5} m/s (Control Case, thick line) to 10^{-6} m/s (Case 4, thin line). (Continued)

Case 5: Larger Hydraulic Conductivity for Zone 1
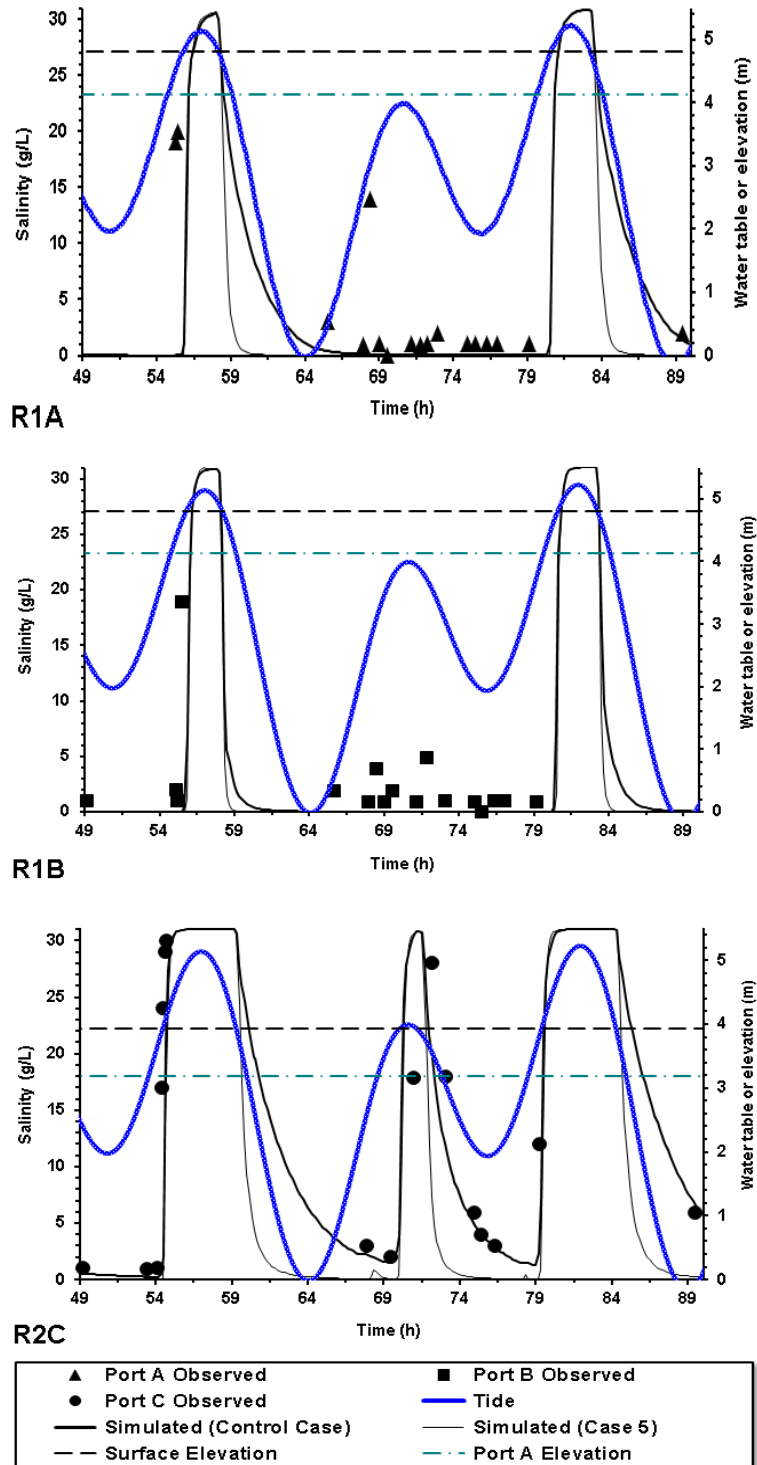
Figure C.6 The pore water salinity at R1A, R1B, R2C, R4A and R4B when the hydraulic conductivity of the upper layer in Zone 1 (20 m< x < 0 m) was increased from $7{\times}10^{-3}$ m/s (Control Case, thick line) to $5{\times}10^{-2}$ m/s (Case 5, thin line).
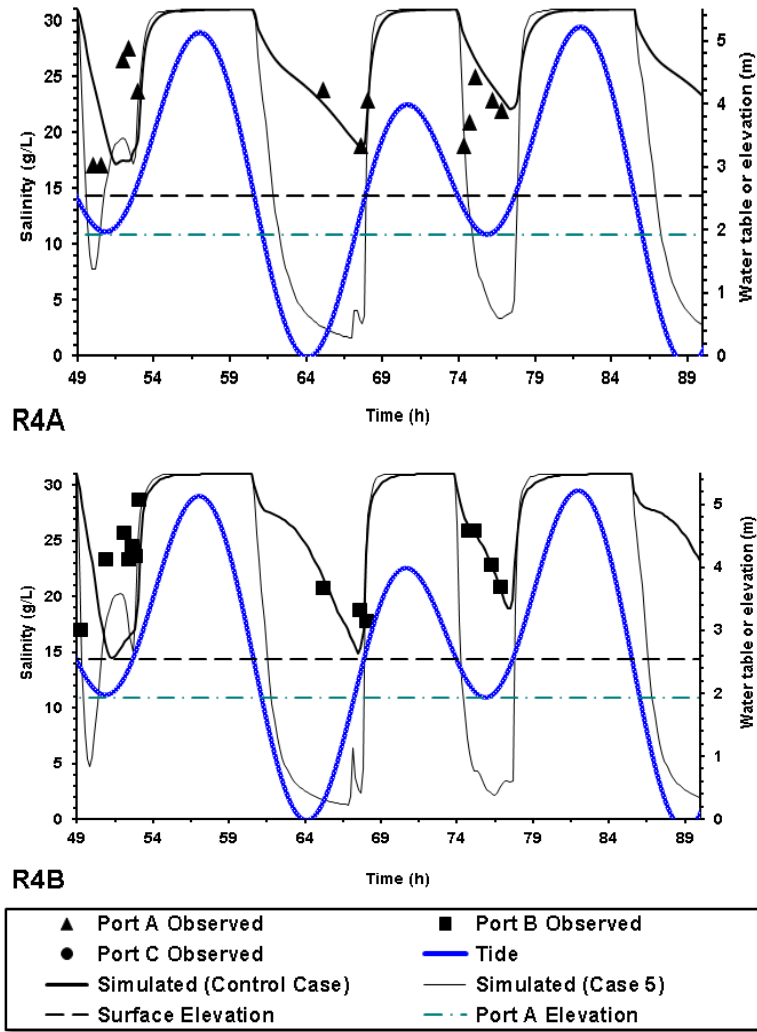
Figure C.6 The pore water salinity at R1A, R1B, R2C, R4A and R4B when the hydraulic conductivity of the upper layer in Zone 1 (20 m< x < 0 m) was increased from 7×10^{-3} m/s (Control Case, thick line) to 5×10^{-2} m/s (Case 5, thin line). (Continued)

Case 6: Smaller Hydraulic Conductivity for Upper Layer of Zone 2

Figure C.7 The pore water salinity at R1B, R2C, R4A and R4B when the hydraulic conductivity of the upper layer in Zone 2 (0 m< x < 75 m) was decreased from 5×10^{-2} m/s (Control Case, thick line) to 10^{-2} m/s (Case 6, thin line).

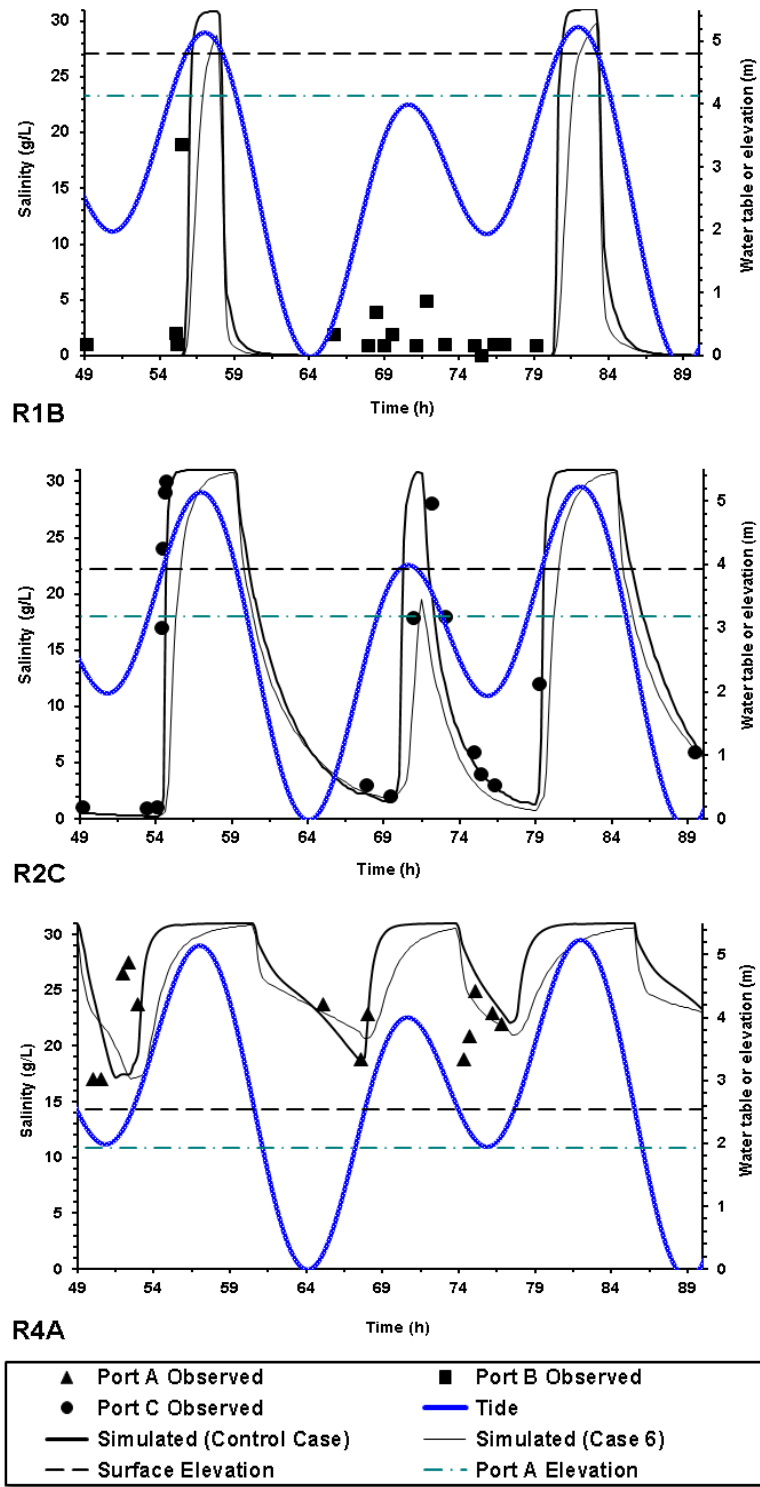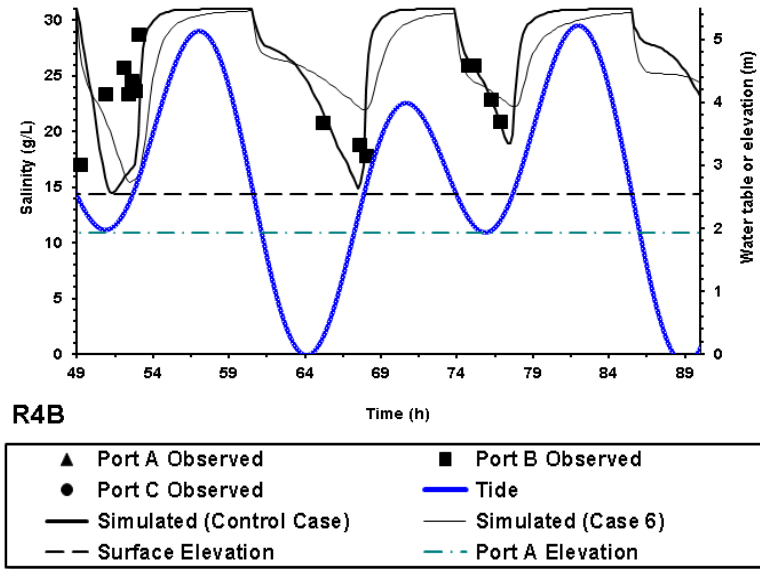**Figure C.7** The pore water salinity at R1B, R2C, R4A and R4B when the hydraulic conductivity of the upper layer in Zone 2 (0 m< x < 75 m) was decreased from 5×10^{-2} m/s (Control Case, thick line) to 10^{-2} m/s (Case 6, thin line). (Continued)

Case 7: Effect of Hydraulic Conductivity of the Pits
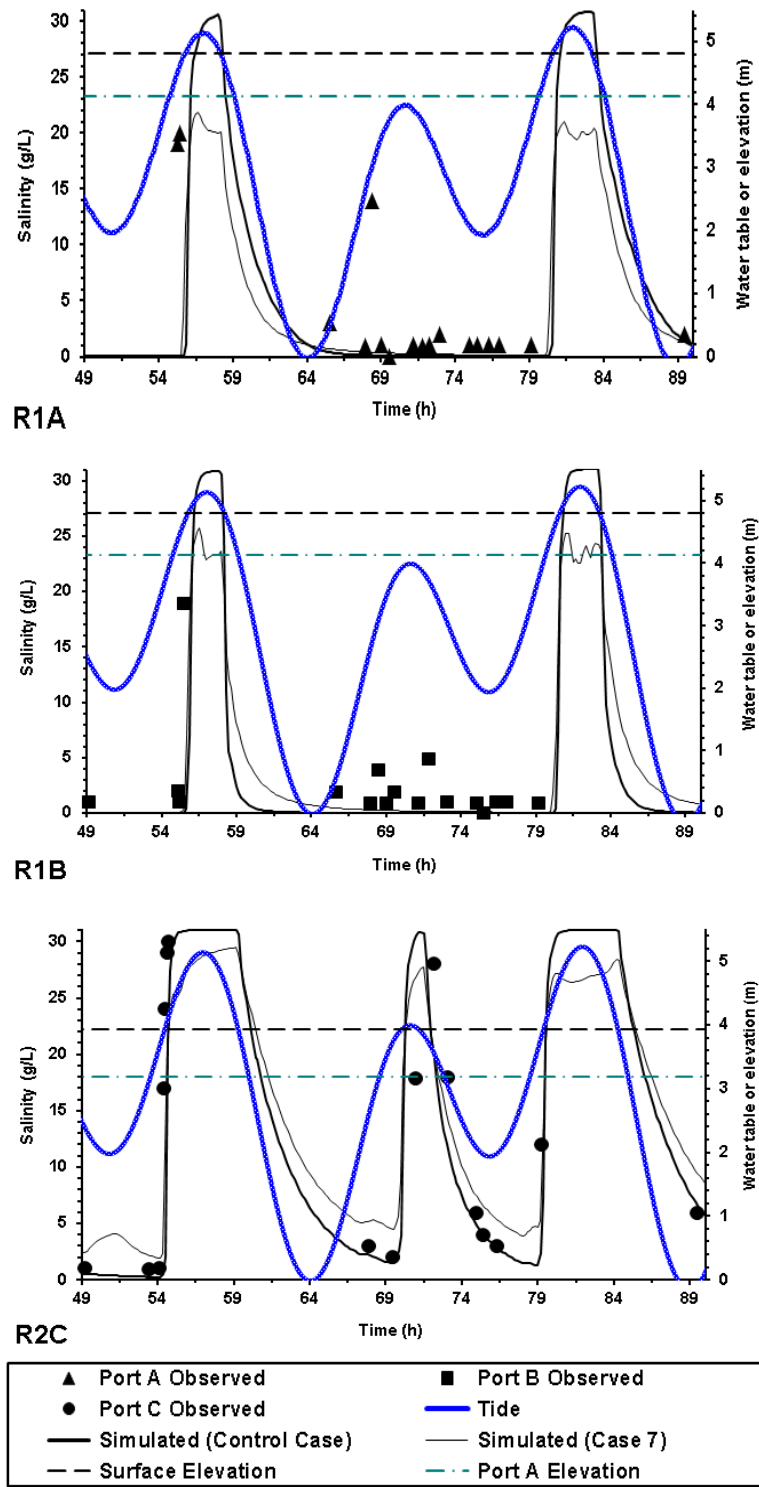
Figure C.8 The pore water salinity at R1A, R1B, R2C, R4A and R4B when the hydraulic conductivity of the sediments in the pits was decreased from 5×10^{-2} m/s (Control Case, thick line) to 5×10^{-3} m/s (Case 7, thin line).
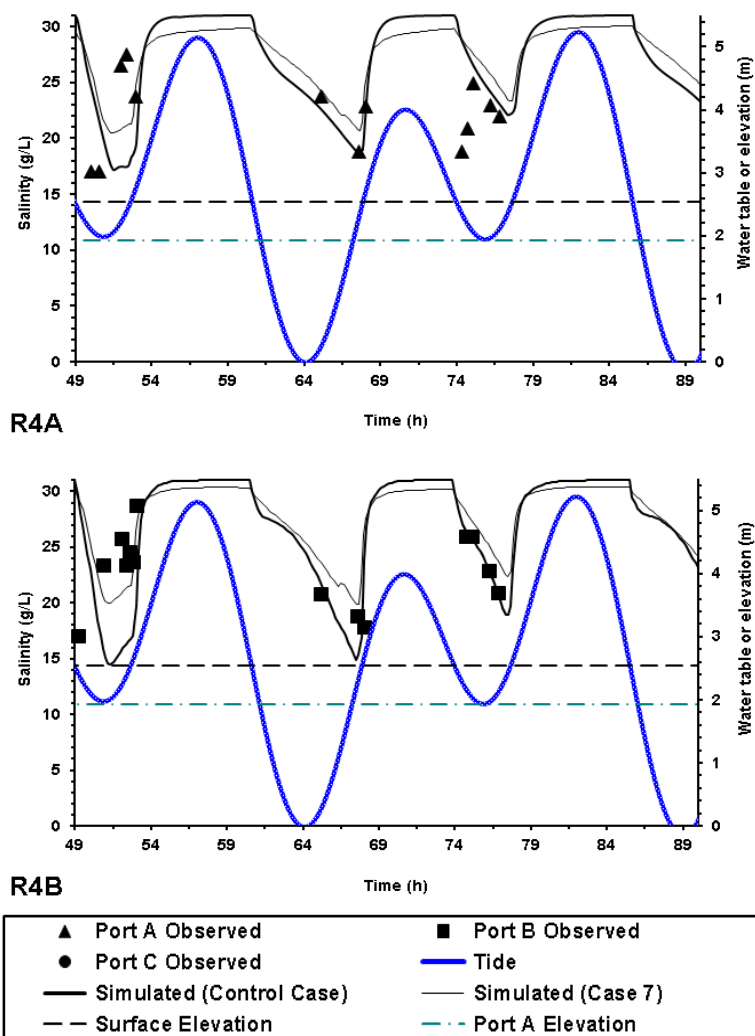
Figure C.8 The pore water salinity at R1A, R1B, R2C, R4A and R4B when the hydraulic conductivity of the sediments in the pits was decreased from 5×10^{-2} m/s (Control Case, thick line) to 5×10^{-3} m/s (Case 7, thin line). (Continued)

Case 8: Effect of Dispersion
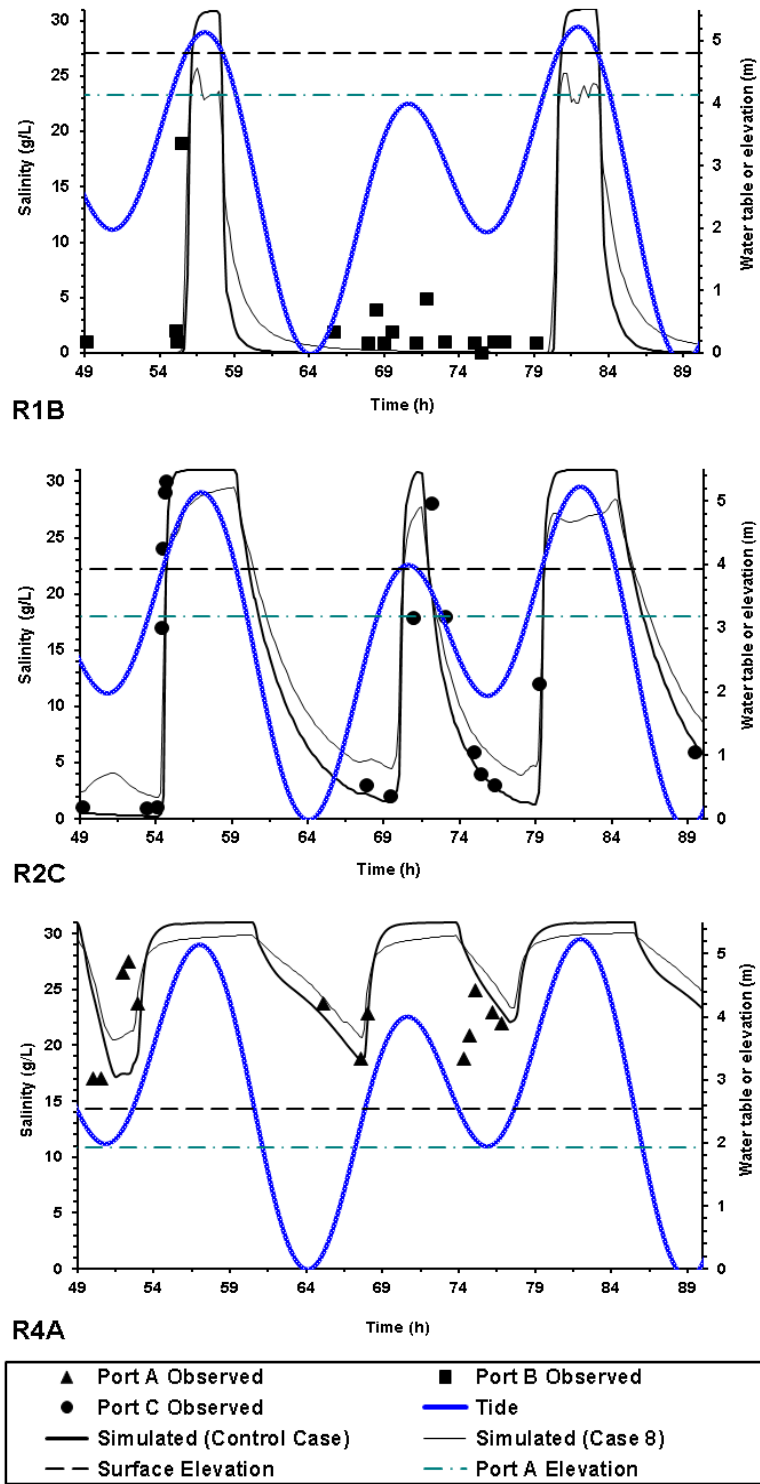
Figure C.9 The pore water salinity at R1B, R2C, R4A and R4B when the longitudinal and transverse dispersion coefficients were increased from 0.1 m and 0.01 m (Control Case, thick line) 0.5 m and 0.05 m (Case 8, thin line), respectively.
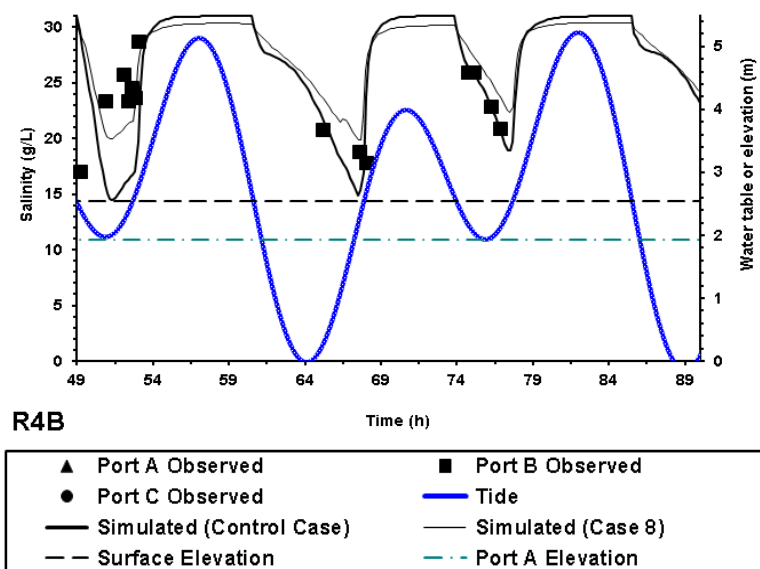
Figure C.9 The pore water salinity at R1B, R2C, R4A and R4B when the longitudinal and transverse dispersion coefficients were increased from 0.1 m and 0.01 m (Control Case, thick line) 0.5 m and 0.05 m (Case 8, thin line), respectively. (Continued)

REFERENCES

Abarca, E., Carrera, J., Sanchez-Vila, X., Dentz, M. (2007). "Anisotropic dispersive Henry problem." Adv. Water Resour., 30(4), 913-926.

Abdollahi-Nasab, A., Boufadel, M. C., Li, H., Weaver, J. W. (2010). "Saltwater flushing by freshwater in a laboratory beach." J. Hydrol., 386(1-4),1-12.

Aral, M. M., Liao, B. (1996). "Analytical solutions for two-dimensional transport equation with time-dependent dispersion coefficients." J. Hydrol. Eng., 1(1), 20-32.

Ataie-Ashtiani, B., Volker, R. E., Lockington, D. A.. (1999). "Tidal effects on sea water intrusion in unconfined aquifers." J. Hydrol., 216, 17-31.

Ataie-Ashtiani, B., Volker, R. E., Lockington, D. A. (2001). "Tidal effects on groundwater dynamics in unconfined aquifers." Hydrol. Process., 15, 655-669.

Atlas, R., Bragg, J. R. (2009). "Evaluation of PAH depletion of subsurface Exxon Valdez oil residues remaining in Prince William Sound in 2007-2008 and their likely bioremediation potential." 32nd Arctic and Marine Oil Spill Program Technical Seminar on Environmental Contamination and Response, Environment Canada, 723-747, Vancouver, BC, Canada.

Barlow, P. M., Reichard, E. G. (2010). "Saltwater intrusion in coastal regions of North America." Hydrogeol. J., 18, 247-260.

Bear, J. (1972). "Dynamics of fluids in porous media." American Elsevier, New York, NY.

Bear, J., Cheng, A. H. D., Sorek, S., Ouazar, D., Herrera, I. (1999). in "Seawater intrusion in coastal aquifers — Concepts, methods and practices". (ed. Bear, J.) (Kluwer Academic, Dordrecht, Netherlands).

Bobo, A. M., Khoury, N., Li, H., Boufadel, M. C. (2012). "Groundwater flow in a tidally influenced gravel beach in Prince William Sound, Alaska." J. Hydrol. Eng., 17(4), 478-494.

Boufadel, M. C. (2000). "A mechanistic study of nonlinear solute transport in a groundwater-surface water system under steady-state and transient hydraulic conditions." Water Resour. Res., 36(9), 2549-2566.

Boufadel, M. C., Suidan, M. T., Venosa, A. D. (1999a). "A numerical model for density-and-viscosity-dependent flows in two-dimensional variably-saturated porous media." J. Contam. Hydrol., 37, 1-20.

Boufadel, M. C., M. T. Suidan, Venosa, A. D. (1999b) "Numerical modelingof water flow below dry salt lakes: Effect of capillarity and viscosity." J. Hydrol., 221(1-2), 55-74.

Boufadel, M. C., Suidan, M. T., Venosa, A. D., Rauch, C. H., Bowers, M. T. (1999c). "Steady seepage in trenches and dams: effect of capillary flow: application to trenches and dams." Hydraul. Eng., 125, 286-294.

Boufadel, M. C., Suidan, M. T., Venosa, A. D. (2006). "Tracer studies in laboratory beach simulating tidal influences." J. Environ. Eng., 132, 616-623.

Boufadel, M. C., Xia, Y., Li, H. (2011). "Modeling solute transport and transient seepage in a laboratory beach under tidal influence." Environ. Modell. Softw., 26, 899-912.

Briggs, K. B., Richardson, M. D. (1997). "Small-scale fluctuations in acoustic and physical properties in surficial carbonate sediments and their relationship to bioturbation." Geo. Mar. Lett., 17(4), 306-306.

Brovelli, A., Mao, X., Barry, D. A. (2007). "Numerical modeling of tidal influence on density-dependent contaminant transport." Water Resour. Res., 43, W10426, doi:10.1029/2006WR005173.

Burnett, W. C., Bokuniewicz, H., Huettel, M., Moore, W. S., Taniguchi, M. (2003). "Groundwater and pore water inputs to the coastal zone." Biogeochemistry, 66(1-2), 3-33.

Buscombe, D., Masselink, G. (2006). "Concepts in gravel beach dynamics." Earth. Sci. Rev., 79, 33-52.

Carls, M. G., Thomas, R. E., Lilly, M. R., Rice, S. D. (2003). "Mechanism for transport of oil-contaminated groundwater into pink salmon redds." Mar. Ecol. Prog. Ser., 248, 245-255.

Carrier, W. D. (2003). "Goodbye, Hazen; hello, Kozeny-Carman." J. Geotech. Geoenviron. Eng., 129(11), 1054-1056.

Celia, M. A., Bouloutas, E. T., Zarba, R. L. (1990). "A general mass-conservative numerical solution for the unsaturated flow equation." Water Resour. Res., 26(7), 1483-1496.

Cobaner, M., Yurtal, R., Dogan, A., Motz., L. H. (2012). "Three dimensional simulation of seawater intrusion in coastal aquifers: A case study in the Goksu Deltaic Plain." J. Hydrol., 464-465, pp. 262-280.

Croucher, A. E., O'Sullivan., M. J. (1995). "The Henry problem for saltwater intrusion." Water Resour. Res., 31(7), 1809-1814.

Dullien, F. A. L. (1992). "Porous media: fluid transport and pore structure.", Academic Press, San Diego, CA.

Elder, J. W. (1967). "Transient convection in a porous medium." J Fluid Mech, 27(3), 609-623.

Eljamal, O., Jinno, K., Hosokawa, T. (2008). "Modeling of solute transport with bioremediation processes using sawdust as a matrix." Water Air Soil Pollut., 195(1-4), 115-127.

Freeze, R. A., Cherry, J. A. (1979). "Groundwater." Prentice Hall, Englewood Cliffs, NJ.

Fried, J. J. (1975). "Groundwater pollution." Elsevier Applied Science, New York, NY.

Frind, E. O. (1982). "Simulation of long-term transient density-dependent transport in groundwater." Adv. Water Res., 5, 73-88.

Galeati, G., Gambolati, G., Neuman, S. P. (1992). "Coupled and partially coupled Eulerian-Lagrangian model of freshwater-seawater mixing." Water Resour. Res., 28(1), 149-165.

Glover, R. E. (1959). "The pattern of fresh water flow in coastal aquifers." J. Geophys. Res., 64, 439-475.

Goswami, R. R., Clement, T. P. (2007). "Laboratory-scale investigation of saltwater intrusion dynamics" Water Resour. Res., 43(4), W04418.

Guo, Q., Li, H., Boufadel, M. C., Sharifi, Y. (2010). "Hydrodynamics in a gravel beach and its impact on the Exxon Valdez oil." J. Geophys. Res., 115, C12077.

Hayes, M. O., Michel, J., Betenbaugh, D.V. (2009). "The intermittently exposed, coarse-grained gravel beaches of prince William Sound, Alaska: Comparison with open-ocean gravel beaches." J. Coastal Res., 26, 4-30.

Henry, H. R. (1964). "Effects of dispersion on salt encroachment in coastal aquifers." U.S. Geol. Surv. Water Supply Pap., 1613-C, C71-C84.

Huyakorn, P. S., Mercer, J. W., Ward, D. S. (1987). "Saltwater intrusion in aquifers: development and testing of a three-dimensional finite element model." Water Resour. Res., 23(2), 293-312.

Kimura, M., Shimiza, R., Tsurumi, T., Ishida, K. (2001). "Measurements of acoustic and physical characteristics of surficial marine sediment." Proc., Autumn Meet. Acoust. Soc. Jpn., , Tokyo, Japan, 1221–1222.

LaBolle, E., Fogg, G., Tompson, A. (1996). "Random-walk simulation of transport in heterogeneous porous media: Local mass-conservation problem and implementation methods." Water Resour. Res., 32(3), 583-93.

Lethcoe, J. (1990). "An observer's guide to the geology of Prince William Sound, Alaska." 1st ed., Prince William Sound Books, Valdez, AK.

Li, H. L., Boufadel, M. C., Weaver., J. W. (2008). "Tide-induced seawater-groundwater circulation in shallow beach aquifers." J. Hydrol., 352(1-2), 211-224.

Li, H. L., Boufadel, M. C., Weaver., J. W. (2011). "A tracer study in an Alaskan gravel beach and its implications on the persistence of the Exxon Valdez oil." Mar. Pollut. Bull., 62, 1261-1269.

Li, H., Boufadel, M. C. (2010). "Long-term persistence of oil from the Exxon Valdez spill in two-layer beaches." Nat. Geosci., 3, 96-99.

Li, H., Boufadel, M. C., Weaver, J. W (2008). "Tide-induced seawater groundwater circulation in shallow beach aquifers." J. Hydrol., 352(1-2), 211-224.

Li, H., Zhao, Q., Boufadel, M. C., Venosa, A. D. (2007). "A universal nutrient application strategy for the bioremediation of oil-polluted beaches." Mar. Pollut. Bull., 54(8), 1146-1161.

Li, L., Barry, D. A., Jeng, D. S., Prommer, H. (2004). "Tidal dynamics of groundwater flow and contaminant transport in coastal aquifers" in Coastal Aquifer Management-Monitoring, Modeling, and Case Studies (edited by A. H.-D. Cheng and D. Ouazar), Chapter 6, 115-141, Lewis, Boca Raton, FL.

Li, L., Barry, D. A., Stagnitti, F., Parlange, J. (1999). "Submarine groundwater discharge and associated chemical input to a coastal sea." Water Resour. Res., 35, 3252-3259.

Mao, X., Enot, P., Barry, D. A., Li, L., Binley, A., Jeng, D. (2006). "Tidal influence on behavior of a coastal aquifer adjacent to low-relief estuary." J. Hydrol., 327, 110-127.

Mason, T., Coates, T. T. (2001). "Sediment transport processes on mixed beaches: a review for shoreline management." J. Coast. Res., 17, 3, 645-657.

Merritt, M. (2004). "Estimating hydraulic properties of the floridian aquifer system by analysis of earth-tide, ocean-tide, and barometric effects." U.S. Geol. Surv. Water Resour. Invest. Rep., 03-4267, 4203–4267, Collier and Hendry Counties, Tallahassee, FL.

Michael, H. A., Mulligan, A. E., Harvey, C. F. (2005). "Seasonal oscillations in water exchange between aquifers and the coastal ocean." Nature, 436, 1145-1148.

Michel, J., Hayes, M. O. (1999). "Weathering patterns of oil residues eight years after the exxon valdez oil spill." Mar. Pollut. Bull., 38(10), 855-863.

Michel, J., Nixon, Z., Hayes, M. O., Short, J., Irvine, G., Betenbaugh, D., Boring, C. (2009). "Modeling the distribution of lingering subsurface oil from the exxon valdez oil spill." Exxon Valdez Oil Spill Restoration Project Final Report (Restoration Project 070801), National Oceanic and Atmospheric Administration, Juneau, AK.

Moore, W. S. (1996). "Large groundwater inputs to coastal waters revealed by 226ra enrichments." Nature, 380, 612-614.

Moore, W. S. (1999). "The subterranean estuary: A reaction zone of ground water and sea water." Mar. Chem., 65, 111-125.

Naba, B., Boufadel, M. C., Weaver, J. (2002). "The role of capillary forces in steady-state and transient seepage flows." Ground Water, 40(4), 407-415.

Neff, J. M., Owens, E. H., Stoker, S. W., McCormick, D. M. (1995). "Shoreline oiling conditions in prince william sound following the exxon valdez oil spill." Proc., Proceedings of the 3rd Symposium on Environmental Toxicology and Risk Assessment, April 26-28, 1993, American Society for Testing and Materials, 312-346.

Nielsen, P. (1990). "Tidal dynamics of the water table in beaches." Water Resour. Res., 26, 2127-2134.

Owens, E. H., Taylor, E., Humphrey, B. (2008). "The persistence and character of stranded oil on coarse-sediment beaches." Mar. Pollut. Bull., 56, 14-26.

Page, D. S., Boehm, P. D., Neff, J. M. (2008). "Shoreline type and subsurface oil persistence in the exxon valdez spill zone of prince william sound, alaska." Proc., 31st Arctic and Marine Oil Spill Program Technical Seminar on Environmental Contamination and Response, June 3-5, 545-563.

Park, C. H., Aral, M. M. (2008). "Saltwater intrusion hydrodynamics in a tidal aquifer." J. Hydrol. Eng., 13(9), 863-872.

Park, C. H., Beyer, C., Bauer, S., Kolditz, (2008) "Using global node-based velocity in random walk particle tracking in variably saturated porous media: application to contaminant leaching from road constructions." Environ. Geol., 55(8), 1755-1766.

Philip, J. R. (1973). "Periodic nonlinear diffusion: An integral relation and its physical consequences." Aust. J. Phys., 26, 513-519.

Plafker, G. (1969). "The Alaska earthquake, regional effects, tectonics." U.S. Geol. Survey Prof. Paper, 531-I.

Sharifi, Y., Van Aken, B., Boufadel, M. C. (2011) "The effect of pore water chemistry on the biodegradation of the Exxon Valdez oil spill." Water Qual. Expo. Health, 2, 157-168.

Short, J. W., Lindeberg, M. R., Harris, P. M., Maselko, J. M., Pella, J. J., Rice, S. D. (2004). "Estimate of oil persisting on the beaches of Prince William Sound 12 years after the exxon valdez oil spill." Environ. Sci. Technol., 38, 19-25.

Short, J. W., Maselko, J. M., Lindeberg, M. R., Harris, P. M., Rice, S. D. (2006). "Vertical distribution and probability of encountering intertidal exxon valdez oil on shorelines of three embayments within prince william sound, alaska." Environ. Sci. Technol., 40(12), 3723-3729.

Simpson, M. J., Clement, T. P. (2003). "Theoretical analysis of the worthiness of the henry and elder problems as benchmarks of density-dependent groundwater flow models." Adv. Water Res., 26, 17-31.

Simpson, M. J., and Clement, T. P. (2004). "Improving the worthiness of the Henry problem as a benchmark for density-dependent groundwater flow models." Water Resour. Res., 40(1), W01504.

Slomp, C., Van Capellen, P. (2004). "Nutrient inputs to the coastal ocean through submarine groundwater discharge: controls and potential impact." J. Hydrol., 295, 64-86.

Sposito G., Barry D A. (1987). "On the Dagan model of solute transport in groundwater: foundational aspects." Water Resour. Res., 23(10), 1867-1875.

Taniguchi, M., Ishitobi, T., Shimata, J. (2006). "Dynamics of submarine groundwater discharge and fresh-seawater interface." J. Geophys. Res., 111, C01008, doi:10.1029/2005JC002924.

Taylor, E., Reimer, D. (2008). "Oil persistence on beaches in Prince William Sound – A review of scat surveys conducted from 1989 to 2002." Mar. Pollut. Bull., 56, 458-474.

Tompson, A. F. B. (1993). "Numerical-simulation of chemical migration in physically and chemically heterogeneous porous media." Water Resour. Res., 29(11), 3709-3726.

Turner, I. L., Coates, B. P., Acworth, R. I. (1997). "Tides, waves and the super-elevation of groundwater at the coast." J. Coast. Res., 13, 46-60.

Uchiyama, Y., Nadaoka, K., Rolke, P., Adachi, K., Yagi, H. (2000). "Submarine groundwater discharge into the sea and associated nutrient transport in a sandy beach." Water Resour. Res., 36(6), 1467-1479.

van Genuchten, M. T. (1980). "A closed-form equation for predicting the hydraulic conductivity of unsaturated soils." Soil Sci. Soc. Am. J., 44, 892-898.

Venosa, A. D., Suidan, M. T., Wrenn, B. A., Strohmeier, K. L., Haines, J., Eberhart, B. L., King, D., Holder, E. (1996). "Bioremediation of an experimental oil spill on the shoreline of Delaware Bay." Environ. Sci. Technol., 30, 1764-1775.

Werner, A. D., Lockington, D.A. (2006). "Tidal impacts on riparian salinities near estuaries." J. Hydrol., 328, 511-522.

Wrenn, B. A., Boufadel, M. C., Suidan, M. T. S., Venosa, A. D. (1997). "Nutrient transport during bioremediation of crude oil contaminated beaches." in 4th Int. Symp. on In-situ and On-site Bioremediation, 267-272, Battelle, Columbus, OH.

Xia, Y., Li, H., Boufadel, M. C., Sharifi., Y. (2010). "Hydrodynamic factors affecting the persistence of the exxon valdez oil in a shallow bedrock beach." Water Resour. Res., 46(10), W10528.

Zheng, C., Bennett, G. D., (2002). "Applied contaminant transport modeling." 2nd ed., John Wiley and Sons Inc., New York, NY.